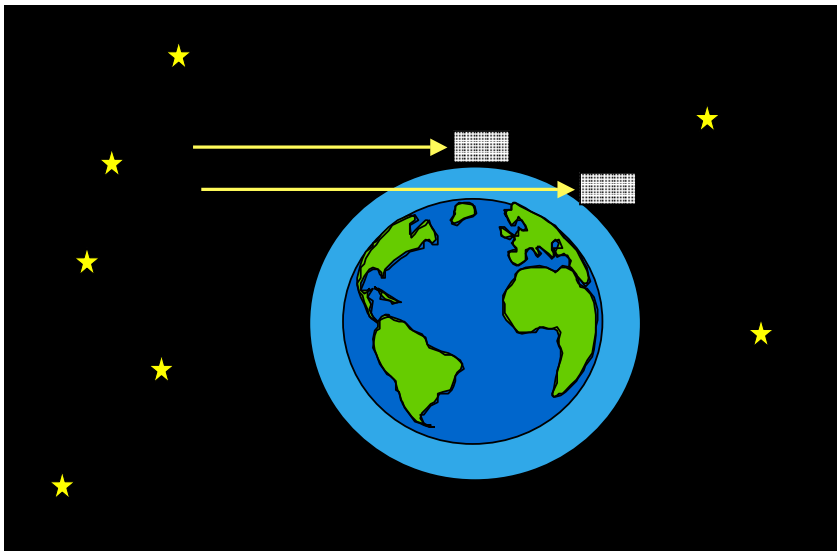

GOMOS
Algorithm Theoretical Basis Document

GOM-FMI-TN-040

Version 3.0

5.12. 2012

E. Kyrölä, FMI and L. Blanot, ACRI-ST

J. Tamminen, V. Sofieva
Finnish Meteorological Institute (FMI)

J. L. Bertaux, A. Hauchecorne, F. Dalaudier
LATMOS-IPSL

D. Fussen, F. Vanhellemont
Institut d'Aéronomie Spatiale de Belgique (IASB)

O. Fanton d'Andon, G. Barrot
ACRI-ST

Contents

Preface **5**

1 GOMOS mission **7**
1.1 Background 7
1.2 GOMOS instrument 8
1.3 Mission objectives and plan 11
1.4 GOMOS data processing 14

2 GOMOS measurement physics **17**
2.1 Introduction 17
2.2 Sources of light 18
2.2.1 Stellar sources 18
2.2.2 Sun 21
2.2.3 Planets 21
2.2.4 Auroral lights and other natural emissions 21
2.3 Propagation of stellar light through the atmosphere 23
2.4 Propagation of solar light through atmosphere 24
2.5 Detection of light by the GOMOS instrument 25
2.5.1 GOMOS instrument 25
2.5.2 Imaging properties of GOMOS 26
2.5.3 Detection properties of GOMOS 29

3 Level 0 and level 1b data processing **31**
3.1 Preprocessing of level 0 product 31
3.2 Level 1b: wavelength assignment, geolocation and datation 32
3.2.1 Wavelength assignment 32
3.2.2 Geolocation 33
3.2.3 Computation of the occultation obliquity 35
3.3 Level 1b: spectrometer data processing 36
3.3.1 Detection and correction of anomalies and outliers 37
3.3.2 Corrections to measured signal (ADU) 40
3.3.3 Separation of stellar and background signals 45
3.3.4 Full transmission calculation 49

3.3.5 Error analysis . . . 50
3.4 Photometer data processing . . . 52
3.5 Databases of level 1b processing . . . 56
3.6 Additional reference documents . . . 58
3.7 Level 1b data products . . . 58

4 Level 2 retrieval 61
4.1 Introduction . . . 61
4.2 Refraction corrections . . . 63
4.2.1 Dilution and scintillations . . . 64
4.3 Chromatic refraction correction . . . 65
4.4 Model developments . . . 66
4.4.1 Effective cross section method . . . 69
4.4.2 Spectral and temporal integration . . . 70
4.5 Spectral inversion . . . 71
4.5.1 Cross sections . . . 71
4.5.2 UVIS spectral inversion . . . 72
4.5.3 IR spectrometer spectral inversion . . . 74
4.6 Vertical inversion . . . 75
4.7 Level 2 loops . . . 78
4.8 High resolution temperature profile . . . 79
4.9 Level 2 products . . . 81

5 GOMOS data quality 85
5.1 Level 1b . . . 85
5.2 Level 2 . . . 87

6 Discussion 95

Acknowledgements 97

A Acronyms 107

B Additional sources of information 109

C Cross sections 111
C.1 O_3 . . . 111
C.2 NO_2 . . . 111
C.3 NO_3 . . . 112

D Version IPF 6 vs. IPF 5 113

Preface

The GOMOS (Global Ozone Monitoring by Occultation of Stars) instrument was launched on March, 1 2002 on board the Envisat satellite. This was 15 years after GOMOS was proposed to the European Space Agency (ESA) in 1988. The first measurements available for users are from August 2002. GOMOS measurements ended in April 2012 when the connection to Envisat was lost. During its 10 years of operation GOMOS measured about 866,000 occultations. These measurements have been used to retrieve operationally profiles of ozone, NO_2, NO_3, H_2O, and O_2. In addition aerosol extinction and high resolution temperature are retrieved.

This document, the GOMOS algorithm theoretical basis document (ATBD), describes the algorithms used in the ESA ground segment of GOMOS. The first version of ATBD appeared in 2000, two years before the Envisat launch. The second version, corresponding to the software version IPF 5, appeared in 2006. The present version corresponds to the software version IPF 6. The main changes are listed in Appendix D.

GOMOS is a novel instrument concept—in the past there have been only a few attempts to exploit stellar occultations for studies of the Earth's atmosphere. This means that most of the data processing algorithms are either completely new or they have been tailored for stellar occultations. The aim of this document is to describe the methods that are used to process raw GOMOS data to GOMOS data products. The emphasis is in the scientific justification of the selected processing algorithms and in the clear presentation of the algorithms. Chapter 1 deals with the GOMOS mission in general. The rest of the document covers two main themes. The first part, Chapter 2, presents what is known about the physics involved in the GOMOS measurements. We will concentrate on processes that are essential in the understanding of the GOMOS data algorithms. In a second part, Chapters 3 and 4 present the GOMOS data processing algorithms and how the processing chain is built. Chapter 3 focuses on the Level 1b processing where instrumental corrections are applied. Chapter 4 presents the Level 2 processing where the main geophysical products like ozone density are derived. In Chapter 5 we give examples of the achieved GOMOS performance. Appendices present acronyms, additional resources of information, absorption cross sections and the list of algorithm changes.

Chapter 1

GOMOS mission

1.1 Background

Ozone is a minor constituent in the Earth's atmosphere but plays a crucial role in shielding Earth's biosphere against solar UV-radiation. Ozone is a central element in the stratospheric chemistry and it has an important role in maintaining the thermal structure of the stratosphere. Ozone is one of the main greenhouse gases.

Ozone distribution in the atmosphere shows natural strong dependency on latitude and altitude. The total ozone peaks at about 70° in both hemispheres in spring and the lowest values are throughout the year near the equator. In the vertical direction there is a strong maximum between 15-30 km and therefore the term ozone layer is often evoked.

Observations in the mid of 1980's revealed a large springtime ozone hole over Antarctica and subsequent analysis have also shown a general slow declining trend of the total ozone content in the stratosphere (see[1]). Presently the main reasons behind these two processes are understood. The key ingredient is the release of man-made CFC-gases to the atmosphere. After a long, slow transport to the stratosphere complex CFC-molecules are dissociated by solar ultraviolet radiation and chlorine atoms are released to stratospheric air. Increased amounts of chlorine atoms amplify the normal catalytic destruction cycles of ozone. In addition to this ('normal') homogeneous chemistry, heterogeneous chemistry on polar stratospheric clouds or on surfaces of volcanic aerosol particles leads to a faster loss of ozone. This explains the extremely severe loss of ozone over Antarctica together with the low temperatures developed during the stable winter vortex over the South Pole.

The international treaties starting from the Montreal 1988 treaty have led to a decline in the amounts of CFC-gases released to the atmosphere. This has already led to the decline in the quantities of CFCs in the troposphere. Due to very long drift times to the stratosphere these trends will affect the stratospheric chlorine concentrations slowly – the recovery time of the ozone layer is predicted

to be about 50 years.

The factors that determine ozone content in the stratosphere are presently quite well known. Perhaps the most important factor that is not understood is the coupling of the greenhouse effect and the ozone problem. The enhanced greenhouse effect cools stratosphere and therefore slows down chemical reactions but also creates opportunities for build up of stratospheric clouds needed in the heterogeneous chemistry. The enhanced greenhouse effect will slow down the recovery of the ozone layer. The ozone hole took the atmospheric community by a surprise in 1985 and we cannot be sure that it was the last surprise. Adequate ozone content in the atmosphere is necessary for the normal functioning of the biosphere and therefore we need to monitor systematically the global distribution of ozone. on board Ozone distribution shows large variation as a function of latitude and so shows the ozone loss. Global observations are needed. Most of the ozone measurements in past have concerned only the total ozone columns. This is, of course, important from the point of view of the UV-problem but for analysing the changes and understanding the relation of these changes to chemical and dynamical processes we need to have measurements of the vertical distribution of ozone. The rate of ozone change is slow and the predicted recovery will last at least 50 years. Therefore, long measurement series are needed. The most important requirements for the monitoring of the ozone in the stratosphere are therefore the following ones:

- Vertical resolution
- Global coverage
- Long-term measurement series

The GOMOS instrument (Global Ozone Monitoring by Occultation of Stars) on board Envisat since 2002 is an attempt to fulfill these requirements using the star occultation method (Fig. 1.1),

1.2 GOMOS instrument

GOMOS is a spectrometer on board the European Space Agency's Envisat satellite (see Ref. [2, 3, 4, 5, 6, 7], and `https://earth.esa.int/web/guest/missions/esa-operational-eo-missions/envisat/instruments/gomos`. GOMOS uses the stellar occultation measurement principle in monitoring of ozone and other trace gases in the Earth's stratosphere. The spectral coverage is ultraviolet and visible, 250-675 nm and two infrared channels at 756-773 nm and at 926-952 nm. The two photometers work at blue 473–527 nm and red 646–698 nm wavelengths at a frequency of 1 kHz. The species retrieved by GOMOS are O_3, NO_2, NO_3, H_2O, O_2. Measurements cover altitude region 5-150 km. Atmospherically valid data are obtained in 15-100 km for ozone. Other constituents have more restricted vertical coverage.

GOMOS includes a slit to limit the background radiation (mainly solar radiation scattered from the atmosphere) entering to the detectors. The GOMOS

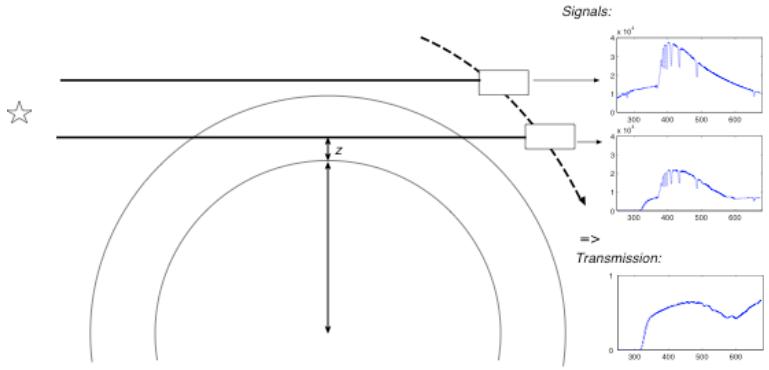

Figure 1.1: Occultation principle. The reference spectrum is measured above the atmosphere. Measurements through the atmosphere are used to calculate the horisontal transmission function that is the basis for geophysical retrieval.

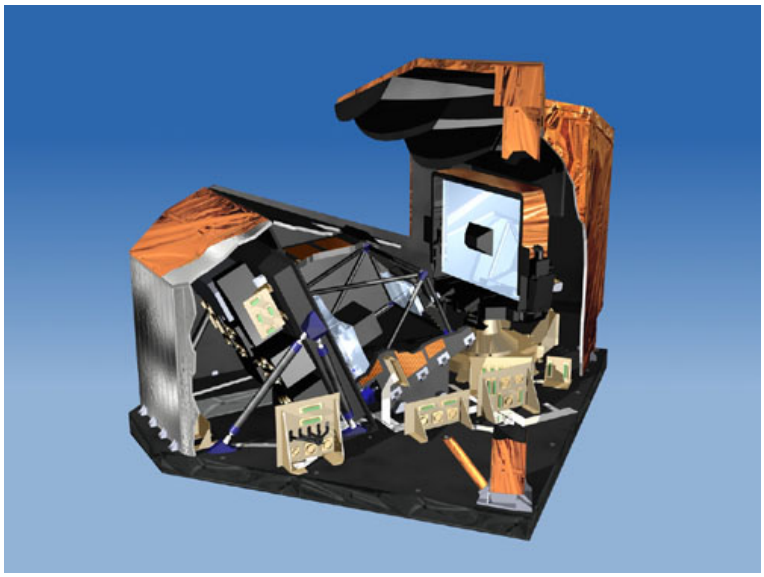

Figure 1.2: GOMOS instrument.

star tracker is sensitive inside the range 600–1000 nm. The star tracker needs to keep the star image in the centre of the slit with the accuracy of one pixel. The pointing stability is better than 40 microradians. The star tracker is able to follow a star down to 5–20 km. The altitude limit depends on the qualities of a star, the state of the atmosphere (e.g., clouds), and the limb illumination condition. GOMOS observes only setting stars. Acquisition of a setting star is much easier than a rising star (due to refraction) and getting both modes was impossible due to demanding visibility requirements in the Envisat platform

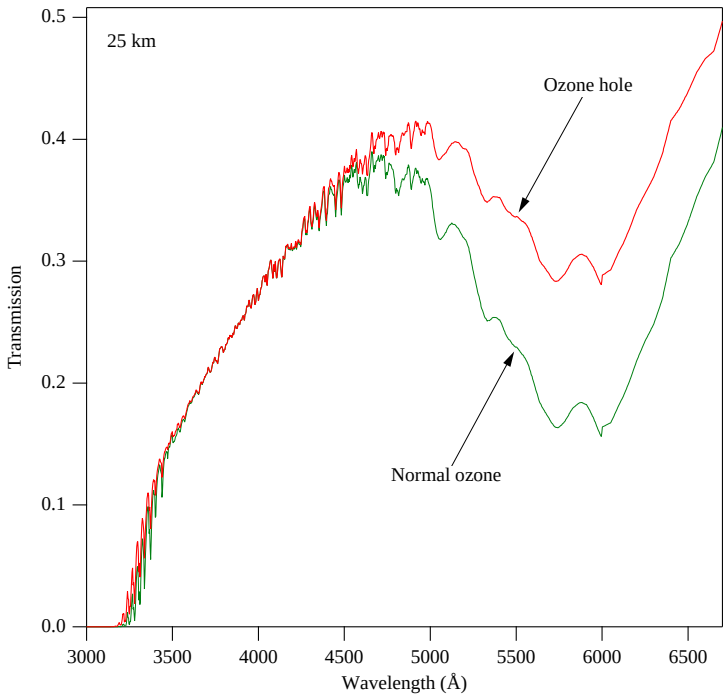

Figure 1.3: Pre-launch simulation for transmissions through the Antarctic stratosphere during normal and ozone hole conditions at 25 km tangent height.

design.

The benefit of the occultation principle is its self-calibrating measurement principle (for references and reviews for occultation method, see Ref. [8, 9, 10, 11, 12]). The reference stellar spectrum is first measured when a star can be seen above the atmosphere. During the occultation measurements through the atmosphere provide spectra with absorption features from the propagation through the atmosphere (see Fig.1.3). When these occulted spectra are divided by the reference spectrum, nearly calibration-free horizontal transmission spectra are obtained (see Fig. 1.3). It must be noted, however, that this assumes that the estimated dark charge that needs to be subtracted from the signals is small compared to signals. For stellar occultations this is not always a sound assumption. The transmissions provide the basis for retrieval of atmospheric constituent densities.

The self-calibration means that GOMOS measurements can be used to create long time series and data from any new similar instrument can be joined with the GOMOS data without calibration questions. GOMOS uses stars seen through the Earth's limb as source of light. The limb viewing geometry, the point source nature of stars and short enough measurement integration time provide good vertical resolution. The vertical sampling distance is 1.7 km for occultations

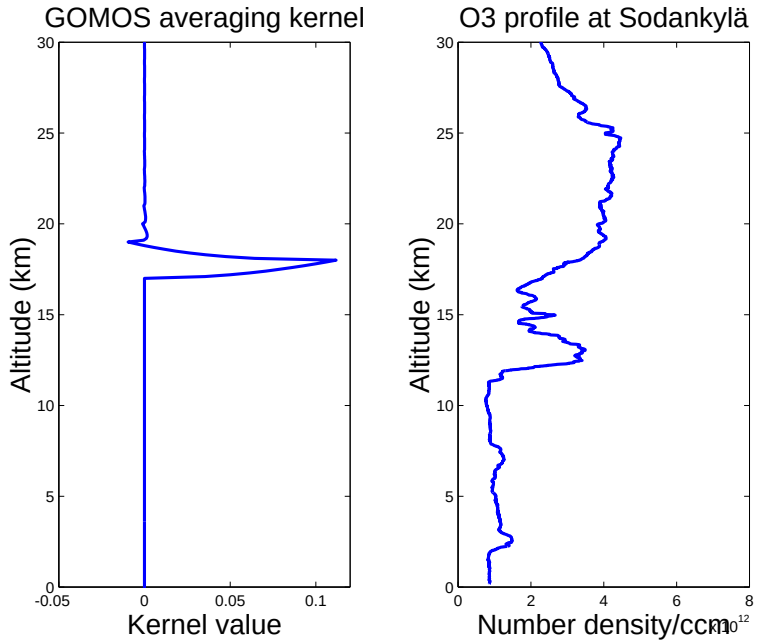

Figure 1.4: The GOMOS averaging kernel (here at 18 km tangent height) and a ozone vertical profile with fine structures.

taking place in the orbital plane. For occultations with FOV outside the orbital plane the integration distance is even smaller. The GOMOS averaging kernel (without the vertical smoothing, see Sec. 9.2) and a typical ozone profile with fine structures are displayed in Fig. 1.4.

1.3 Mission objectives and plan

Depending on the time of year, there are 150 to 300 stars that are bright enough for GOMOS to track and that are in field of view of the instrument at specific times during an orbit. Since the actual occultation time windows often overlap each other, they can not all be observed. Therefore, a number of alternative occultation sequences can be planned (see Fig. 1.5). Each sequence has different characteristics, for example, with respect to the ozone retrieval. This creates an opportunity to find an optimal sequence for a specific mission objective.

The most important properties of a star for occultation measurements in the UV-visible wavelength region are the shape of its spectrum and the brightness. Hot stars emit plenty of UV-radiation that penetrates the Earth's atmosphere in horizontal direction only at high tangent altitudes. Cold stars, on the contrary, emit mainly in visible and infrared region and the atmosphere is fairly transparent at these wavelengths down to low tangent altitudes. Different star

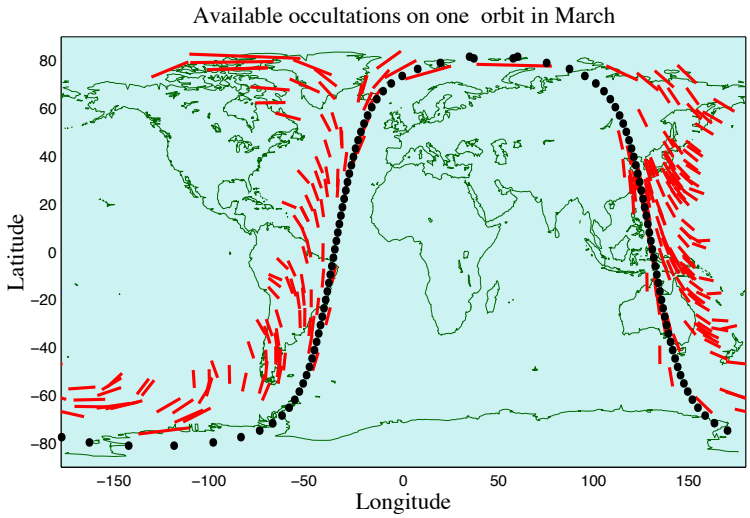

Figure 1.5: An example of the available occultations on one orbit. Each red line corresponds to one occultation. The satellite orbit is denoted with dots.

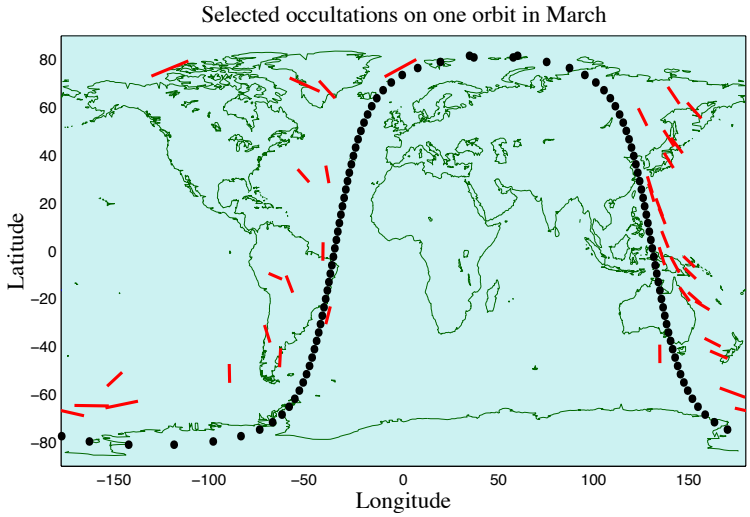

Figure 1.6: An example of the selected occultations on one orbit.

temperatures mean, therefore, that stars are probing different atmospheric altitude regions. This leads to different retrieval accuracies at different altitudes. The brightness of the star affects directly the signal to noise ratio of the instrument (see Ref. [13, 14]).

In order to accomplish the optimisation of the mission plan we quantify the

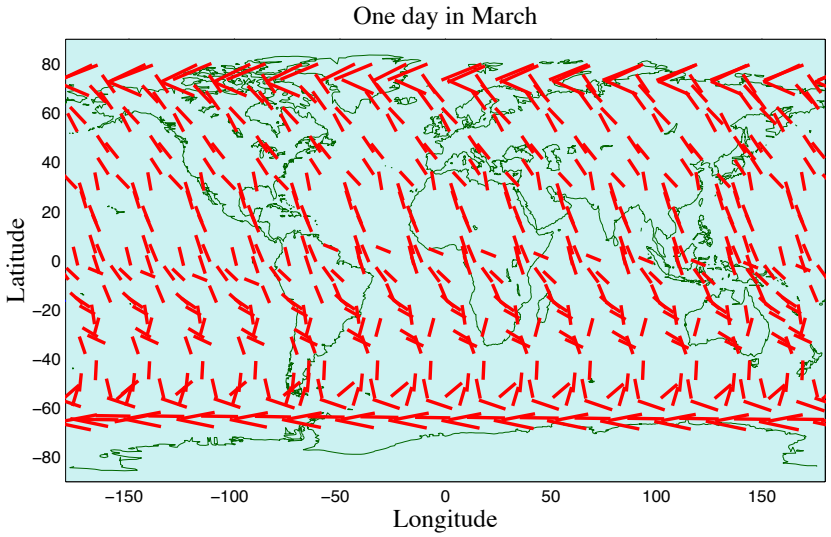

Figure 1.7: Global coverage of the occultations predicted.

GOMOS mission objectives by criteria, which allow us to compare occultations and occultation sequences with one another. Any scientific objective is characterised by a set of criteria. Each mission planning criterion is activated by introducing the data requirements of the criterion. Each data requirement is transformed to a mathematical merit function. From the set of possible occultations and the corresponding mission planning database the mission planning optimisation algorithm selects the sequence of occultations which fulfils the requirements in a best possible way. An example of the selection results is shown in Fig. 1.6. A typical global coverage in day hours is shown in Fig. 1.7. During 24 hours, the total number of occultations is 400-600 provided the nominal measurement configuration.For more information on GOMOS mission planning see Ref. [15, 16] and references therein.

During August 2002-April 2012 (end of the ENVISAT mission) GOMOS measured about 866 000 occultations. The ongoing GOMOS data consolidation will provide more data from the period April, 2002–August, 2002 and makes the data set fully consistent (see `http://earth.eo.esa.int/pcs/envisat/gomos/consolidated_dataset/Level_0/index.html`). The number of measurements per month is shown in Fig. 1.8. The daily average number of measurements in the beginning was about 400. In spring 2003 GOMOS suffered from a steering system problem and the measurement efficiency was lower until the end of July 2003 when the problem was solved by switching to a redundant electronics chain of the instrument. A second steering system problem occurred in the end of January 2005. The instrument was not used operationally until the end of August 2005. The operations resumed with a restricted azimuthal range of the steering system. This number of measurements decreased to about 280

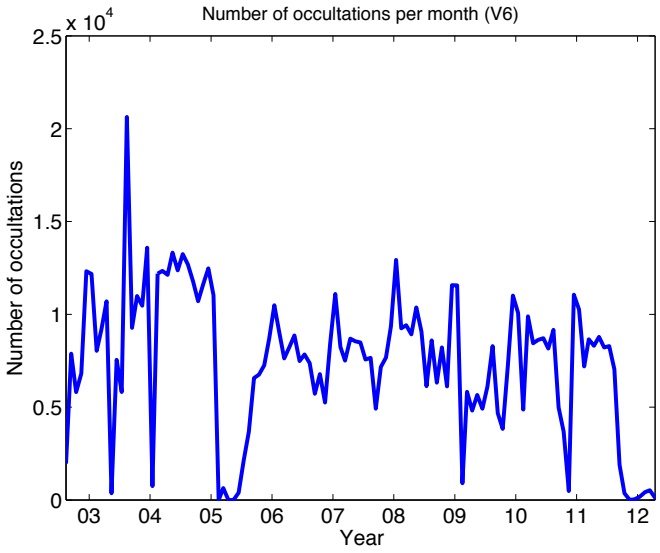

Figure 1.8: The distribution of the number of occultations starting from March 2002 to April 2012.

occultations per day (see Fig. 1.8). In Fall 2011 GOMOS measurements were severely restricted to the recurring problems in the steering system and only a few occultations per orbit were possible.

1.4 GOMOS data processing

The large number of measurements and the wealth of spectral data make it mandatory to have an effective data processing system for GOMOS. GOMOS is an ESA developed instrument and the ground segment for GOMOS is also developed by ESA Ref. [17]. The ground processing is divided to the near-real time processing and the off-line processing. The processing levels are 1b and 2. For GOMOS the division between the Level 1b and the Level 2 is the transmission function.

ESA handles the near-real time processing of Levels 1b and 2 and the off-line processing of Level 1b. The off-line processing centre for Level 2 is located at Finnish Meteorological Institute's Sodankylä observatory (the FIN-CoPAC facility). Off-line data are disseminated through DLR's D-PAC in Oberpfaffenhofen. The overall ground processing scheme for Envisat is presented in Ref. [17].

The GOMOS data processing algorithms have been developed in the contract between ESA and the ACRI company in Sophia-Antipolis, France. The

scientific institutes, Finnish Meteorological Institute, Service d'Aéronomie du CNRS (presently LATMOS-IPSL) and Institut d'Aéronomie Spatiale de Belgique, form the GOMOS Expert Support Laboratory-coalition (ESL).

GOMOS data retrieval algorithms have been discussed in several scientific publications [18, 13, 19, 6]). The algorithms discussed here constitute the Envisat GOMOS ground segment supported by ESA. GOMOS mission objectives and mission planning aspects are discussed in Ref. [15, 16, 6, 20]. GOMOS error characterisation have been discussed in [20]. GOMOS data products are discussed in Ref. [21].

Chapter 2

GOMOS measurement physics

2.1 Introduction

GOMOS relies on the occultation measurement principle in monitoring of ozone and other trace gases in the stratosphere. The point source character of stars, and the weakness of their radiation, make it necessary to consider some questions that are not relevant to the solar occultation method, the method favoured in past. The low S/N-ratio means that we must put additional effort in data retrieval and we must understand what additional light sources may compete with the main stellar signal. Because one half of each orbit is illuminated by the sun, GOMOS detects scattered solar light which easily dominates the stellar signal. GOMOS also sees light coming from auroral and other natural emissions in the atmosphere. The CCD detector used by GOMOS makes it, however, possible to estimate radiation coming from extended sources and extract it from the main signal. The measurement principle is shown in Fig. 2.1.

An occultation measurement can be thought as a measurement of the atmo-

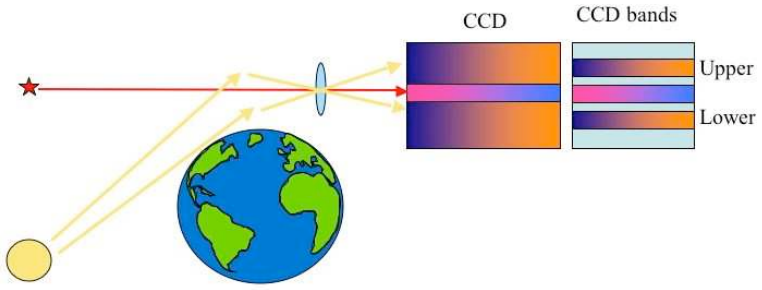

Figure 2.1: Use of GOMOS CCD to measure atmospheric background radiation.

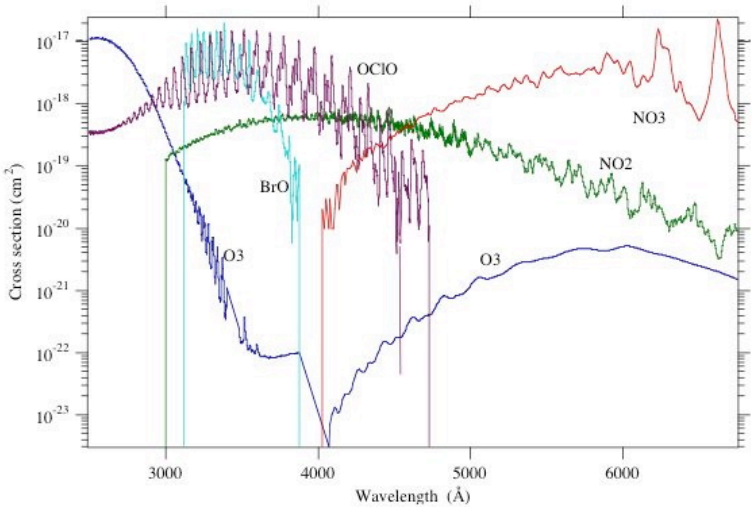

Figure 2.2: Cross sections.

spheric transmission between the source and the instrument. The transmission cannot be directly observed but it can be calculated from measurements through and above the atmosphere. The transmission can be modelled by using the well-known Beer-Lambert law:

$$T_{\text{ext}} = e^{-\tau} \tag{2.1}$$

where the optical depth τ is given by

$$\tau(\lambda) = \sum_j \int \sigma_j(\lambda, \bar{r}(s))\rho_j(\bar{r}(s))ds \tag{2.2}$$

Here ρ_j's are the constituent densities depending on the position $\bar{r}$ and σ_j's are the absorption or scattering cross-sections (see Fig. 2.2). The integration is made along the line of sight joining the instrument and the source. The scales of the measurement are shown in Fig. 2.3. The modelled transmission gives the desired coupling between measurements and the geophysically interesting constituent profiles.

2.2 Sources of light

2.2.1 Stellar sources

The main light sources for GOMOS are stars that provide a sufficient flux in the spectral range 250-952 nm where the GOMOS detectors and the star tracking system work. The instrumental performance restricts the visual magnitudes to 4 or brighter and the acceptable temperature range is 3000-30000 K. Obviously GOMOS measurements are difficult to interpret if a star is rapidly varying.

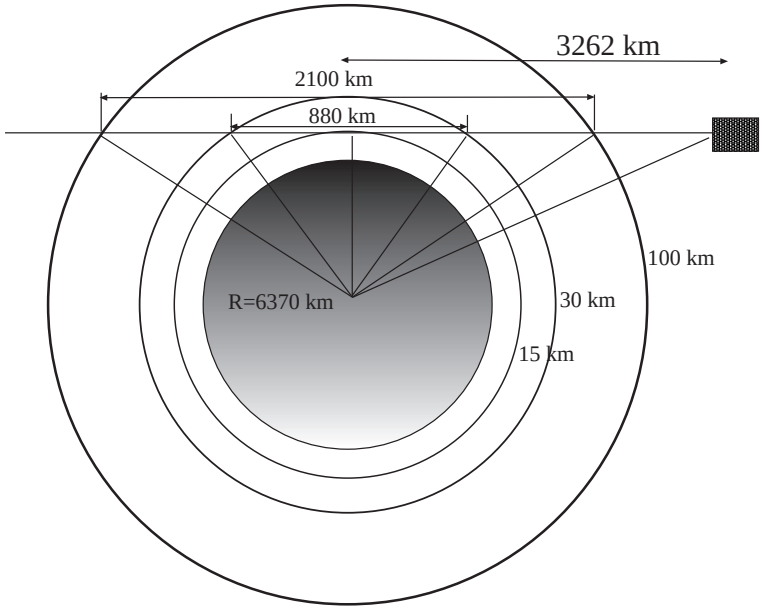

Figure 2.3: GOMOS geometry scales.

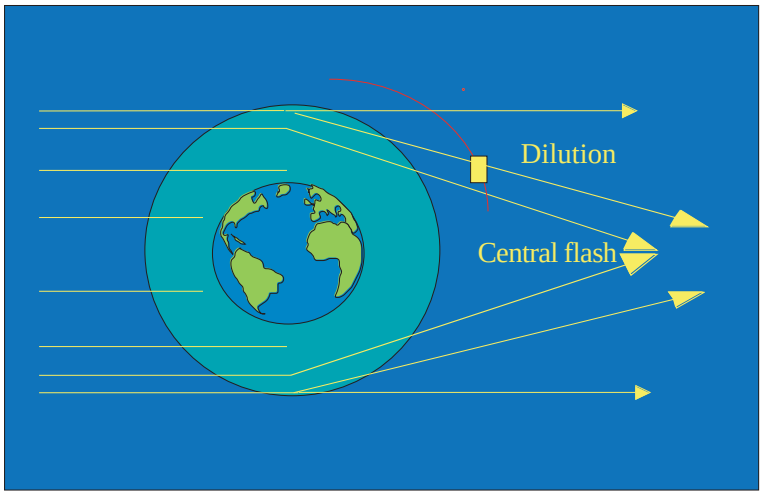

Figure 2.4: Refractive dilution and the central flash.

Difficulties are also encountered if two or more stars are visually close to each other.

The GOMOS measurement principle does not necessarily require that we know the actual spectrum of a star that we measure. For many purposes related to calibration this would, however, be advantageous and for the signal

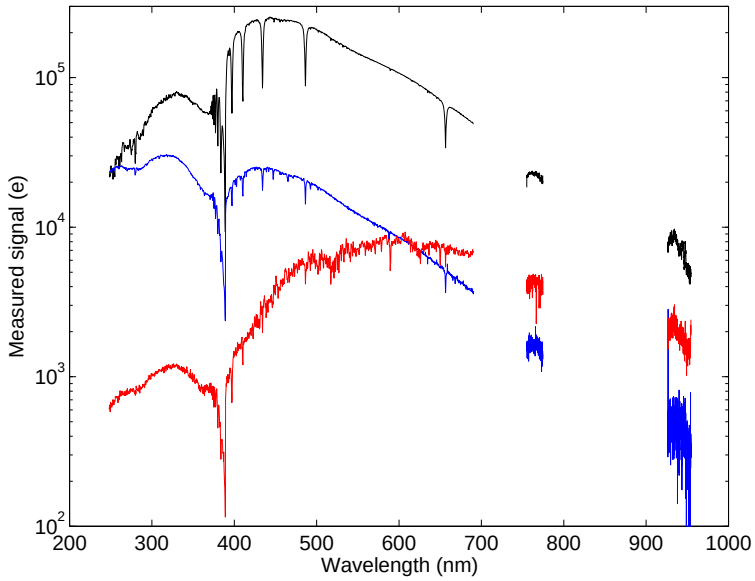

Figure 2.5: Star spectra measured by GOMOS. The spectrum of the visually brightest star in the sky, Sirius or α CMa, is shown by the black line. Sirius' visual magnitude is -1.44 and the effective surface temperature (determined from the spectral class) 11 000 K. The blue line shows the spectrum for the star β Cru with magnitude 1.253 and temperature 30 000 K. The red line represents the spectrum of the star ϵ Car with magnitude 1.86 and temperature 4100 K. The visual magnitudes determine the flux at 550 nm by $F = F_{\mathrm{ref}} 10^{-m/2.5}$. Figure is from ref. [19].

simulation it is necessary. Because the signal simulation is needed for the algorithm development and the testing, a discussion is warranted.

There are no measurements of stellar spectra covering the whole spectral range of GOMOS. This is because the GOMOS spectral window is larger than the atmospheric window (from ground). In the visible range the atmosphere is almost transparent and good spectral measurements can be carried out from ground based observatories. Below 300 nm the ozone layer prevents any stellar light from reaching the ground and the only way to record UV spectra is to use satellite borne spectrometers. So far satellite measurements have been limited to UV parts of stellar spectra. Therefore complete (from the GOMOS point of view) spectra can only be reached by combining ground based and space based measurements. This is obviously a difficult task. Service dAeronomie has constructed a few stellar spectra by combining satellite and ground based measurement. Stellar spectra are often approximated by a blackbody model and in the GOMOS algorithm development this approach has been widely used. A blackbody model gives a rough simulation of the intensity distribution of a target star but it misses all narrow structures like Fraunhofer lines and ionisation

edges, Fig. 2.5 shows GOMOS measurements of stellar spectra from a hot and cool star and from the brightest star in the sky, Sirius.

2.2.2 Sun

GOMOS does not look directly toward the Sun because of the large difference between solar and stellar brightness. However, in bright limb measurements GOMOS measures the solar light scattered once or several times in the atmosphere. The solar spectrum for the spectral range needed for GOMOS is quite well known, It is known to be stable with a precision better than 1%. Higher variability occurs for shorter wavelengths.

2.2.3 Planets

GOMOS can also measure occultation of planets. Contrary to stars, planets are bright targets and they have extended angular size. Since GOMOS has very large slit (at the entrance of the spectrometers), the finite angular size of the planets translates directly into an increased spectral spread. However, except for spectrometer B (narrow O_2 and H_2O lines), the impact on transmission spectrum is rather limited. Such behavior was not observed for the case of Mars occultation. Earth came unusually close to Mars on August 27, 2003. By a fraction of a percent, Earth was closer than any time in the last 60,000 years or so. A dedicated three week campaign was set up, encompassing this date, and providing very low phase angle observations of Mars at its brightest.

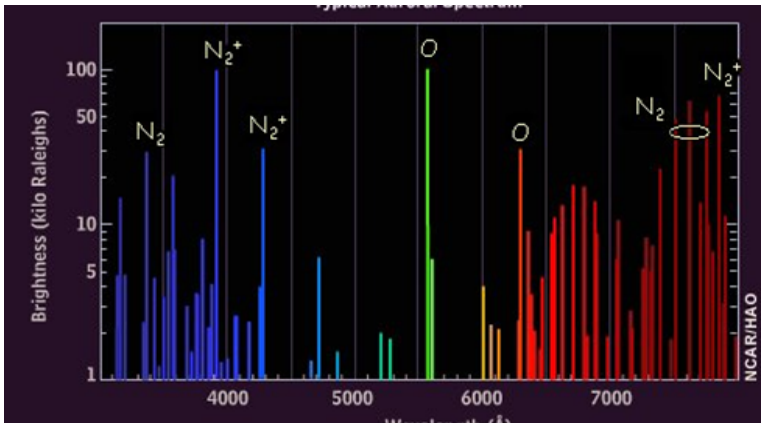

Figure 2.6: Aurora emission line model (source HCAR/HAO)

2.2.4 Auroral lights and other natural emissions

Besides light sources outside the atmosphere (stars, planets, Sun) GOMOS measurements are affected by sources inside the atmosphere. These include natural

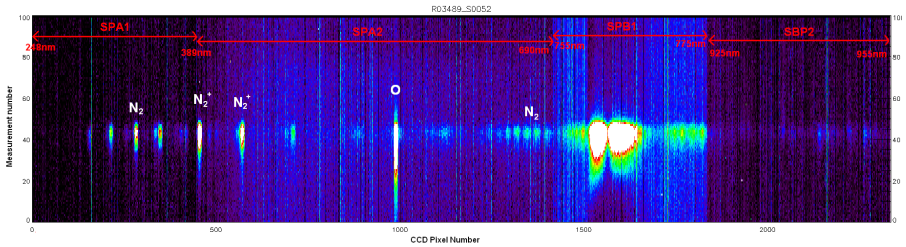

Figure 2.7: GOMOS upper background band map (measured intensity vs. spectral pixel number vs. measurement number) for star S052 in orbit R03489 (30 october 2009, tangent point latitude = 70°). This is a full dark (illumination flag 0) observation. Measurement number is related to the tangent point altitude (first measurement = 153 km, last measurements =11 km). Most of the emission lines presented in the model of 2.6 are also visible on the GOMOS observation. The lines are broader than the model because of the width of the spectrometer slit (10 pixels). Very strong O_2 emission is visible in the SPB1 spectrometer. This emission line is present in all GOMOS observations, even when not contaminated by auroral sources. However, its intensity is increased each time an aurora occurs.

emissions and auroral lights.

GOMOS measurements are affected by auroral emissions in the polar region observations. The spectral signature of the auroral light has several emission lines located in the UV, visible and near IR. The most intense line is the green line, located at 557.7 nm. It is due to the emission of atomic oxygen. Atomic oxygen can also emit in the red part of the spectrum (main line at 630 nm). Several lines in the purple/blue part of the spectrum (main at 391nm and 427.8 nm) are due to N_2^+. N_2 has several lines in the near UV (<390 nm). N_2 and N_2^+ have also several lines in the active red (around 670 nm) and in the Near Infra-Red (>700 nm) While aurora are produced at high altitude, they can appear in the spectrum of low tangent altitude GOMOS measurements. The line of sight of a measurement always goes through the upper atmosphere even if the tangent point is low and thus can be contaminated by auroral emission,

An auroral light detection algorithm has been built, based on the presence of the green line, but is currently not integrated in the processing chain. In bright, twilight and stray-light illumination conditions, the main auroral emission lines are eliminated from the central band by the estimated central background correction. However, this correction may not be accurate enough: the interpolation law between upper and lower band (for computation of the estimated central background) is exponential and there is no reason why the aurora line intensity should follow an exponential law with altitude. Auroral emission light also appears in full dark occultations (see example in Fig. 2.7). For this illumination condition, the central band is not corrected of the estimated central background for the spectrometer A (UV+visible). Some investigations are on-going in order

to estimate the impact on the retrieval of species.

2.3 Propagation of stellar light through the atmosphere

In the case where the source is point-like, the Beer-Lambert law alone is not able to explain observed transmissions. A parallel ray bundle from the star will be strongly disturbed by refraction in the atmosphere. Specifically the following effects have been observed:

1. Chromatic bending of rays
2. Refractive dilution
3. Scintillations

A nearly exponential decrease of the atmospheric air density leads to bending of rays coming from a star. The bending angle increases with decreasing tangent altitude. Refraction in the atmosphere transforms parallel incident rays into a diverging beam. This results in dilution of the related intensity and at large distances in so-called central flash (Fig. 2.4).

The refracted path is determined from the equation:

$$\frac{d}{ds}(n\frac{d\vec{r}}{ds}) = \nabla n. \tag{2.3}$$

The satellite position and the stellar direction provide the boundary conditions. The source term is produced by the gradient of the refractive index n.

The refractive dilution can be described by the following equation:

$$T_{\text{dil}} = \frac{1}{1 + L\frac{d\alpha}{dz}} \tag{2.4}$$

where L the distance between the satellite and the tangent point and α the refraction angle.

The air density always contains irregularities that are generated by internal gravity waves and turbulence. Their characteristic scales range from few kilometres down to a dissipation scale, which is typically smaller than 1 m. The stellar flux observed through the atmosphere exhibit fluctuations (called scintillations) that are caused by these air density irregularities. Largest scale irregularities (associated with internal gravity waves) are strongly stretched in horizontal direction. The interaction of stellar light with these structures can be well described in the geometric optics approximation. It can be treated as random focusing and defocusing of light beams. For description of scintillations that are caused by small-scale irregularities generated by isotropic turbulence, the diffraction theory is appropriate.

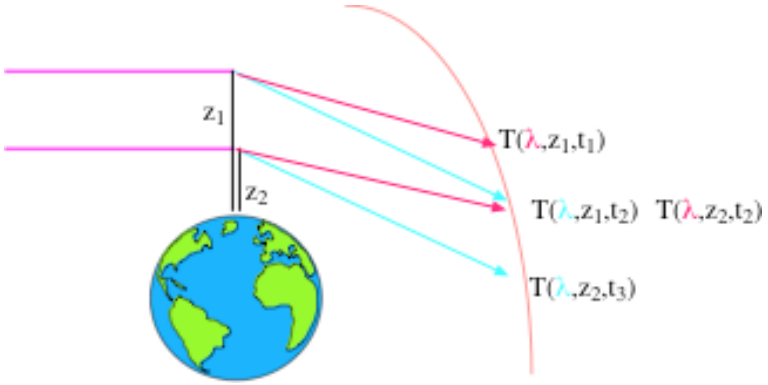

Figure 2.8: Chromatic refraction and its impact on detection times of different colours.

The dependence of the refractive index of the atmosphere on wavelength leads to a spatial separation of rays of different colours (Fig. 2.8). A multi-wavelength measurement of a stellar spectrum through the atmosphere cannot therefore be attached with an unique ray connecting the satellite and the star. If we describe rays by their tangent heights, we see that at a given time a measurement will be characterised by a range of tangent heights. If we want to attach one tangent height we have to combine data from measurements from different tangent heights.

The refractive effects discussed above are not restricted to the stellar occultations in the Earth's atmosphere. In fact they all have been detected and exploited in the data retrieval of stellar occultations of planetary atmospheres (see Ref. [8, 12]).

The attenuation of the light due to absorption and scattering can be accurately described by the well-known Beer-Lambert is law. For the wavelength region where GOMOS is measuring (250 nm-952 nm) the principal absorbers are O_3, NO_2, H_2O and O_2, and the main scatterers are neutral density and different aerosol particles. Inside quite narrow wavelength regions there are also contributions from NO_3, OClO and BrO. The integration follows along a refracted path.

2.4 Propagation of solar light through atmosphere

Solar light reaches GOMOS in bright limb conditions and also when the Sun is just below the horizon (twilight). The quality of the GOMOS measurements in bright limb depends on the ability to subtract the solar signal from the stellar signal. Even if the solar signal appears as nuisance for the main data analysis, it can be used to retrieve atmospheric information at higher level in the GOMOS

data analysis.

The total solar intensity obeys the radiative transfer equation:

$$\frac{dI(\lambda, s, \Omega)}{ds} = -\sigma(\lambda, T(s))\rho(s)I(\lambda, s, \Omega) + \frac{\sigma(\lambda)\rho(s)}{4\pi}\int P(\Omega, \Omega')I(\lambda, s, \Omega')d\Omega' \tag{2.5}$$

For simplicity we have assumed only one scattering constituent (density ρ, scattering cross section σ) and moreover we have assumed that it is non-absorbing. The boundary conditions include the incoming flux from the Sun and the albedo of the Earth at ground. The function P is the scattering phase function.

The single scattering solution for Eq. 2.5 can be computed in a straightforward manner:

$$I_{scat}(\lambda, \ell, t) = I_{Sun}\int_{\ell} T_{solar}T(s)(\sigma_R(\lambda)P_R(\theta)\rho_{air}(s) + \sigma_a(\lambda)P_a(\theta)\rho_a(s))ds \tag{2.6}$$

Here T_{solar} is the transmission along the solar path to the scattering point s, T is the transmission along the line of sight (ℓ) from s to the observing point (GOMOS), P_R and P_a are the scattering phase functions for the Rayleigh and aerosol scattering, respectively, and finally θ is the scattering angle.

The single scattering contribution is usually the dominant term in the radiance but in some cases its contribution can be as low as 50% of the total (see Ref. [22, 23]).

2.5 Detection of light by the GOMOS instrument

2.5.1 GOMOS instrument

GOMOS is a medium resolution spectrometer covering the wavelength range between 250 nm and 952 nm (see Fig. 2.10 and Ref. [6, 24]). Spectrometers A1 and A2 cover the UV-visible wavelength region 248–690 nm with 1416 pixels with the spectral width 0.31 nm. The spectral resolution is 0.8 nm. The spectrometer B1 covers 755–774 nm with 420 0.045 nm wide pixels. The spectral resolution is 0.13 nm. The spectrometers B2 covers 926–954 nm with 500 0.052 nm wide pixels. The spectral resolution is 0.13 nm.

The high sensitivity requirement (stars are weak sources of radiation) down to 250 nm has been a significant design driver leading to an all reflective optical system design for the UVIS part of the spectrum and to functional pupil separation between the UVIS and the NIR spectral regions (thus no dichroic separation of UV). Due to the requirement of operating on very faint stars (down to magnitude 4) the sensitivity requirement to the instrument is very high. Consequently, a large telescope (30 cm x 20 cm aperture) had to be used to collect sufficient signal and detectors with high quantum efficiency and very

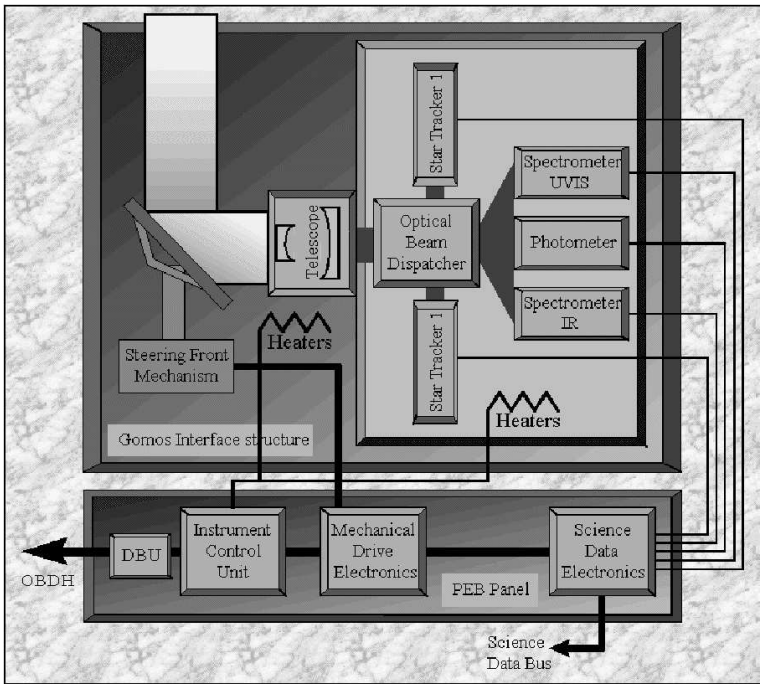

Figure 2.9: GOMOS instrument block diagram.

low noise had to be developed to achieve the required signal to noise ratios. In addition, in order to use the entire star signal, a slitless spectrometer design had to be chosen. The price that had to be paid for this design is that a highly performance pointing system had to be used to keep the star image fixed at the input of the spectrometers in order not to degrade the spectral resolution and the spectral stability.

The star tracker is sensitive inside the range 600-1000 nm and it is capable to keep the stellar spectrum fixed with an accuracy of a 1 pixel. The star tracker is able to follow a star down to 5-20 km. The altitude limit depends on the qualities of a star, the state of the atmosphere (e.g., clouds), and the limb illumination condition. GOMOS observes only setting stars. Acquisition of a setting star is much easier than a rising star (refraction) and to get both modes was impossible due to demanding visibility requirements in the platform design.

The main instrument requirements are summarised in Table 2.1 and the instrument layout is shown in Fig. 2.9 and 2.10.

2.5.2 Imaging properties of GOMOS

The GOMOS optical layout is shown in Fig. 2.11. To describe the imaging properties of GOMOS we divide the imaging chain into two parts. The first part starts from the outermost surface of the GOMOS optical chain and ends at

Table 2.1: **The main instrument requirements for GOMOS**

Requirement	**Value**
Occulting stars characteristics	Visual magnitude range: Max. -1.6 to min. 2.4 to 4 for stars with 30,000K and 3000K temperature respectively
Spectral range of the spectrometer	250 - 675 nm, 756-773 nm and 926-952 nm
Spectral sampling 0.3 nm in UVIS, 0.05 nm in NIR	Spectral resolution 1.2 nm in UVIS, 0.2 nm in NIR
Spectral stability knowledge in dark limb	0.07 nm in UVIS, 0.016 nm in NIR
Photometer spectral windows and sampling rate	470-520 nm and 650-700 nm 1 kHz sampling rate
Short term radiometric stability (over 150 s)	1%
Linearity	1%
Pointing stability	Better than 40 microradians peak-peak
Number of occultations per orbit	45 on average under nominal conditions, i.e. approximately 920,000 occultations during the 4-year mission
Angular coverage	-10 deg. to +90 deg. with respect to the flight direction. Thus, large instrument angular range observability

the slit plane. The second part is from the slit plane to the grating and finally to the detector surface. The first part can be written as:

$$I(u, v, \lambda, t) = I_0(\lambda, t, \vec{s}_0) S(u, v, \vec{s}_0) \tag{2.7}$$

The first factor is the incoming intensity which depends on wavelength, time and its direction of approach. The second factor indicates how the telescope transfers light from the front surface to the slit plane where (u,v) are the coordinates. The size of the slit is 120 μm in the horizontal or spectral direction and 200 μm in the vertical or spatial direction. The stellar image is much smaller and the slit is, therefore, actually not needed for the stellar imaging i.e., we have actually a slitless instrument. The slit is, however, needed to reduce the background radiation in bright limb measurements.

The intensity on the detector can be written as a mapping from the intensity on the GOMOS slit plane as follows:

$$I(x, y, \lambda, t) = \int\int I(u, v, \lambda, t) h(x - x_0 - d(\lambda - \lambda_0) - u, y - y_0 - v) du dv \tag{2.8}$$

Here h is the impulse response function and (x_0, y_0) the reference position. The figure 2.11 shows the imaging and spectroscopic scheme used.

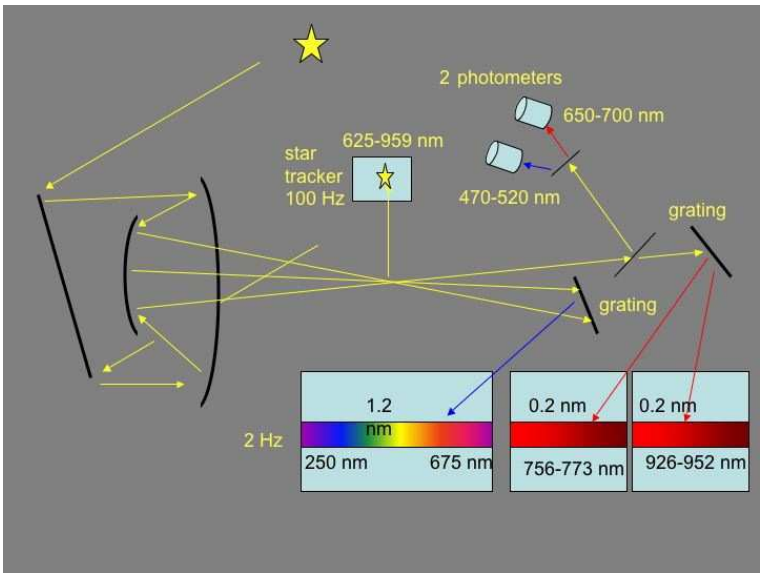

Figure 2.10: GOMOS instrument layout.

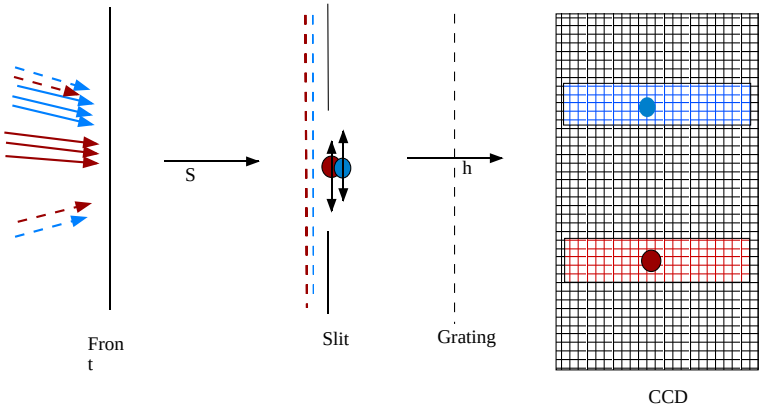

Figure 2.11: GOMOS imaging. The stellar light (solid lines) falling onto the GOMOS front surface comes as parallel ray bundles where the direction of approach depends on the wavelength. The background is coming from all directions. In the slit plane, stellar light with one wavelength is imaged into a small spot and its position varies rapidly as GOMOS intercepts different regions in the non-uniform intensity field. There is also motion due to pointing noise. All these motions are mapped onto the CCD plane where they are seen as wavelength shifts and wandering in the spatial direction.

2.5.3 Detection properties of GOMOS

The GOMOS data are produced when the intensity in Eq. 2.8 produces electrons in the CCD pixels. Nominally several pixels are binned in the spatial direction and charges are allowed to accumulate 0.25-0.5 seconds. The resulting net charge is transferred to the electronics where it is amplified and digitised. The final result which we see as counts is:

$$N = G(\sum \int\int\int\int\int\int\int I_0(\lambda, t, \vec{s}_0) S(u, v, \vec{s}_0) Q(x, y, \lambda) \\ h(x - x_0 - d(\lambda - \lambda_0) - u, y - y_0 - v)\, du\, dv\, dx\, dy\, d\lambda\, dt\, d\vec{s}_0) \quad (2.9)$$

The amplification and analog to digital transformation is described by the function G. The summing goes over the binned pixels. The integration over x and y are over the pixel surface. The integration over the input directions is needed because refraction in the atmosphere breaks the parallel ray coherence. The detection efficiency of individual pixels are described by the quantum efficiency function $Q(x, y, \lambda)$. In addition to the signal produced by the input light, there is generation of dark charges as well as the read-out noise.

Chapter 3

Level 0 and level 1b data processing

The main goal of the GOMOS level 1b processing is to estimate a set of geolocated spectral transmission functions along horizontal line of sights using stellar spectra measured by the GOMOS spectrometers. This so-called full transmission function will serve as basic data for the level 2 processing where profiles of atmospheric constituents are to be determined. Spectrometer data, as well as photometer data are therefore corrected for instrument dependent factors, as well as some atmospheric factors (scintillations, emissions at the limb, ...). Fast photometer data are needed to correct spectrometer data from scintillation.

Even if the GOMOS measurement method is a self-calibrating measurement method, several calibration-type corrections are needed. The self-calibration is taking care of the general slow changing radiometric drifts but many pixel-level details are not included. Outliers connected to bad pixels and cosmic rays are corrected.

Since the launch of ENVISAT, all the CCD pixels have suffered from particle radiation and became 'hot': their dark charge exceeds the value measured on ground, at the same temperature, by a significant amount. This general increase contribute to a higher DC also variable within hours. For this reason, at each orbit one special observation of a Dark Sky Area (DSA) is dedicated to the mapping of the Dark Charge.

3.1 Preprocessing of level 0 product

This level includes a simple set of operations where the orbit based Envisat data are separated into individual data sets, each covering one occultation. A special case occurs for tangent occultations that are stored in two individual packets and here they are combined to form a single occultation. In this stage the star catalogue product is used.

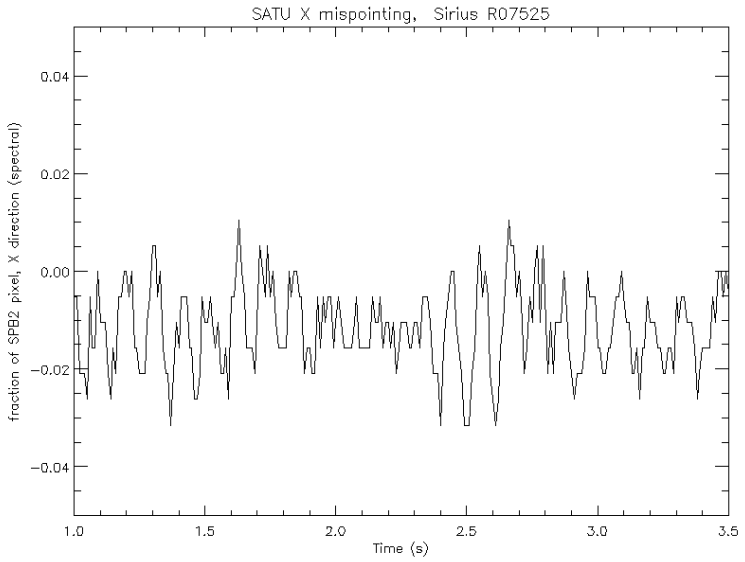

Figure 3.1: SATU (Star Acquisition and Tracking Unit) output data at 100 Hz at the beginning of the occultation in the X (spectral) direction. The unit of mispointing is fraction of the horisontal size of the B2 spectrometer pixel (20 μm): when the image of the star is moving on the SATU CCD detector, it is also moving on all spectrometers. Abscissae is time in seconds after the start time of the occultation.

3.2 Level 1b: wavelength assignment, geolocation and datation

3.2.1 Wavelength assignment

Two operations are performed: the nominal wavelength assignment is carried out using the calibration auxiliary product and the pixel wise spectral shifts are identified using the star tracker data. The nominal wavelength assignment corresponding to a perfect tracking of the star during the measurement is provided by the spectral assignment of one CCD column and by the spectral dispersion law of the spectrometers read in the calibration auxiliary product. Spectral shifts due to vibrations and imperfect tracking are estimated using the pointing data history produced by the SATU (Star Acquisition Tracking Unit). These shifts are used to spectrally assign each CCD column during each spectrometer measurement.

The SATU output provides the shift in two directions (axes): X (horizontal direction) which represents a spectral shift, and Y (vertical direction) which is a physical (spatial) shift. A mean SATU output data is computed at a frequency of 2 Hz and is used to compute the physical and spectral shifts of the star signal

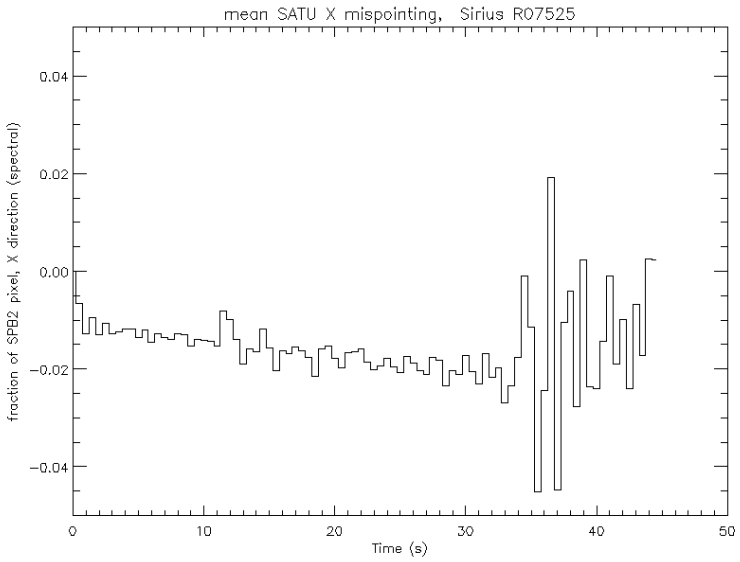

Figure 3.2: Shifts from SATU for the whole occultation in the X (spectral) direction. The unit of mispointing is fraction of the horisontal size of the B2 spectrometer pixel. The size of one GOMOS B2 spectrometer pixel is 27.0x20.0 μm: 27.0 μm along the spatial direction and 20.0 μm along the spectral direction.

on the spectrometer CCD arrays. Figure 3.1 presents the SATU output data in Y direction (physical) between 1.0 and 3.5 seconds (SATU output frequency is 100 Hz) in fraction of B2 CCD lines (or pixels). The mean physical shift (2 Hz) expressed in fraction of B2 CCD lines (or pixels) is plotted on Figure 3.2.

3.2.2 Geolocation

A complete geolocation calculation is carried out. Several different factors contribute to the geolocation:

- Orbit of the satellite
- Shape of the Earth
- State of the atmosphere (to compute the refraction of stellar light)
- Stellar co-ordinates

In the absence of refraction, the GOMOS line-of-sight (LOS) is defined by the direction of the star and the location of the Envisat satellite. The line of sight varies from 28° to 22° below the horizontal. The equivalent elevation angle of the instrument telescope varies from 62° up to 68° (the average 65°

corresponds roughly to the top of the atmosphere). As a result, for a 28° LOS, a positioning error ΔL "along track" (along the orbit) will produce an error Δz for the altitude of the LOS tangent height :

$$\Delta z = \Delta L \cos 28^\circ \approx 0.5 \Delta L \tag{3.1}$$

Therefore, GOMOS retrieval accuracy requires a good accuracy of the orbit knowledge (about 50 m), absolute timing of measurements and direction to the star. This latter must take into account the proper star motion, the parallax effect (which is small), and the aberration of light. The aberration depends on the time of the year, because of the orbital velocity of the Earth along its orbit: 30 km/s, giving a maximum aberration angle of 10^{-4} radian. This angle, projected on the limb, would yield an error altitude of about 300 m if not accounted for.

The orbit information can be obtained from the Envisat orbit propagator where the initial data are included in the Level 0 data. Depending on the time delay of the processing with respect to the measurement, there may be also more accurate orbit data available. The shape of the Earth is approximated by the well-known model WGS84 (see Technical Report [RD1]).

For the near real time processing, made within 3 hours after the measurements (for the production of Fast Delivery Products), the atmospheric profile is computed from the ECMWF 24 hour forecast made the day before for levels up to 1 hPa and completed by the climatological MSIS90 model above 1 hPa. The final processing is using ECMWF analysis up to 1 hPa and MSIS90 above 1 hPa. In both cases, a continuous density profile is built up, satisfying the hydrostatic law. Also, the geopotential height (the reference for models) is converted into geometric altitude, necessary for the GOMOS geolocation. Because of atmospheric refraction, the light from the star to GOMOS does not follow a straight line. A full ray tracing is performed through the atmosphere to compute the exact path of the stellar light. The approximation applied in this calculation is that there is no contribution from density gradients other than the ones in the plane determined by GOMOS, the star and the Earth centre. An example of the effect of refraction is shown in Fig 3.3 presenting the altitude of the tangent point during an occultation.

The refraction is computed at each point along the path, taking into account the atmospheric model, and the index of refraction which varies with wavelength according to the Edlen's formula (3.2):

$$n = 1 + \frac{10^{-6}}{1.00062}(83.4213 + \frac{24060.30}{130 - \lambda^{-2}} + \frac{159.97}{38.9 - \lambda^{-2}}) \tag{3.2}$$

where the wavelength λ is expressed in micrometers. See Edlen's paper [25] for reference on the formula (3.2). The overall multiplicative factor 1/1.00062 was introduced in order to account for 'real gas' deviation from the law of perfect gases (see Technical Note by F. Dalaudier [RD2])

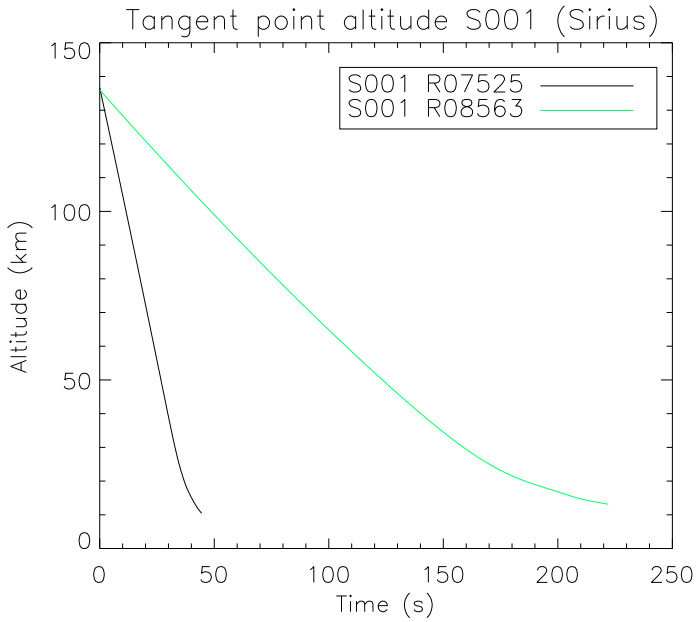

Figure 3.3: Tangent point altitude as a function of time. The refraction effect is to slowdown the vertical velocity of the LOS for altitudes below 25km. Two occultations of Sirius are plotted on this figure: the black curve occultation is a short one which lasts about 45 seconds while the green curve occultation is a long one which lasts about 220 seconds

3.2.3 Computation of the occultation obliquity

For the analysis of the geometry of an occultation, we need to know how the line of sight moves within the atmosphere. More specifically, the effect of isotropic (non-stratified) turbulence can be corrected only if the line of sight moves vertically through the atmosphere. The velocity of the line of sight, perpendicular to itself, varies between 3.4 km/s for a direct occultation, to about 8 km/s for a tangent one. The velocity of the atmosphere, due to the rotation of the Earth, varies between 0 and 0.5 km/s. Consequently, it is not negligible and must be taken into account.

The obliquity is defined here as the angle θ between the motion of the line of sight (with respect to the atmosphere) and the direction of the Earth's center. In the calculations the refraction of the line of sight is ignored (the altitude where the obliquity is calculated is sufficiently high so that the refraction is still negligible). On the other hand, the maximal perturbation effect of the 'isotropic' turbulence is observed between 20 and 50 km (depending on the geometry of the occultation and the considered constituent). The altitude chosen to calculate the obliquity is fixed to 35 km for any occultation. In case of tangent occultation,

if this altitude is never reached, the obliquity can be arbitrary fixed to 90°. The flattening of the Earth is also ignored since the direction of the Earth center can differ slightly from the local vertical (at the tangent point). In an 'Earth fixed' (rotating) reference frame, the direction of the star is not constant, and the line of sight does not stay parallel to itself. For this reason, it is easier to perform the calculation within an inertial geocentric reference frame and to correct the velocity of the line of sight from the velocity induced by the Earth's rotation. The velocities will be projected onto the fixed plane Π containing the origin (the Earth center) and perpendicular to the star direction (the line of sight).

In oder to calculate the obliquity we need the following steps[1]. Without Earth's rotation the velocity of point Q: $\mathbf{U}_Q = \mathbf{(S \times V)} \times \mathbf{S}$ and the direction of Earth center (from Q): $\mathbf{- Q} = \mathbf{- (S \times P)} \times \mathbf{S}$. Subtraction of Earth's rotation :Projection of $\mathbf{W}$ onto plane Π : $\mathbf{U}_E = \mathbf{(S \times W)} \times \mathbf{S}$. The relative velocity (within Π) is : $\mathbf{U}_R = \mathbf{U}_Q\mathbf{-U}_E$.

The obliquity is calculated through a scalar product with unit vector $\mathbf{S}$

$$sin\theta = (u_R \times q) \cdot S \tag{3.3}$$

The angle being calculated through its sinus, its sign is well determined. As the analytical formula shows, the obliquity varies in the same direction as the azimuth. The name 'obliquity' is in agreement with the fact that an occultation with a vanishing obliquity is vertical (within the atmosphere). It is not oblique at all.

Figures 3.4 and 3.5 show how the GOMOS measurements probe the atmosphere in short and long occultations. We have shown the movement of the tangent point in latitude-longitude values and the latitude-longitude values of ray tracing paths. From the geometry we know that points around the tangent point contribute strongest to the horizontal columns. In the short occultations the tangent point is almost stationary in latitude-longitude coordinates. In the long occultations the movement of the tangent point can be more than 10 degrees in latitude and longitude.

3.3 Level 1b: spectrometer data processing

The data processing requires a good knowledge of instrument characteristics (dark charge, wavelength calibration, wavelength resolution,...) based on ground characterisation and additional in-flight measurements.

Since GOMOS collects data on the day side as well as on night side, one major step in the Level 1b processing is to disentangle the light which comes from the star and the light which comes from the solar illuminated limb (background). GOMOS is equipped with three bands of measurements (portions of the CCD array), two devoted to the background vertically above and below

[1] $\mathbf{S}$: direction of the star (unit vector, no dimensions, fixed), $\mathbf{P}$: position of the satellite, $\mathbf{V}$: velocity of the satellite, ω: Earth rotation vector, $\mathbf{Q}$: projection of the satellite position in the plane Π : $\mathbf{Q} = \mathbf{(S \times P)} \times \mathbf{S}$, $\mathbf{W}$ velocity due to Earth rotation at point $\mathbf{Q}$: $\mathbf{W} = \omega \times \mathbf{Q}$

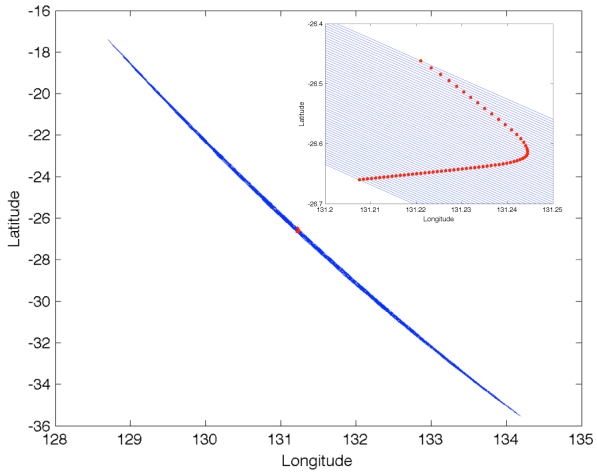

Figure 3.4: Geographical coverage of a short GOMOS occultation.The duration of the occultation is 44 s and the obliquity 3.9. The red line, hardly discernible in the centre of the main figure, gives the latitude-longitude values of the tangent points below 100 km. The inserted figure shows the zoom of the tangent point location. The blue lines show the latitude-longitude projections of the the ray tracing paths below 100 km. Figure is from ref. [19].

the star (in the spatial domain). Given a good radiometric calibration of GOMOS, the absolute limb radiance spectrum can be extracted from the GOMOS background measurements. These limb radiances may in turn be interpreted in terms of aerosol loading, and ozone and other constituent distributions, and this is why they belong to the standard Level 1b products.

3.3.1 Detection and correction of anomalies and outliers

3.3.1.1 Saturated samples processing

In this module, the saturated pixel values are detected, flagged and removed from further processing.

3.3.1.2 Bad pixels processing

With this processing step, bad pixels samples are flagged. The missing data are created with a median filtering using the values of the neighbour measurements in the spectral direction.

Bad pixels are specified from a bad pixels list coming from the calibration database. The initial list is defined by on-ground characterisation. This list is regularly updated by the GOMOS in-flight calibration process (Uniformity

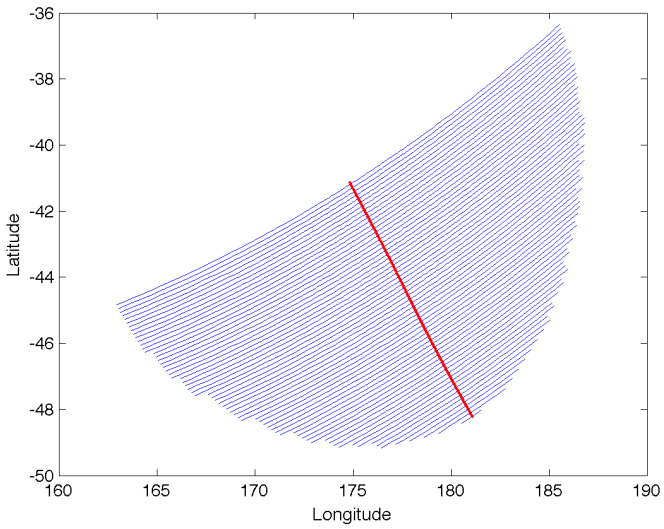

Figure 3.5: Geographical coverage of a long GOMOS occultation. The duration of the occultation is 164 s and the obliquity 83.5. The red line gives the latitude-longitude values of the tangent points below 100 km. The blue lines show the latitude-longitude values of the the ray tracing paths below 100 km. The occultation starts from the right lower side and moves to the centre of the figure. Figure is from ref. [19].

monitoring mode). There is no on-line detection of bad pixels but the cosmic rays correction processing may also prevent unexpected bad pixels (a bad pixel creates a local sharp variation which may be detected by the cosmic rays correction processing). Once bad pixels are identified from the bad pixel list, two complementary actions are performed:

1. The bad pixels are flagged and are ruled out from any further processing.
2. New values in ADU are interpolated from neighbouring pixels by a median filter, mainly for cosmetic use (more beautiful data display) because they are not used further in the processing.

This step does not increase the information content of the data.

3.3.1.3 Cosmic ray processing

The CCD detectors are sensitive to high energy particles, which may come from the Earth's radiation belts or from the interplanetary/interstellar medium. They may also be generated by radioactive decay of impurities in the spacecraft and GOMOS materials. A cosmic ray will produce an additional charge in a

single pixel, or several pixels when the angle of incidence with respect to the surface of the CCD is small. This phenomena is seen in all space-flying CCDs.

The easiest way to identify a cosmic hit on a CCD is to take two images of the same scenery at a short time interval, and to compare them (by subtraction). A hit will appear, above the noise level, either in positive or negative, if it belonged to the first or the second image (cosmic hits are always positive, producing more electrons in one or several contiguous pixels). When only one image is acquired (full 2D CCD image), the standard way to identify automatically the cosmic hits is to pass a median filter (i.e., 3 x 3 pixels) on the image and to compare the content of each pixel to the median value of the window centered on this pixel.

For GOMOS, we do not get a 2D CCD image, rather, we have several blocks of lines electronically binned together (three per CCD), at each exposure of 0.5 s. Therefore, a pseudo-image is reconstituted for each measuring band of CCDs: the top line of the image being the first measurement in the band, the second line being the second measurement, and so on for a whole occultation. We assume here that a pixel has only a very small chance to be hit by a cosmic ray during two consecutive measurements. In a sense, we are using both standard methods at the same time (comparison of two nearby exposures, reduced here to a single line per CCD band). Of course, one cosmic hit cannot be distinguished from noise if it is smaller than a few times the noise level.

This abnormal CCD response is eliminated using a median filtering in both spectral and temporal directions. The content of each pixel is compared to the median value of the filtering window. A cosmic hit is detected if this difference is greater than a given threshold. This threshold value depends of the gain index of the CCD. Threshold values for the four different gain index are read in the Level1b processing configuration product. The value of the corresponding sample is replaced by the computed median value. It is flagged and not used further in the processing. In bright limb condition cosmic ray processing is disabled.

3.3.1.4 Modulation correction

It was discovered in flight that the ADC offset level shows a small variation, with a reproductible pattern in successive samples and an amplitude of 0.5 to 1.5 ADU (changing with the specific CCD A1 or A2). This is called a modulation. If the illumination condition is not in bright limb condition, a correction of this modulation is performed for spectrometer A1 and A2 (just after the cosmic rays correction). For spectrometer B, the modulation is not corrected.

There is a slow change in the amplitude of this modulation, which is monitored. The change in the amplitude of the modulation through the whole mission is small enough not to be taken into account in the processing chain. Modulation signal is characterised in [RD3].

3.3.2 Corrections to measured signal (ADU)

3.3.2.1 Conversion into the number of measured electrons

A conversion of the ADU values into number of electrons is performed in each spatial band of the spectrometers A and B, including non-linearity correction. This conversion needs the value of the CCD gain (in e/ADU) for each electronic chain (for the nominal and the redundant chains) and for each programmable gains (4 gains per spectrometer). The non-linearity correction of the electronic chain is performed in this processing step.

$$D^{LIN} = (D - d_0) f_{nlin} \tag{3.4}$$

$$N^{RO} = D^{LIN} \times G \tag{3.5}$$

Here D is the spectrometer pixel value in ADU (after saturated samples, bad samples and cosmic ray processings), f_{nlin} is the non-linearity factor, G is the electronic gain factor, d_0 is the off-set and N^{RO} is the number of electrons collected by the pixel. The non-linearity factor can be determined by using so-called linearity monitoring mode of GOMOS where the integration time can be specified between 0.25 to 10 seconds. Originally it was measured on the ground in the instrument characterisation process. The CCD pixels' sensitivity becomes non-linear when they are approaching the saturation. Study on bright limb data have shown that the non-linearity correction does not work adequately. Consequently, we have decided to lower the threshold value of the saturation in order to remove pixels which are in non-linear regime. Those pixel are now considered as saturated and are discarded in the Level 2 spectral inversion.

3.3.2.2 Dark charge correction

This is a major change to Level 1b algorithms established prior to the launch. During ENVISAT flight the pixels became 'hot', with a higher and variable dark charge (the GOMOS CCDs are not cooled). In the absence of light, the level of Dark charge is much higher than on the ground, and it is highly variable from one pixel to the next (so-called DCNU, dark charge non-uniformity). Also, its average level for one pixel may change, with a time scale that can vary from a few seconds to several hours. This phenomenon is called RTS (Radio Telegraphic Signal). Therefore, a new observing strategy was set up. At each orbit, when ENVISAT is near the equator in deep night, the instrument is pointed towards a dark area of the sky. Instrument collects, therefore, only the dark charge on all CCDs and all 3 bands. It is averaged to produce a dark charge spectrum. It is used to correct all other occultations in the same orbit. Presently there is some evidence that the long time between the dark current measurement and its use for corrections may be too long for accurate correction.

Dark charge accumulation depends strongly on the detector temperature. This temperature varies along the Envisat orbit. The variation is corrected using detector thermistor values. The accuracy of the thermistor is 0.41K which means a possible 6% error in the dark current removal. In order to correct this

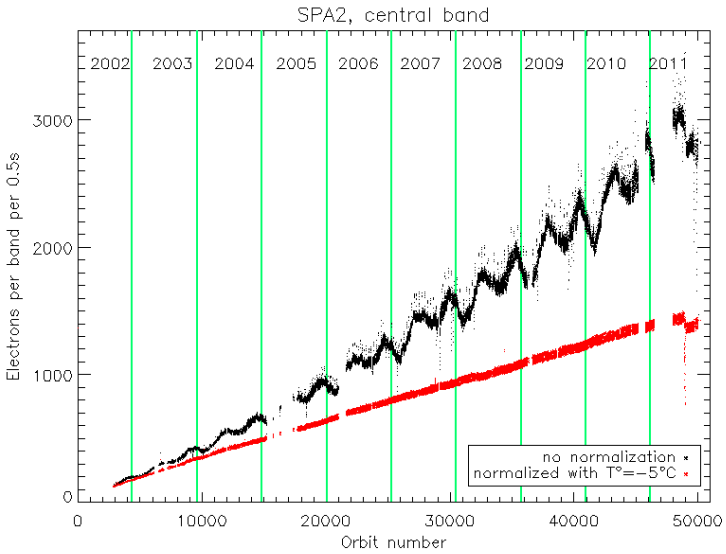

Figure 3.6: Mean dark charge for spectrometer A2. The black curve shows seasonal variations due to the position of the sun and thus to the change of the temperature of the CCD. The red curve has been obtained by normalizing the black curve at a reference temperature of -5°C. Therefore, the red curve shows that an increase of dark charge (independent of the temperature) still exists. These are called hot pixels. An annealing of GOMOS CCD was performed near orbit 49000 (July 2011) as an attempt to reduce the number of hot pixels. By this procedure, we reduced successfully the amount of hot pixels by about 8% as clearly visible on the red curve (sudden 8% decrease between pre and post orbit 49 000 data). During the annealing procedure the temperature was raised at level where the normalization law is not valid anymore which explain the local downward peak of the red curve at the time of the annealing (on the black curve, it would be seen as a very high DC level, but it is out of the Yaxis range).

bias the signal levels of the upper and lower band after dark current removal at the end of the occultation are used to estimate the residual bias in the central band. This can be used only in dark limb measurements where the upper and lower bands should include only noise at the end of the occultation. For detailed analysis, see [26].

The corrected number of electrons N^{DC} is :

$$N^{DC} = N^{RO} - DC \tag{3.6}$$

Figure 3.6 shows the increase of the mean DC with time for the spectrometer A2.

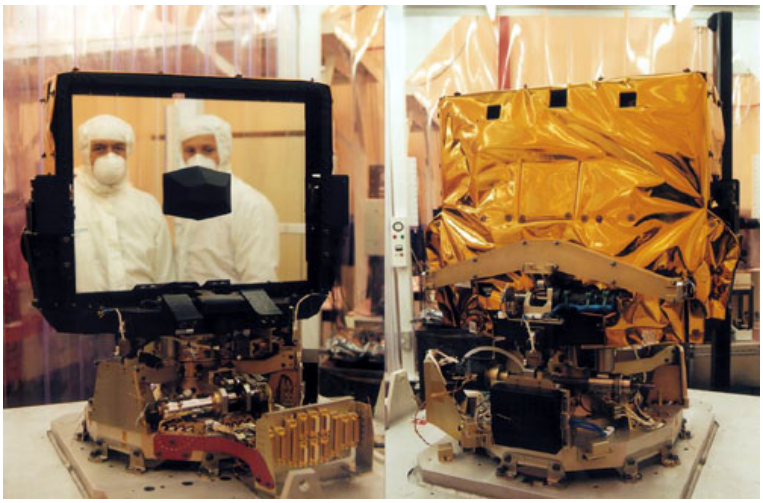

Figure 3.7: GOMOS main mirror.

3.3.2.3 Correction of the SFA mirror reflectivity

The plane mirror (see Fig. 3.7) of the SFA (Steering Front Assembly) is oriented in such a way that the line of sight is reflected in a fixed direction, along the telescope axis. The reflectivity of the mirror varies with wavelength and the angle of incidence, which is $\geq 25°$. The incidence angle depends on the elevation and azimuth angles. Since the incidence angle varies by a few degrees during one occultation, it is important to correct for the effect. Otherwise the transmission ratio of two star spectra measured with a different incidence angle would be biased. Observations of star Sirius (S0001) were obtained at a variety of azimuth and incidence angles, allowing to build a LUT (Look Up Table) of the reflectivity as a function of wavelength. The variation of reflectivity is assumed to be a linear function of the angle of incidence.

3.3.2.4 Internal and external straylight correction

The internal straylight is the light coming from the region of FOV (Field Of View) delimited by the slit, but whose photons do not fall on their nominal position on the CCD. It is mainly generated by the grating as scattered light, and it is most manifest as light from the star collected in the background bands. As such, it contaminates only the background bands and the measurement of the background, not the star itself. At present time, no correction of the internal straylight is implemented. The corresponding software module exists, but it is not activated.

The external straylight is the light which makes its way through the slit, though its origin is outside the nominal FOV of the slit. There are mainly two sources of external straylight. One is the solar light scattered by some ENVISAT

Table 3.1: **PCD illumination conditions**

Illumination flag	**Illumination**	**Requirement**
0	full dark	Not in bright limb nor twilight nor straylight conditions.
1	bright	SZA at tangent point $< 97°$ for at least one measurement with ALT at tangent point < 50km.
2	pure twilight	Not in bright limb and SZA at tangent point $< 110°$ for at least one measurement with ALT at tangent point $<$ 100km.
3	pure straylight	Not in bright limb and SZA of ENVISAT $< 120°$ for at least one measurement.
4	twilight + straylight	Not in bright limb and both conditions for twilight and for straylight are verified.

hardware into the baffle and optics of GOMOS. The other is coming from the limb, or the nadir, sun-illuminated. The external straylight of solar origin does not go through the ozone layer, and therefore contains some UV even at maximum ozone absorption wavelength (255 nm). At present time, no correction of the external straylight is implemented. Still, geometrical computations are performed to characterize the illumination conditions of GOMOS, ENVISAT, and the tangent point of occultation at the limb at a reference altitude (the nominal value is 50 km). The illumination condition is given in the flag index 'PCD_ILLUM' which is stored in the Level1b product. There are five different illumination conditions presented in Table 3.1. This index may be also used as a guide for the straylight contamination. The global distribution of measurements in the five illumination flag classes is shown in Fig. 3.8. The genuinely dark limb occultations belong to the class 0.

3.3.2.5 Vignetting correction

At the extreme range of azimuth (negative angles), the plane mirror is vignetting (partially masking) a part of the collecting area for the IR spectrometer B. In this module the degraded performance of the IR spectrometer at some azimuth angles (nominally from -10° to -5°) is taken into account by a vignetting factor correction.

3.3.2.6 Flat field correction

The sensitivity of each pixel is different from its neighbours, determined by PRNU (Pixel-to-pixel Response Non Uniformity). The PRNU of all pixels was

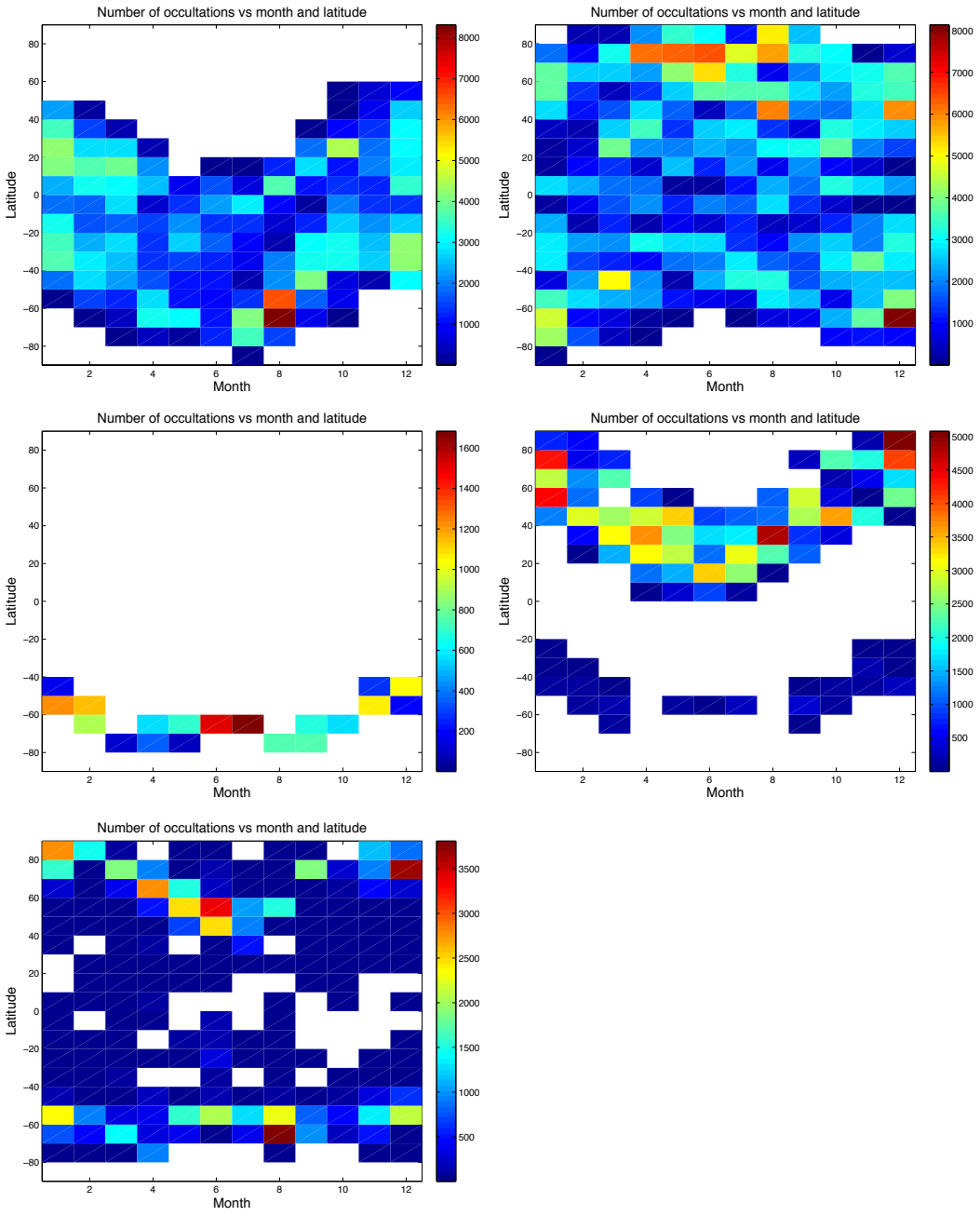

Figure 3.8: The distribution of measurements in latitude-time grid during 2002-2012 with different illumination classes. Classes are in the following order: Top row 0 and 1; middle row 2 and 3; bottom 4.

determined in-flight. It is most important for spectrometer B1 (O_2, 760 nm) and B2 (H_2O, 936 nm). During one spectrometer integration time, the image of the star spectrum is moving on the CCD due to refraction effects and residual pointing errors, so that pixels with a different response will contribute to the signal measurement. The signal at band level will depend on the exact position on which the star spectrum is formed. This position is known from SATU data (SATU is the star tracker), at 100 Hz sampling rate. Coupled with a refraction model and with the instrument Point Spread Function, the SATU information allows to estimate the current effective PRNU of the CCD pixels of the Central band, which contains the star spectrum image.

The scintillations measured from photometers data allow to take into account fast brightness variations of the star spectrum, for each position of the star spectrum at 100 Hz within a sample time (0.5 s).

The signal at band level will depend on the exact position on which the star spectrum is formed. This position is known from SATU data (SATU is the star tracker), at 100 Hz sampling rate and from the nominal location of the star on the CCD. Satu-Y data provides the star vertical displacements (during the occultation) around the nominal location.

Studies on in-flight data have shown that the response inside one pixel is not uniform. Therefore, the PRNU correction should consider this sub-pixel sensitivity (also called intra-pixel) in order to be complete. An sub-pixel PRNU (iPRNU) map for spectrometer B2 has been computed from Sirius observations. These Sirius observations have the particularity to cover a big range in the spatial direction (satuY = [-30μrad, +30μrad]) even at high altitude thus not contaminated by water vapor. The iPRNU map gives the sensitivity response of the CCD as a function of the spectral pixel number (500 pixels in B2) and of the vertical star displacement (SATU Y) on the CCD.The resolution of this map for the vertical displacement is 1μrad which is about 26 times lower than the size of one pixel and the range of the map is [-30μrad, +30μrad]. The iPRNU correction makes use of this map and, as for the initial PRNU correction, of the SatuY data and of the nominal location of the star. The spatial PSF is not used as it is already "included" in the iPRNU maps. Studies on in-flight data have shown that the nominal location of the star on the CCD is not constant. It is changing with time and also with the star. LUTs of nominal location as a function of time have been computed for the 9 brightest stars in spectrometer B2 (NIR) and are used in the correction algorithm. Spectrometer A1, A2 and B1 iPRNU correction is not yet implemented as iPRNU map for these spectrometers have not been computed. Initial PRNU correction is still used for these spectrometers. iPRNU correction, especially for SPB1, should be considered in future baseline updates.

3.3.3 Separation of stellar and background signals

3.3.3.1 Central background estimate

The objectives of the central background estimation are to provide:

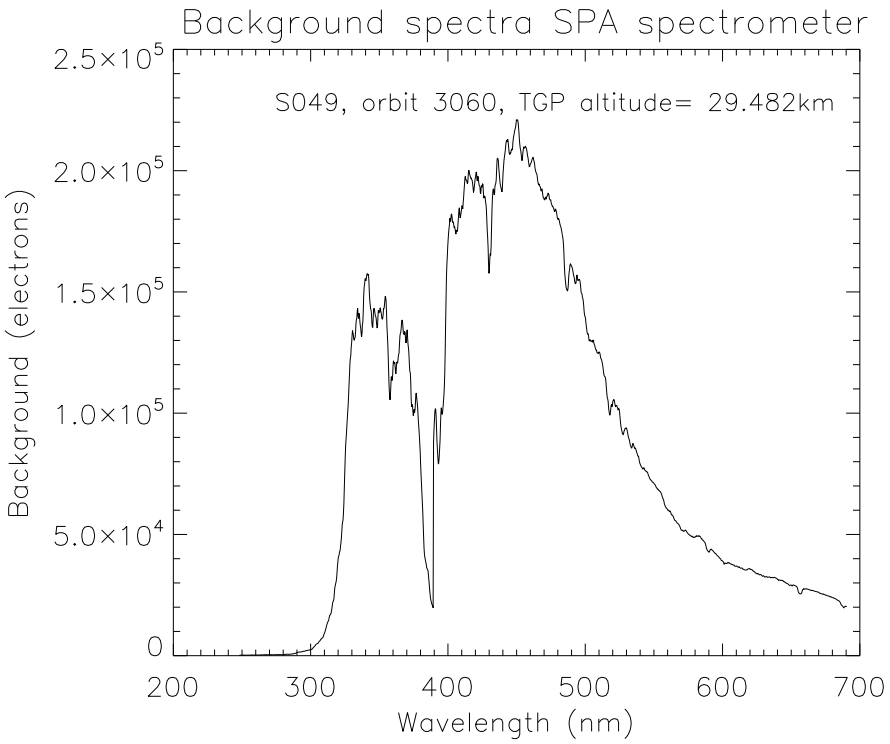

Figure 3.9: Estimated central background for a bright limb occultation. The minimum near 400 nm is due to instrumental sensitivity (part of the UV CCD is masked by the visible CCD). This minimum disappears when converting to physical unit applying the radiometric curve.

- an estimation of the background signal measured by the central band during the occultation. This signal will be subtracted from the measured central signal in order to get the star signal alone
- an estimation of the contribution of the background signal to the signal of the fast photometers
- an estimation of the upper and lower background corrected for flat fielding, to be stored in the GOMOS Limb Products.

Before the estimation a flat field correction is applied to upper (U) and lower (L) bands. The present software configuration includes three different methods for estimating the background contribution inside the stellar band:

1. No background estimation

$$N_c^{NST} = 0 \tag{3.7}$$

2. A linear interpolation between upper and lower bands

$$N_c^{NST} = N_L^{NST} + (N_U^{NST} - N_L^{NST})\frac{h_C - h_L}{h_U - h_L} \tag{3.8}$$

where $h_{L,U}$ are the tangent heights calculated by the geolocation for the upper and lower bands.

3. An exponential interpolation (this is the method currently activated in the processing):

$$N_c^{NST} = N_L^{NST} + (\frac{N_U^{NST}}{N_L^{NST}})^{\frac{h_C - h_L}{h_U - h_L}} \tag{3.9}$$

For methods 2 and 3 the central background is obtained as :

$$N_C^B = N_C^{NST} Q_C \tag{3.10}$$

whereQ_C is the pixel response non-uniformity (PRNU) (= flat-field) at band level for the central band.
Once the central background is estimated, it is subtracted from the central band to get the true stellar signal. It is performed in all conditions, except in the full dark limb conditions for Spectrometer A (UV-Vis). In full dark conditions, it is negligible, and subtracting it would add the noise of the Dark Charge of the two background bands. For Spectrometer B (IR), it is not negligible, even during the night. There is indeed an O_2 emission around 760 nm, and OH emissions near 940 nm.
On the day side, the limb brightness is large. It saturates the spectrometers usually at altitudes lower than 26km so that the background correction is no longer feasible. When any of the upper, central or lower band is saturated, the corresponding column is flagged and not used in the following processings. Figure 3.9 shows an example of the estimated central background for a bright limb occultation.

3.3.3.2 Star signal computation

The star spectrum is computed from the central band measurement and from the estimation of the central background. First, the number of electrons due to background is directly subtracted from the central band signal which includes both star and background signals. Then, the result of this operation is corrected for flat-fielding in order to get a valid estimation of the star spectrum. The nominal location of the star signal on the CCD, the SATU output data, the photometer engineering data and the photo-response non uniformity are used to correct for the non uniformity (flat-fielding), as described in section (3.3.2.6). Figure 3.10 shows an example of the occulted star spectrum (central band) at low tangent altitude.

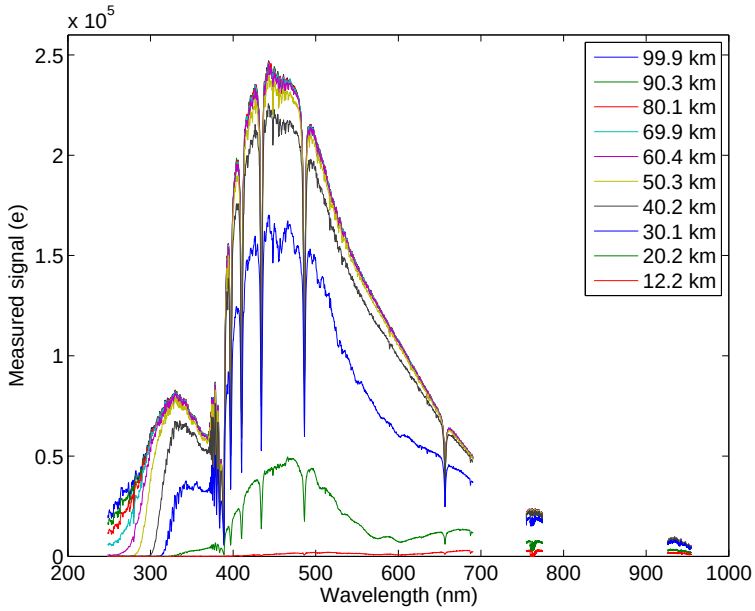

Figure 3.10: Sirius spectrum measured through the atmosphere at several tangent altitudes. Figure is from ref. [19]
.

3.3.3.3 Slit correction

If the star image in the slit deviates unexpectedly too much from the nominal central position the decreased slit transmission blocks part of the signal. Because the position of the star image can be estimated from the star tracker, a look-up table can be used to recalibrate the signal:

$$N^S = \frac{\hat{N}^S}{\bar{\tau}_{slit}} \tag{3.11}$$

where the slit transmission is the calculated blocking factor.

3.3.3.4 Reference star spectrum computation

A reference spectrum of the star (Figure 3.11) is measured at each occultation by averaging 10 measurements obtained above a threshold altitude of 105 km. At lower altitudes, there is absorption in the UV part of the star spectrum. Depending of the start altitude of the occultation, there may be less than 10 measurements above the threshold altitude. In this case, the reference spectrum will be calculated by averaging less than 10 measurements.

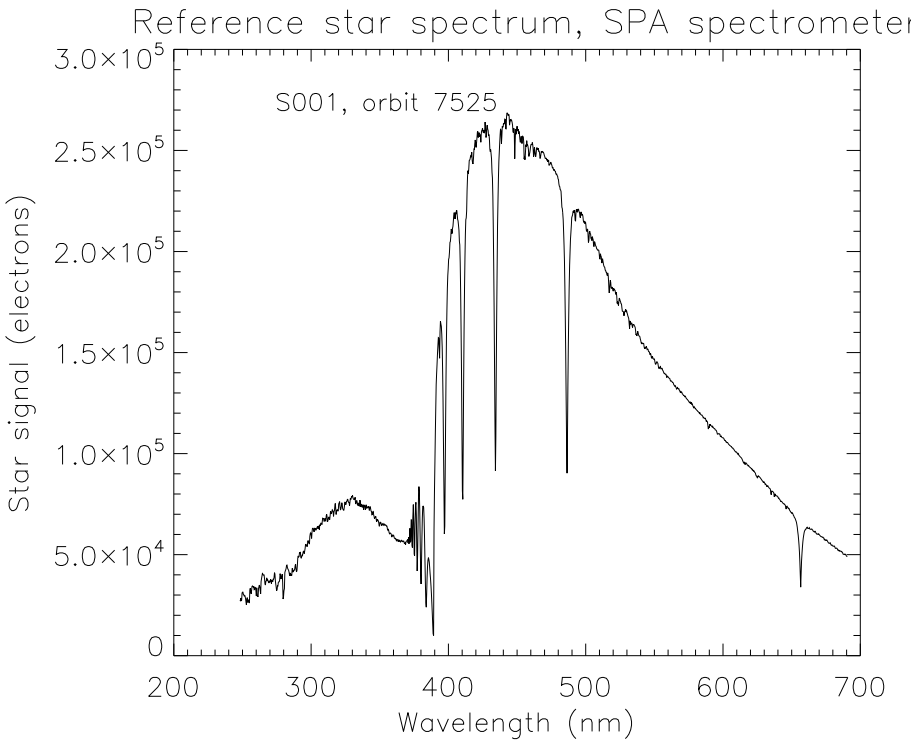

Figure 3.11: Reference star spectrum of Sirius in electrons computed by averaging the 10 first star spectrum measurements (central band) of the occultation.

3.3.4 Full transmission calculation

The Level 1b processing is finalised by calculating the so-called full transmission:

$$T = \frac{N^S}{N^{REF}} \tag{3.12}$$

The full transmission (Figures 3.12, 3.13, 3.14) is computed as the ratio of the estimated star spectrum (N^S)to the reference spectrum of the current occultation (N^{REF}). All the spectra used in this processing must be spectrally aligned before computation. The wavelength assignment of the star spectrum is re-sampled over the nominal spectral grid before the computation of the transmission.

The covariance function (Figures 3.15, 3.16) gives an estimation of the errors due to both instrument measurements and the level 1b processing. These functions are used by the level 2 algorithms. The error on the star spectrum is computed as the square root of the quadratic sum of the noise due to the instrument itself during the measurement and of the noise due to the level 1b processing. Noise due to instrument includes:

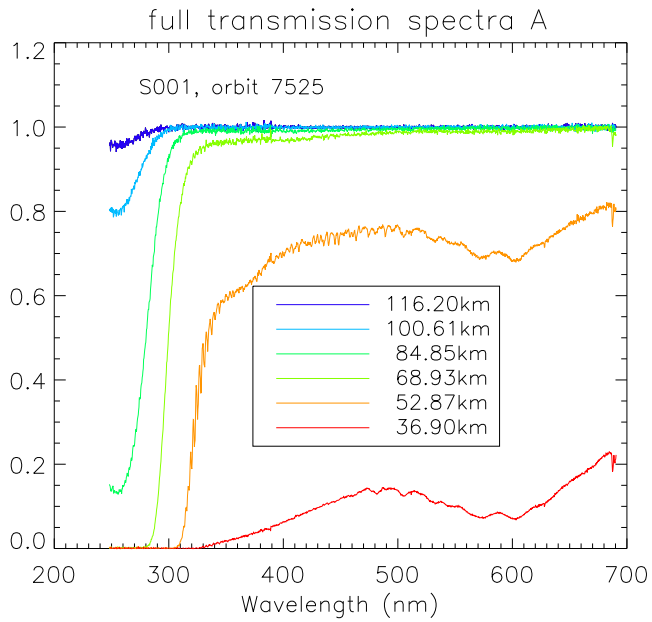

Figure 3.12: Full transmission spectra of spectrometers A1 and A2. The absorption of ozone is manifested in the UV, and also around 500-600 nm at low altitude (Chappuis band). Some features of NO_2 are also visible around 450 nm.

- Spectrometer electronic chain noise
- Shot noise expressed in electrons
- Quantisation noise due to the ADC

The noise due to the level 1b processing has several contributors:

- Dark charge removal
- Straylight removal
- Background corrections (which is the main contributor in bright limb conditions).

3.3.5 Error analysis

All the products issued from level 1b are given with error estimates. These estimates are calculated assuming that there is no modelling error and considering normal Gaussian error statistics. The pixelvise data are assumed to be independent on each other. We ignore all correlations between pixels even if

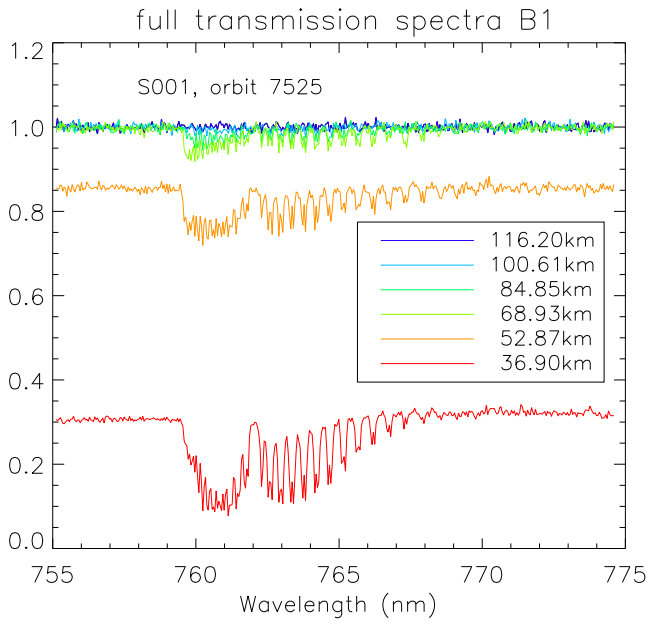

Figure 3.13: Full transmission spectra of spectrometer B1, dedicated to the measurement of molecular oxygen O_2.

Level 1b data processing may generate some. In the following the main error contributions for the main products are reviewed.

The error on any signal coming from CCD and processed is :

$$\Delta N = \sqrt{N + \Delta DC^2 + R^2_{read-out} + \frac{G^2}{12}} \tag{3.13}$$

The first component under the square-root is the photon noise, the second (ΔDC) is the noise associated with the dark charge removal, the third one is the read-out noise and the last one is the quantization noise.

The error on the backgound has been estimated simply by

$$\Delta B = \sqrt{|B_{est}|} \tag{3.14}$$

where B_{est} is the estimate of background signal in the central band. The error on the estimated stellar signal is

$$\Delta N = \sqrt{N_{meas} + (\Delta DC)^2 + R^2_{read-out} + \frac{G^2}{12} + (\Delta LP)^2 + (\Delta B)^2} \tag{3.15}$$

where ΔLP is the error associated to the subtraction of straylight, and ΔB is the error associated to the subtraction of background. At present, ΔLP is set to zero because the straylight correction has not been activated.

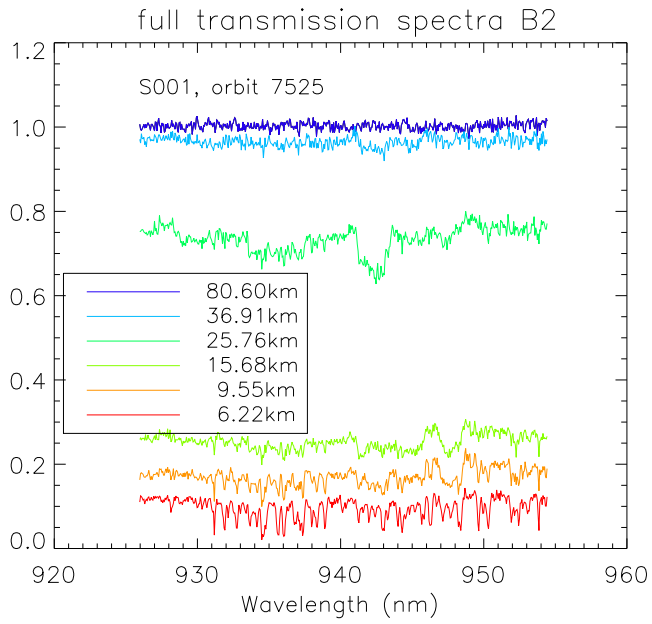

Figure 3.14: Full transmission spectra of spectrometer B2. This channel is dedicated to the measurement of H_2O. A big 'spectral' feature at 940-943 nm on the third curve from top (25.76 km of altitude) is spurious, and due to an imperfect flatfield correction. H_2O bands are very well observed in the troposphere (6.22 km of altitude).

The error on the reference spectrum is given by

$$\Delta N_0 = \frac{1}{p}\sqrt{\sum_{j=1}^{p} \Delta N_j^2} \tag{3.16}$$

where p=10 is the number of measurements averaged. The error on the transmission is then

$$\Delta T = T\sqrt{(\frac{\Delta N}{N})^2 + (\frac{\Delta N_0}{N_0})^2} \tag{3.17}$$

All these error estimation formulas have been validated by simulations and by in-flight statistical analysis of measurements.

3.4 Photometer data processing

The processing applied to the fast photometer samples is composed of the following steps :

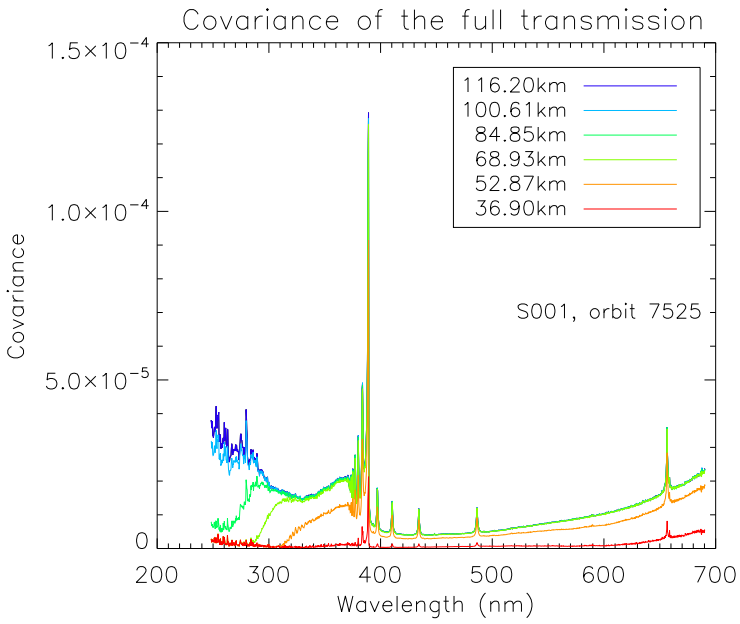

Figure 3.15: Variance of the full transmission (square of the error estimate) vs wavelength at several altitudes of the occultation. The variance is larger below 400 nm, where the signal is lower because a part of the UV CCD is masked by the visible CCD. Other spikes correspond to lower intensities in the bottom of Fraunhofer lines.

- Unfolding correction
- Saturated samples processing
- Non-linearity correction
- ADU to electrons conversion
- Spikes correction
- Dark charge correction
- Straylight correction
- Vignetting correction
- Background subtraction
- Flat-field correction

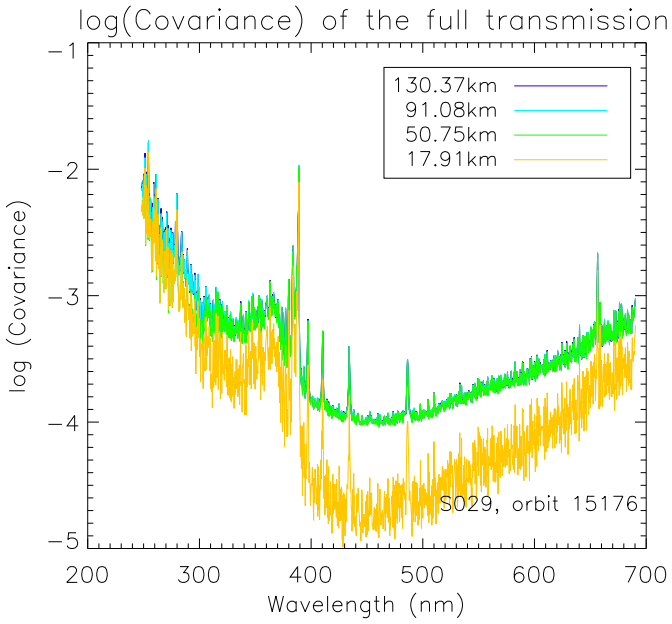

Figure 3.16: Same as Figure 3.15 for a faint star S029. Y axis is in logarithm scale.

Most of these processings are similar to the ones for the spectrometer samples, except the background subtraction that uses the estimated central background computed for the spectrometers as an 10.01 to remove the background contribution for the photometer samples. The error of the photometer signal is dominated by the shot noise, and the estimate is taken as the square root of the signal. Figure 3.17 gives an example of the blue photometer signal.

3.4.0.1 Unfolding of the photometer signal

Because of the 12 bits capacity of the on-board adder included in the photometer electronic chain, only the 12 least significant bits are written in the GOMOS packets (spikes, overflow and saturation are visible in the figure 3.18).

In case of overflow, the analysis of the temporal series usually allows to rebuild the original signal (unfolding algorithm). The current unfolding algorithm compares the local variation of the signal to a threshold. Figure 3.19 presents the results of the unfolding processing applied on the previous data. This figure shows that the correction of the spikes should be done after the unfolding correction. In the current processing, correction of the spikes is done before the unfolding correction leading to residual upward spikes (see time $>$ 15 seconds on Fig. 3.19).

However, in some circumstances (e.g. Sirius occultations with strong at-

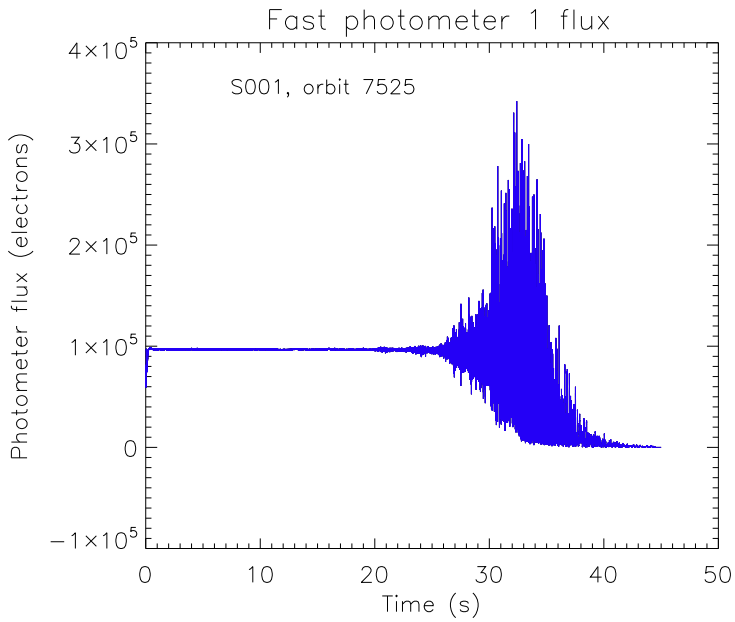

Figure 3.17: Blue photometer signal, the intensity is in electrons and it is plotted versus the time in seconds since the beginning of the occultation.

mospheric scintillation), the real variability of the signal flux can exceed this threshold, leading to false overflow detection.

An incorrect unfolding of the photometer signal has a negative impact on the scintillation/dilution correction of the transmission spectra (level 2 processing) thus on the quality of the species retrieval. Discontinuities of the NO_2 and air column density profiles have been observed at the altitudes of false reset corrections.

The analysis of the processed occultations leads us to definitely avoid applying the unfolding process for the occultations of the Sirius star or in case of full dark limb condition where the overflow is assumed to be only punctual.

3.4.0.2 Correction of the spikes

The photometer data are measured with a sampling rate of 1 kHz and each sample corresponds to a time integration of the light intensity during one millisecond (1 ms). For each spectrometer measurement (0.5 s), there is consequently 500 photometer samples for each photometer. However, the last sample of each series of 500 is obtained with a time integration of 0.9 ms (instead of 1 ms), thus producing a downward spike. This instrumental effect is corrected by dividing the value of the last sample in each series of 500 by 0.9.

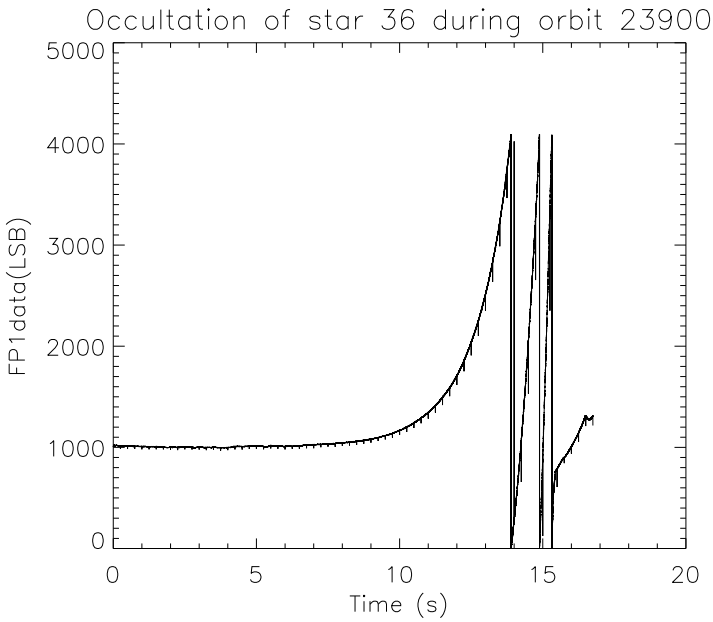

Figure 3.18: GOMOS FP1 data in bright limb condition showing several overflows. The intensity is in electrons and it is plotted versus the time in seconds since the beginning of the occultation. Downward spikes which need to be corrected by the processing are also visible.

3.5 Databases of level 1b processing

There are several databases associated to the Level 1b processing.

Level 1b processing configuration database contains all the configuration parameters and the thresholds used by the different algorithms of Level 1b processing chain as well as the parameters needed in the atmosphere model.

Instrument physical characteristics database contains the characteristics of the instrument which should not vary during its lifetime: CCD size, static spatial and spectral PSF, and other parameters.

Star catalogue contains for each of the 960 stars which could be occulted by GOMOS a number of informations: name, identification number in various catalogues, visual magnitude, position, parallax, proper motion (from Hipparcos catalogue), radial velocity, rotational velocity (which determines the Fraunhofer linewidths), spectral type, effective temperature, multiplicity, index describing the proximity of other nearby bright stars and other parameters.

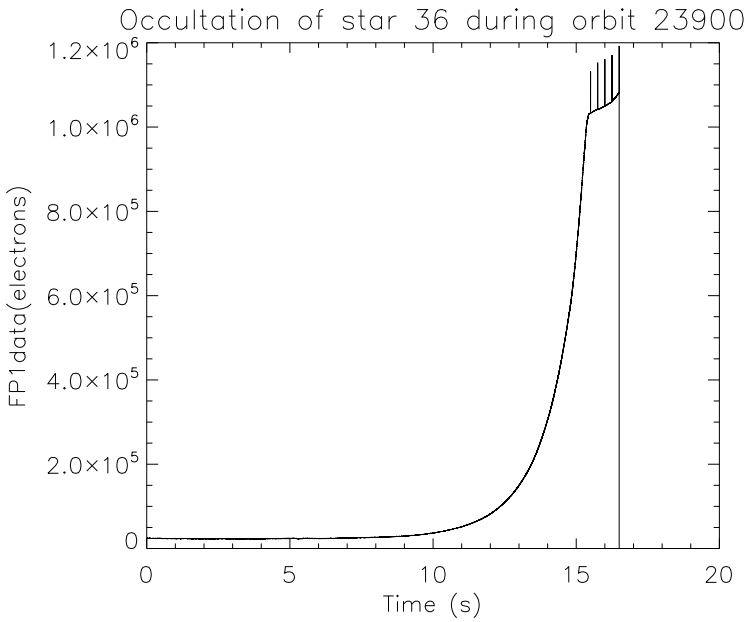

Figure 3.19: Unfolding process applied to the previous data (Fig. 3.18). Some spikes at high intensity appear not well corrected because the CCD is near saturation.

Calibration database contains (non-exhaustive list):

Absolute sensitivity of spectrometers and photometers chains, both for a point source and an extended source, as a function of λ.

Detailed spectral bandwidths

Gain factors of the CCD chains (number of electrons per ADU) and the read-out noise.

Flat Fields of CCDs

Intra-PRNU map of SPB2

Linearity curves of CDDs chains and bias levels

Matrices representing the DC for each pixel, as a function of temperature.

Calibration factors to allow SATU data interpretation

Housekeeping engineering calibration curves (i.e., for mirror angles).

All these data are extracted from the characterization measurements (on the ground) and from in-flight data, perfomed either with the standard mode of GOMOS operation (occultation) or with the dedicated monitoring modes. Some of the standard occultations are analyzed for monitoring the instrument (for

instance, the sensitivity is monitored with the signal delivered by stable stars). In addition to the standard occultation mode, GOMOS may be activated in one of several observation modes (Monitoring modes) dedicated to the monitoring of the instrument. There is the possibility to follow a fictitious star with a data format identical to the standard mode. In another mode, 33 lines of the CCD are transmitted every 6 seconds, allowing checking of the response of all individual pixels (which otherwise are merged together to form one spectrum). These monitoring modes are activated on request for checking the instrument quality and refresh the Calibration data base, on a regular basis. These modes need a special data processing which is performed off-line.

3.6 Additional reference documents

- RD1: NIMA Technical Report TR8350.2, *Department of Defense World Geodetic System 1984, Its Definition and Relationships With Local Geodetic Systems.*
- RD2: F. Dalaudier: Technical Note, *Formulae for the refractive index of air*, 1994
- RD3: A. Hauchecorne: Technical Note GOMOS-SA-TN-116, *Estimation of signal modulation in spectrometers A1 and A2.*

3.7 Level 1b data products

Level 1b data products are listed in Table 3.2. and the processing chain is shown in Fig. 3.20.

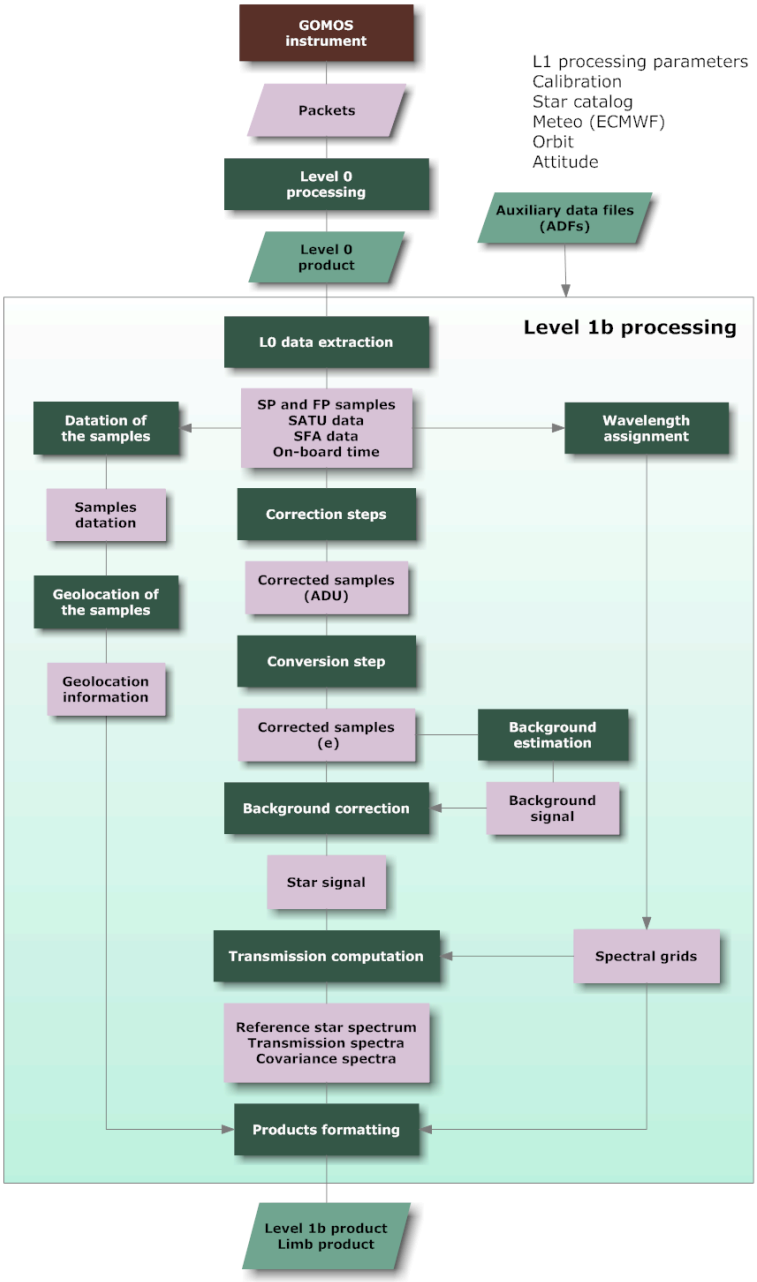

Figure 3.20: Level 1b processing

Table 3.2: **GOMOS Level 1b products.**

Name	**Description**
Transmission	Once per occultation
Reference star spectrum	Average of the 10 first spectra obtained during the occultation.
Reference atmospheric profile	This profile is extracted from a meteorological field analysis (ECMWF) combined with MSIS90 at P<0.1hPa.
Full transmission spectra and covariance	This spectrum is obtained by dividing each spectrum by the reference star spectrum. This transmission is not corrected for refraction effects or for variable PSF. Each spectrum is re-sampled on the wavelength pixel grid of the reference spectrum to get the transmission. The covariance is computed from analysis of S/N ratio. 2 Hz
Central background estimate and error	The estimated background contribution to the total signal in the central band, which was subtracted to yield the pure stellar signal. 2 Hz
Photometers data and error	Scintillation data expressed in electrons. 1 kHz
SATU data	The position of the centroid of the star image on the SATU CCD (Stellar Tracking Unit), which allows to know where to find each wavelength in the series of pixels and to know the spatial deviation of the star (used in PRNU and iPNRU corrections). 100 Hz
SFA angle measurements	Steering front assembly mirror: azimuth and elevation at 10 Hz
Nominal wavelength assignment of the spectra	The nominal wavelength of the centre of each pixel, valid for the whole occultation.once per occultation
Spectral shift of the star spectra	2 Hz
Geolocation and error	This includes both the position of ENVISAT spacecraft and the position of the tangent point of the LOS. 4 Hz
Limb product	once per occultation
Upper and lower background spectra and error	This product includes the background actually measured with the two external bands of CCD spectrometers, uncorrected and corrected for straylight and IR-vignetting.

Chapter 4

Level 2 retrieval

4.1 Introduction

The GOMOS Level 1 products that are used in the GOMOS Level 2 processing are:

- Transmission data (T^{obs})
- Photometer data (I^{obs}_{pho})
- Geolocational data ($\ell(\lambda, t)$)
- A priori atmospheric data ($\rho_{air}(\bar{r}), \mathrm{T}(\bar{r})$)

The main data are the transmission spectra at different tangent heights. Photometric data from the two fast photometers are used to correct the transmissions from the scintillation effects. Photometric data are also used to retrieve a high resolution temperature profile of the atmosphere. The geolocational and the a priori atmospheric data are necessary information in dealing with the refractive effects and in initialising the inversion. These data are partly replaced by new data from GOMOS Level 2 processing.

In the GOMOS Level 2 processing the data set processed at a time are the measurements from one star occultation. Even if some occultations would probe the same atmospheric region at successive orbits these occultations are treated separately. Therefore, the possibility to carry out some kind of atmospheric tomography by GOMOS has not been considered in the Level 2 processing (see Ref. [27]).

In the present GOMOS ground processing by ESA limb spectra from Level 1b are not used. There is an ongoing attempt to use these spectra for ozone retrieval (see Ref. [28, 29, 30]).

The geophysical retrieval strategy in the GOMOS Level data processing assumes that the measured transmission (produced by the GOMOS Level 1b processing) can be taken as the product of two transmissions:

$$T^{\mathrm{obs}} = T_{\mathrm{ref}} T_{\mathrm{ext}} \tag{4.1}$$

The transmission $T_{\rm ref}$ is due to refractive effects and the transmission $T_{\rm ext}$ is due to absorption and scattering processes in the atmosphere. The Level 2 processing aims first to estimate the refractive part using the fast photometer data and the geolocational data, and then to remove it from the measured transmission. The remaining transmission can then be connected to the atmospheric constituent densities, the retrieval of which is the main mission objective of the GOMOS instrument. As discussed in Chapter 3 this transmission can be written as:

$$T_{\rm ext} = e^{-\tau} \tag{4.2}$$

where the optical depth τ is given by:

$$\tau(\lambda) = \sum_j \int \sigma_j(\lambda, \bar{r}(s))\rho_j(\bar{r}(s))ds \tag{4.3}$$

There is no obstacle to an inversion strategy where we use Eqs. 4.2 and 4.3 to retrieve the constituent profiles. This approach can be called one-step inversion. The problem is the size of the input data and the number of the estimated parameters. Data consist of about 3000 spectral points (for the UV-VIS and IR spectrometers) at about 70 tangent altitudes. This means something like 210 000 data points for one occultation. We aim to retrieve at least 5 gases at the measurement levels i.e. we have at minimum 250 model parameters. The inversion problem size is dangerously large for operational retrieval (for studies of this so-called one-step inversion, see Ref. [31, 32]).

In the GOMOS Level 2 data processing strategy the following essential simplifications have been adopted in order to bring the inversion problem into a more manageable form (see Ref. [31, 28]).

1. Separate UVIS and IR spectrometer data analysis

2. Decouple spectral and vertical inversion problems as far as possible.

These simplifications allow us to perform the inversion in a sequential way. We still have to decide if we carry out the spectral inversion or the vertical inversion first. If the spectral inversion is performed first, as an intermediate result we produce horizontal column densities of different constituents $N_j(z)$. If the vertical inversion is performed first, as intermediate products we produce profiles of the absorption coefficients $k(\lambda, z)$. In the GOMOS ground segment it is chosen to perform the spectral inversion first because it leads to a rapid compression in the data volumes processed. The simplifications discussed above lead to some inaccuracies of the modelling but they are counteracted by performing iteration loops. After performing spectral and vertical inversion we perform the sequence again and so on. The different approaches for the Level 2 inversions, as well as for the processing of higher level products, are shown in Fig.4.1 (see also Ref. [11]).

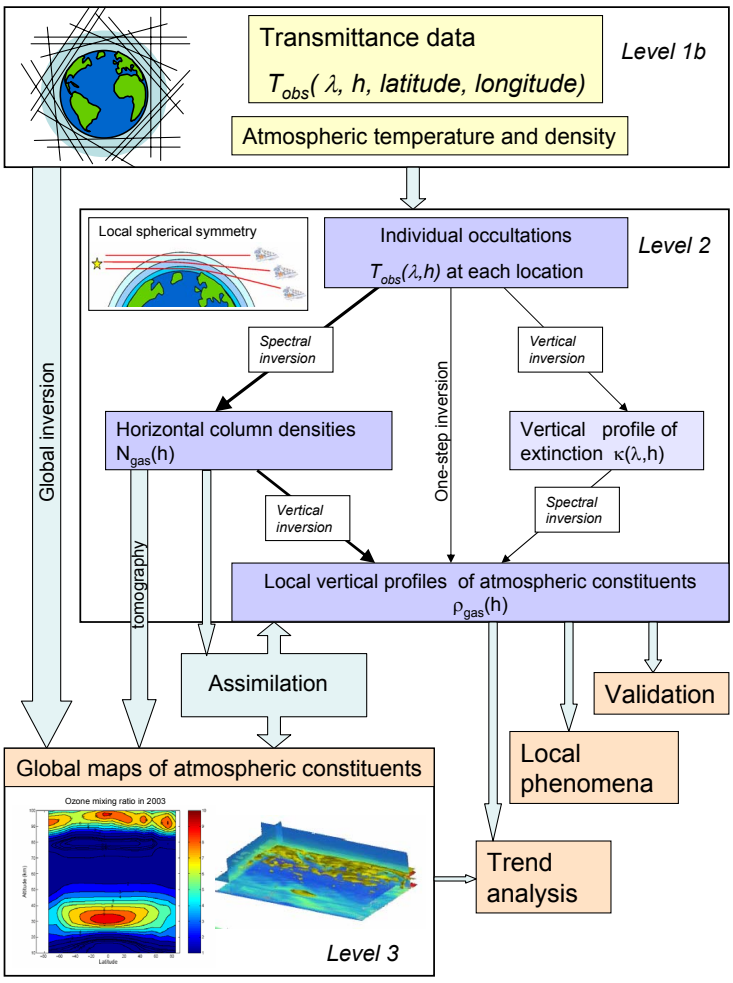

Figure 4.1: Strategy for the spectral and vertical inversion [33] . See text for explanations.

4.2 Refraction corrections

As already explained in Sec. 3.1, the refraction affects GOMOS measurements in various ways. The most obvious effect is the change in the geolocation of the light path connecting the satellite and a star. This can be taken into account by performing ray tracing calculations but it is further complicated by the chromaticity of the refraction. The ray tracing needs atmospheric data.

We use ECMWF (up to 1hPa) and MSIS90 (above 1 hPa) for this data. The other effects are generated by the variation of the air temperature and therefore also by the index of refraction. This causes a differential bending of the light rays in the atmosphere that results in a modulation of the intensity detected by GOMOS. In the GOMOS level 2 data processing a distinction is made between the smooth and fast variations of the index of refraction. The smooth variation can be calculated analytically whereas the fast variation is best described using GOMOS fast photometer data.

The objective of the refraction corrections is to provide a simple scheme that can be used to estimate the part connected to scintillation and dilution effects.

4.2.1 Dilution and scintillations

The scintillation and dilution correction process is based on the assumption that the modulation due to dilution and scintillation may be split in two independent terms:

$$T_{ref}(t) = T_{dil}(t)T_{sci}(t) \tag{4.4}$$

where T_{ref} is the transmission due to refractive effects, T_{dil} represents the dilution component and T_{sci} represents the effect of scintillation, assumed to be free of direct chromatic effect.

The following approach is assumed: T_{sci} is estimated using the signal of the fast photometer which has the highest signal to noise ratio. The principle is to minimise extinction effects in the photometer bands (the less extinct one is generally the red photometer). The estimation of this term is made with the assumption that all high frequency fluctuations in the photometer signal (if we except noise fluctuations) are due to scintillations and that fluctuations due to structures in vertical profiles of absorbing constituents affect only the low frequency part of the signal. This assumption is justified by the fact that the absorption depends on the integrated density along the line of sight, while the dilution is sensitive to the vertical second derivative of the integrated density. As a matter of fact high frequencies are enhanced by the derivation. T_{dil} is computed using a vertical profile of atmospheric density coming from an external atmospheric model.

The mean dilution is approximated by using the so-called phase screen approximation. In the framework of the phase-screen approximation, the effect of the extended atmosphere on the light wave passing through it is replaced by that of a virtual phase screen located at the tangent point. The refractive bending takes place at the screen. With this approximation the mean dilution can be written simply as:

$$T_{dil}(z,\lambda) = \frac{1}{1 + L\dfrac{d\theta(z,\lambda)}{dz}} \tag{4.5}$$

where L is the distance from the tangent point (screen) to the satellite and θ is the refractive angle of the ray. In the GOMOS level 2 processing the

refractive angle is taken from the ray tracing calculation. If the mean deviation is computed for the first time, the ray tracing calculation is the one performed in Level 1b. For subsequent calls (see Level 2 loops) the ray tracing may be performed again using the GOMOS generated atmosphere.

The scintillation transmission is calculated by:

$$T_{sci}(t) = \frac{I_{ph}(t)}{\overline{I}_{ph}(t)} \tag{4.6}$$

where the numerator is the photometer signal and the denominator is the smoothed photometer signal. The smoothing is performed by the Hanning filter (see Ref. [34]) over an adjustable time interval (in vertical distance the default value is about 3 km). The combined effect due to dilution and scintillations during one integration time of the spectrum (0.5 sec) is now given by:

$$\overline{T}_{ref} = \frac{1}{\Delta t}\int T_{ref}(t)\, dt = \frac{1}{\Delta t}\int_{\Delta t} T_{dil}(t) T_{sci}(t)\, dt \tag{4.7}$$

The transmission due to absorption and scattering can now be calculated by dividing the observed transmission by the estimated refractive part:

$$T_{ext}^{obs} = \frac{T^{obs}}{\overline{T}_{ref}} \tag{4.8}$$

It is important to note that, at this stage, we have transmission corresponding to tangent altitudes depending on wavelength. The chromatic effect is taken into account in the mean dilution term. The chromatic effect which is neglected in scintillation correction is the intensity normalisation resulting from difference in "duration" of the same structure when viewed at different wavelengths. In other words, the integration time in Eq. 4.7 is also wavelength dependent.

This algorithm assumes that the absorption does not contain high frequency components. The algorithm does not check the consistency between the atmospheric model (dilution) and the Rayleigh attenuation.

Two fundamental restrictions of the scintillation correction algorithm are depicted in Figs. 4.2 and 4.3. The algorithm does not correct so-called strong scintillations and it is not generally able to correct scintillations from isotropic fluctuations in the atmosphere. The correction for isotropic scintillations works only if the FOV of the instrument is in the orbital plane.

4.3 Chromatic refraction correction

During its path through the atmosphere, a light ray is refracted by the gradient of the index of refraction. This bending is dependent on wavelength. The smaller the wavelength, the greater the bending. It means that there is no single path through the atmosphere that could be attached to a light field detected at any given time by GOMOS.

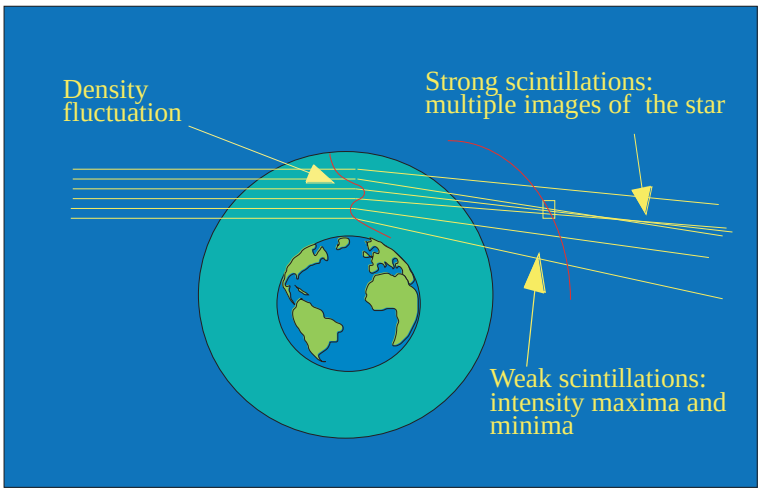

Figure 4.2: Strong and weak scintillations.

The goal of this algorithm is to correct the atmospheric transmission for the chromatic refraction. We calculate the tangent points corresponding to each pixel of each spectrum and then calculate the transmission for given tangent altitudes by performing linear interpolations between two acquisitions.

$$\widetilde{T}^{obs}_{ext}(z_j,\lambda) = rT^{obs}_{ext}(z_j,\lambda) + (1-r)T^{obs}_{ext}(z_{j+1},\lambda) \tag{4.9}$$

$$\widetilde{T}^{obs}_{ext}(z_j,\lambda) = (1-r)T^{obs}_{ext}(z_j,\lambda) + rT^{obs}_{ext}(z_{j-1},\lambda) \tag{4.10}$$

The first alternative is applied for wavelengths λ smaller or equal to the fixed reference wavelength and the second alternative to the rest. The coefficient r is the interpolation coefficient:

$$r = \pm\frac{z_j(\lambda_{ref}) - z_{j\pm1}(\lambda)}{z_j(\lambda) - z_{j\pm1}(\lambda)} \tag{4.11}$$

This module represents the first alternative method to correct the chromatic refraction effects. The second alternative is presented in connection to the transmission modelling.

4.4 Model developments

In the previous section we derived from Level 1b transmission the reduced transmissions (Eq. 4.8 or Eqs. 4.9-4.11) that should now be connected to the constituent densities in the atmosphere. Note that the transmission is measured in the horizontal direction and it bears no simple relationship to the vertical transmission that is the relevant quantity in discussions of UV-radiation threats.

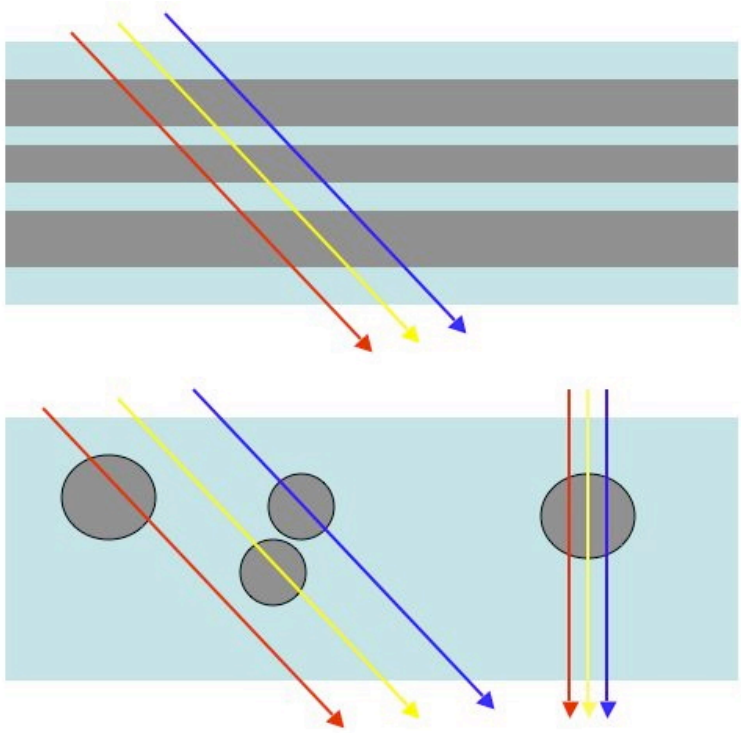

Figure 4.3: Anisotropic (top) and isotropic (bottom) density structures and the propagation of multicoloured light. The GOMOS scintillation correction works well for anisotropic structures. It can also handle isotropic structures if the occultation takes place in the orbital plane (the vertical ray bundle) but fails for oblique occultations (the tilted ray bundle).

However, these horizontal transmissions constitute an invaluable data set for the monitoring of the state of the stratosphere.

Unfortunately, there are still factors that make it necessary to perform further analysis before the connection between transmissions and the profiles can be worked on. These effects are related to the finite integration time of the instrument and to the finite spectral resolution of the imaging system, as well as the combined of effects of these two processes.

For a point source and with nearly ideal imaging we can write the model transmission as the following two-dimensional integral:

$$\bar{T}(\lambda, t) = \frac{1}{\Delta t} \int \int T_{ext}(\lambda', \ell(t, \lambda')) W(\lambda, \lambda', t)\, dt d\lambda' \tag{4.12}$$

where W is the instrument point spread function. It is time dependent because during the integration time the stellar image wanders in the slit plane and its image on the CCD plane does the same. This causes some spectral smearing.

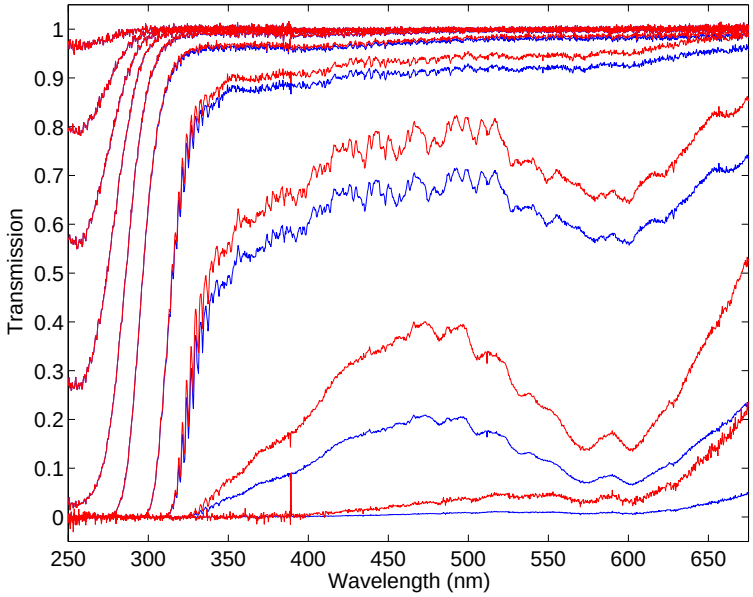

Figure 4.4: Level 1b transmissions (blue) and refraction corrected transmissions (red) at various altitudes. The altitudes and the star are the same as in Fig. 3.10. Figure is from ref. [19].

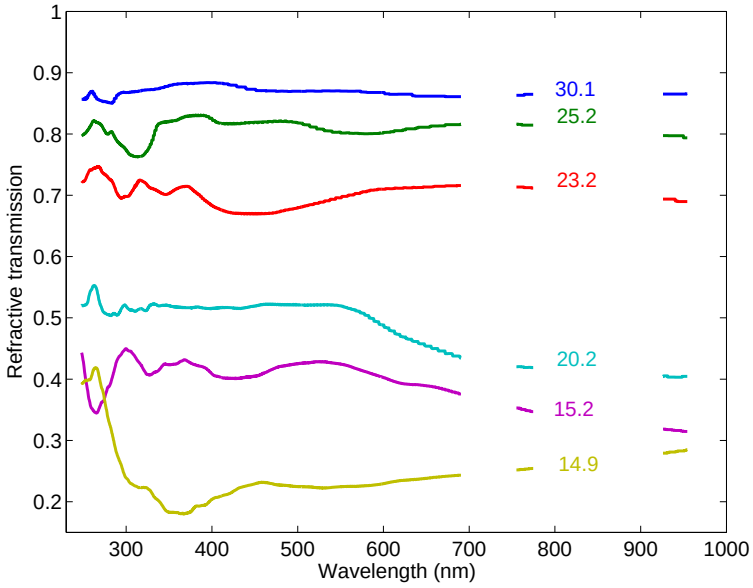

Figure 4.5: Refractive transmission at altitudes 14-16 km. The occultation is the same as in Fig. 3.10. Figure is from ref. [19].

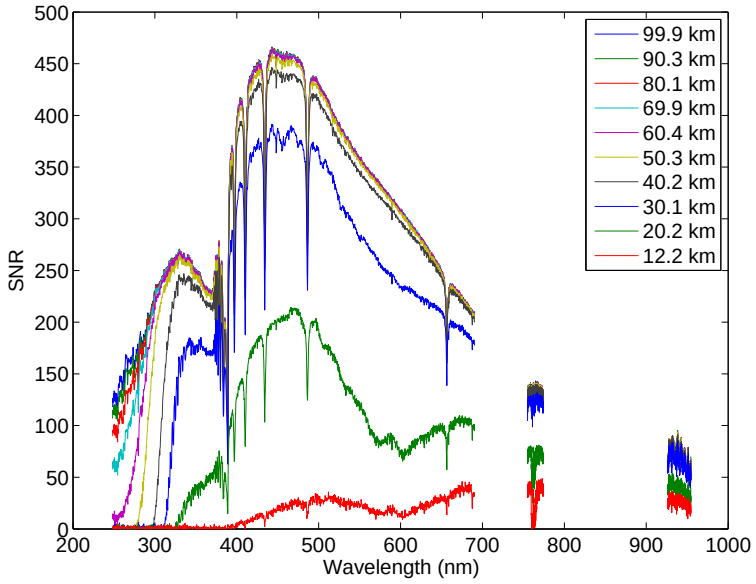

Figure 4.6: Level 2 transmission signal-to-noise ratio. The occultation is the same as in Fig. 3.10. Figure is from ref. [19].

Equation 4.12 is the starting point in the Level 2 inversion. From this formula we can see that there is still not a very simple connection between the measured transmissions and the constituent profiles in the atmosphere. First, the spectral and temporal integrations cause some averaging in the corresponding directions. Second, all the temperature dependent cross sections cause coupling between the spectral and the vertical directions in the problem. These two issues must be addressed.

In the following we show how the model transmission is developed so that it can be used effectively in the data inversion (see Ref. [31]).

4.4.1 Effective cross section method

The temperature dependent cross sections cause coupling between the spectral and the spatial dimensions of the problem. According to our strategy we aim at factorising the problem into spectral and vertical inversion problems as far as possible. This can be achieved by using the effective cross section method. We write:

$$\begin{aligned}\tau(\lambda,\ell) &= \sum_j \int \rho_j(s)\sigma_j(\lambda,\mathrm{T}(s))ds \\ &= \sum_j \sigma_j^{eff}(\lambda,\ell)N_j \end{aligned} \tag{4.13}$$

where N_j is the line density of the species j:

$$N_j = \int_\ell \rho_j(z(s))\, ds \tag{4.14}$$

and:

$$\sigma_j^{\text{eff}}(\lambda, \ell) = \frac{\int_\ell \sigma_j(\lambda, \mathrm{T}(s))\rho_j(s)\, ds}{N_j} \tag{4.15}$$

is the effective cross-section of species j. The use of the effective cross-section has formally separated the inversion problem into two parts. The spectral inversion part is given by Eq. 4.13 with the line densities N_j as unknowns. The vertical inversion part is given by Eq. 4.14 with $\rho_j(z)$ as the unknowns. The two parts are, however, coupled together by the unknown effective cross sections. An iterative loop over spectral and vertical inversion is needed to take this into account. Initially we can use the tangent point temperature in Eq. 4.15.

4.4.2 Spectral and temporal integration

The other model simplification aims at eliminating the need for the spectral and temporal integrations in the model function Eq. 4.12. With the perturbation technique we are able to recover the exponential form of the model transmission. The detailed calculations are not shown here (see Ref. [31]) but the final result is:

$$\bar{T}(\lambda, t) = e^{-\hat{\tau}} \tag{4.16}$$

where the modified optical extinction is (h's being the tangent heights):

$$\begin{aligned}\hat{\tau}(\lambda) = &-\sum_j \tilde{\sigma}_j(\lambda)\bar{N}_j - \frac{1}{2}\sum_{ij} B_{ij}(\lambda)\bar{N}_i\bar{N}_j \\ &+(h(\lambda) - h(\lambda_{ref}))\sum_j \tilde{\sigma}_j(\lambda)\frac{d\bar{N}_j}{dh} \\ &-\frac{(\Delta h)^2}{24}(\sum_j \tilde{\sigma}_j(\lambda)\frac{d\bar{N}_j}{dh})^2\end{aligned} \tag{4.17}$$

where Δh is the vertical coverage of the measurement at the tangent point. The convoluted cross sections are defined by:

$$\tilde{\sigma}_j(\lambda) = \int W(\lambda' - \lambda)\sigma_j(\lambda')d\lambda' \tag{4.18}$$

and the coefficients B_{ij} are coming from the convolution of cross-section correlations:

$$B_{ij}(\lambda) = \int W(\lambda' - \lambda)\sigma_i(\lambda')\sigma_j(\lambda')d\lambda' - \sigma_i(\lambda)\sigma_j(\lambda) \tag{4.19}$$

Note that the cross sections here are effective cross sections.

The unknown instantaneous line densities are now replaced by the averaged line densities:

$$\bar{N_j} = \frac{1}{\Delta t} \int N_j(t) dt \tag{4.20}$$

The derivatives of the line densities are calculated during the iteration loop only.

The transmission model 4.16-4.17 includes the chromatic refraction effect, the spectral convolution by the instrument and the time integration effect. Obviously all effects are taken into account in an approximate way only.

4.5 Spectral inversion

4.5.1 Cross sections

The final ingredient in the model calculation are the cross sections. The cross-sections are taken from the GOMOS cross-section database where they are ordered through species, temperature, and wavelength. The cross sections are obtained from laboratory measurements. There are no cross sections measured directly by the GOMOS instrument.

The scattering cross-sections can also be approached analytically (for absorbing species the cross-sections are too complex to be derived from first principles). The Rayleigh cross-section needed for scattering by air has the following form:

$$\sigma_R(\lambda) = 1.06 \frac{32\pi^3}{3} \frac{(n(\lambda) - 1)^2}{\lambda^4 N_{stp}^2} \tag{4.21}$$

The factor 1.06 is the depolarisation factor for air. The index of refraction $n(\lambda)$ follows the Edlen's law. N_{stp} is the air number density at sea level.

The specification of the aerosol scattering cross section is very difficult. The aerosol content varies all the time in the atmosphere and so varies the effective aerosol cross section. In the retrieval we can either fix a certain best guess cross section or we can try to define a flexible aerosol cross section (actually aerosol extinction) with unknown model parameters. In the latter case the retrieval will hopefully fix the unknown parameters. Both these approaches have been used in the GOMOS Level 2 processing. As a fixed cross section we have used the Angström's formula:

$$\sigma_a(\lambda) = \frac{\sigma_0}{\lambda^b} \tag{4.22}$$

A more flexible description of the aerosol extinction is a simple polynomial expression:

$$\tau(\lambda) = \int_{LOS} \beta(z(s), \lambda) ds = c_0 + c_1 \Delta\lambda + ... \tag{4.23}$$

where the coefficients c_i are unknowns to be determined and $\Delta\lambda = \lambda - \lambda_{ref}$. The order of the polynomial depends on the aerosol state of the atmosphere. In case of high volcanic activity (e.g. the post-Pinatubo period 1991-1993), a broad maximum of $\beta(\lambda)$ can be observed in the visible range and therefore requires at least a quadratic form for a correct description. During background conditions,

the spectral dependence of the aerosol extinction coefficient exhibits mostly a monotonic decrease versus wavelength.

On the other side, the polynomial order should be kept as low as possible due to the non-orthogonality of the aerosol optical thickness dependence with respect to other constituents having a cross section (like Rayleigh scattering by air). Fortunately, ozone is not strongly coupled with aerosol due to its strong spectral signature.

In summary, it is important to point out that the aerosol spectral dependence is a product of GOMOS spectral inversion (and not input data as cross sections are). A higher decoupling of species correlated with aerosol could be achieved by taking into account information coming from spectrometer B, photometers or by inclusion of a priori information. This is the subject of ongoing investigation.

4.5.2 UVIS spectral inversion

In the spectral inversion the observed transmission function is fitted by the model transmission Eq. 4.16 where the line densities are the unknowns. The GOMOS spectral inversion is based on the method that is spectrally global, uses absolute cross sections, takes a non-linear approach and assumes no explicit a priori information (see Ref. [11, 31]).

The estimation of column densities is based on the standard likelihood method (for a more complete but also computationally more expensive method, see Ref. [14]). We aim to minimise the so-called cost function between the data and the model. We assume that the noise in data is nearly Gaussian (see Ref. [11]) and therefore the suitable objective function is the quadratic form:

$$S(N) = (T_{ext}(N) - T_{ext}^{obs})^T C^{-1} (T_{ext}(N) - T_{ext}^{obs}) \tag{4.24}$$

The matrix (in spectral direction and for N) notation is implied. The observed transmission is given by Eq. 4.8 or Eqs. 4.9-4.11. The matrix C is the covariance matrix of the transmission data.

The minimisation is done by using the Levenberg-Marquardt algorithm (see Ref. [34]). This algorithm tries to find a minimum starting from a pre-set initial values. The algorithm also produces an estimate for the covariance matrix assuming that the linearisation of the model function near the minimum is accurate enough. The input covariance for the spectral inversion comes from two sources. The first, the most important one, is the data covariance. If there has been no data operations destroying stochastic independence of data, this covariance is diagonal i.e., it is the variance vector of the data. The second source is the modelling errors. If the data error and the model error are Gaussian we can simply add these two error sources:

$$C = C_{obs} + C_{mod} \tag{4.25}$$

The main source of GOMOS modelling errors in the stratosphere (at altitudes 20–50 km) is the incomplete scintillation correction. We briefly describe the parametrisation of the scintillation correction error (for more details, see

[35]). In the parametrisation, the scintillation correction error is assumed to be a Gaussian random variable with zero mean and covariance matrix C^{mod}:

$$C_{ij}^{mod} = \sigma_i \sigma_j B_{ij} \tag{4.26}$$

Here indices i and j denote the spectrometer pixels corresponding to wavelengths λ_i and λ_j, σ is the amplitude and B is the correlation function of off-diagonal elements. The correlation function is approximated by

$$B_{ij} = B_0(\xi) = e^{-0.4|\xi|^{1.15}} J_0(1.5\xi) \tag{4.27}$$

Here J_0 is the Bessel function of zero order and ξ is the ratio of the chromatic separation of rays corresponding to wavelengths i and j, to the diffractive Fresnel scale

$$rho_F = (\sqrt{\lambda_i \lambda_j}/2\pi)^{1/2} \tag{4.28}$$

$$\xi = \Delta_{ch}(\lambda_i, \lambda_j) \sin\alpha / \rho_F \tag{4.29}$$

α is obliquity of an occultation. $\Delta(\lambda_i, \lambda_j) and$ is the vertical chromatic shift of rays corresponding to wavelengths λ_i and λ_j [36]. For an illustration of these parameters, see Fig. 4 in [37]. An example of the correlation function of the spectrometer pixels at 30 km is shown in Fig. 7 of [37].

The amplitude of the scintillation correction error can be approximated as:

$$\sigma(z, \lambda, \alpha) = T_{ext} \sigma_{iso}(z, \lambda, \alpha) \sqrt{1 - b_{ph} B(\lambda, \lambda_{red})} \tag{4.30}$$

where σ_{iso} is rms of isotropic scintillations (relative fluctuations of intensity) in spectrometer channels, and the term inside the square root takes into account the influence of scintillation correction procedure. σ_{iso} is parameterized as:

$$\sigma_{iso} = \sigma_0(z) \frac{\rho(z)}{\rho_0(z)} \sqrt{\frac{\nu_0}{\nu(\alpha)}} (\frac{\lambda}{\lambda_{red}})^{-1/3} \tag{4.31}$$

Here $\sigma_0(z)$ is the standard profile of isotropic scintillation variance in the spectrometer channels, which was estimated using red photometer data (λ =672 nm) from all occultations of Canopus in 2003 with obliquity about 50 by the method explained in [38],. ρ_0 is the average air density profile in the considered data set. The other factors give the dependence of σ_{iso} on wavelength, obliquity (via dependence of ray velocity v in the phase screen [36]) and the mean air density ρ_0. b_{ph} is the ratio of isotropic scintillation variances of smoothed red photometer and spectrometer signals for λ_{red}=672 nm and it is parametrised as:

$$b_{ph} = e^{-0.105(\frac{\Delta \sin\alpha}{\rho_F})^{1.5}} \tag{4.32}$$

where Δ is the vertical chromatic shift 672 25 nm, corresponding to the width of the red photometer optical filter. $B(\lambda, \lambda_{red})$ is the correlation coefficient

between the smoothed signal of the red photometer and spectrometer channels, which is defined in the same way as the correlation of spectrometer channels. The altitude and wavelength dependence of the amplitude of the scintillation correction error is illustrated in Fig. 8 of [37].

The proposed parametrisation adjusts automatically the correlation and the mean amplitude of isotropic scintillations in spectrometer channels to the different measurement conditions (obliquity, altitude). FCM algorithm is disabled during the initialisation phase. FCM algorithm is also enabled and following modifications must be activated only when the tangent point altitude is lower or equal to 60 km.

The retrieval process described above has been modified during the GOMOS mission in response to difficulties in the neutral density retrieval and to larger than expected effects from scintillations. The retrieval of neutral density often leads to a large bias with respect to the values from ECMWF. Therefore, it has been decided to fix the neutral density to the value given by ECMWF. Between about 20 and 40 km, chromatic scintillations caused by isotropic turbulence, create perturbations in GOMOS transmission spectra that induce unrealistic oscillations in the vertical profiles of line densities of some species, mainly NO_2 and NO_3. The scintillation correction step (Eq. (4.7)) is unable to remove these scintillations from the transmission data. In order to improve the retrieval, a variant named GDI (Global DOAS Iterative) of the DOAS retrieval is applied for NO_2 and NO_3.

In the GDI a species is artificially separated into two virtual species X_S and X_D with their respective cross-sections:

$$\sigma_S(\lambda) + \sigma_D(\lambda) = \sigma(\lambda) \tag{4.33}$$

The spectral inversion is performed in two phases. The first Levenberg-Marquardt fit is applied with X_S=X_0 and X_D as a free parameter together with all other species that we want to retrieve. The fit gives a first value $X_D^{(1)}$. The second fit is applied with X_S=$X_D^{(1)}$. A second value $X_D^{(2)}$ is obtained. The process is iterated until the maximum number of iterations is performed or until a given convergence criterion is reached.

4.5.3 IR spectrometer spectral inversion

The IR spectrometer measures the densities of two different constituents O_2 and H_2O in two bands: 756-773 nm and 926-952 nm respectively. Due to the physics of the problem, the individual absorption lines are very thin and saturated, the apparent cross sections change with the integrated densities, and they can no longer be considered as only wavelength dependent. The calculation of the transmission function is computationally very demanding. Therefore, it is difficult to use the same direct inversion method like for the UVIS spectrometer data.

A new algorithm has been developed. The method uses reference transmission spectra ($T_{mod}(\lambda, N)$) which are calculated for different integrated densities

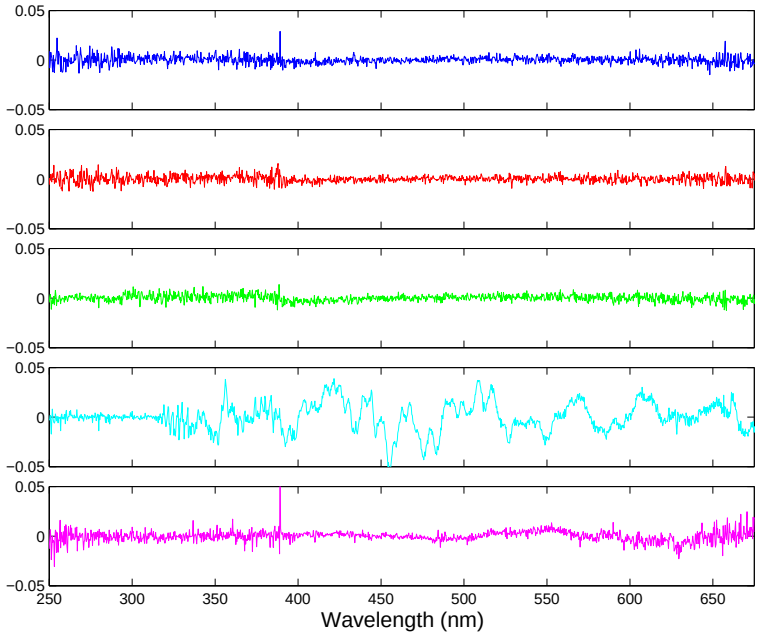

Figure 4.7: Residuals (unit-less) between observed and modelled transmissions at altitudes 12 (bottom panel), 30, 50, 90 and 100 km (top panel). The disturbances from scintillations are evident at 30 km. Figure is from ref. [19].

of O_2 or of H_2O. These reference transmissions slightly depend on pressure. To take into account this dependency, calculations of transmission are performed by using a direct model with a standard atmospheric profile. Several such calculations are done for different atmospheric models in order to get the response for different conditions such as tropical, mid-latitude and subarctic atmospheric profiles. The method fits a function:

$$y = a \log(T_{mod}(\lambda, N)) + \frac{b}{\lambda} + c \tag{4.34}$$

to the data set formed by the observed transmissions. The last two terms in Eq. 4.34 are for the fitting of the background. By varying the model function or by varying the altitude where the model function is calculated we aim to minimise the difference $a - 1$. Due to its nature, this method has been called "comparative method ". An illustrative example is shown in Fig. 4.8.

4.6 Vertical inversion

The vertical inversion problem aims to find the vertical profile $\rho(z)$ that fulfils:

$$N(z_t) = \int \rho(z(s))ds \tag{4.35}$$

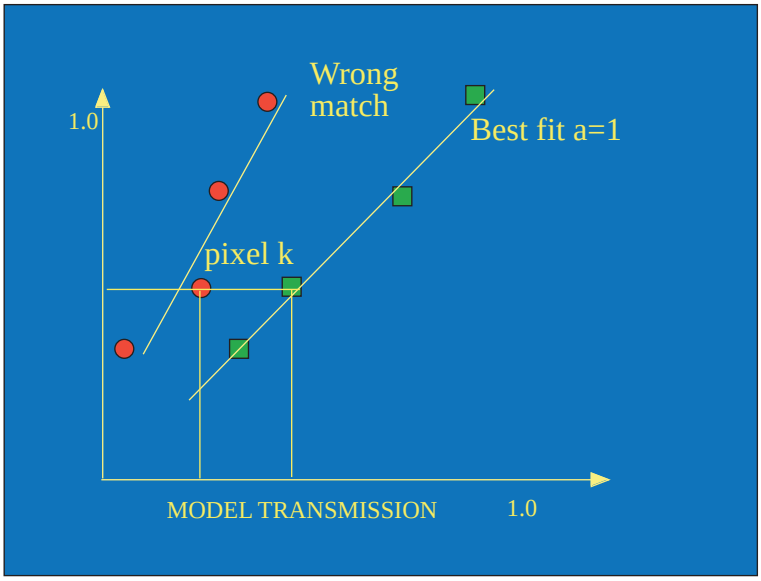

Figure 4.8: IR fitting.

where N is any of the line densities inverted in the spectral inversion.

The normal approach to the under-determined inversion problem Eq. 4.35 is to make it even-determined by discretising the atmosphere into layers. The number of layers is given by the number of measurements in the occultation processed. The resulting problem is a readily solvable linear inversion problem. By the triangular nature of the kernel matrix the inversion can be done using the so-called onion peeling method.

The vertical inversion method used in the GOMOS data processing makes an attempt to create continuous profiles instead of the layer structure of the onion peeling technique. We approximate the local densities to be linear as a function of altitude between two successive GOMOS measurements:

$$\rho(z) = \frac{(z_{j-1} - z)\rho(z_j) + (z - z_j)\rho_{j-1}}{z_{j-1} - z_j} \tag{4.36}$$

Other approaches have been discussed in Ref. [31]. After a tedious algebra the problem 4.35-4.36 is transformed to a matrix equation:

$$A\rho = N \tag{4.37}$$

where A is a relatively complicated kernel matrix.

As already mentioned the line density values we are using as inputs are the result of an integration in time and then should be adapted to the "instantaneous" expression that has been derived (i.e. the linear system is only valid for instantaneous line densities). To pass from integrated to instantaneous data we

use an expression derived from Taylor expansion:

$$\bar{N}_j = N_j + \frac{(\Delta t)^2}{24}\frac{\partial^2 N_j}{\partial t^2} \tag{4.38}$$

Then if we summarise these contributions into a matrix form, the vertical inversion consists of solving the following linear system:

$$\bar{N} = K\rho \tag{4.39}$$

This matrix equation can be solved by standard methods. The covariance matrix is produced.

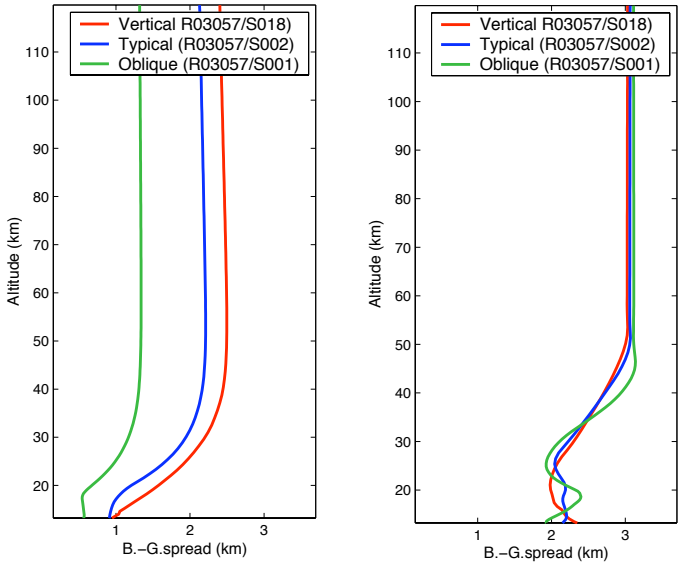

Figure 4.9: The vertical resolution.

In the case of GOMOS, the inversion above produces vertical profiles with unphysical oscillations. Therefore the inversion is performed using the Tikhonov regularisation method (Ref. [39]). The classical Tikhonov regularised solution of the problem is a minimiser of the functional:

$$F(\lambda) = \|\mathbf{K}\rho - \mathbf{N}\|^2 + \lambda\|\mathbf{H}\rho\|^2 \tag{4.40}$$

Here λ is the regularisation parameter and the tri-diagonal matrix $\mathbf{H}$ approximates second differences.

We apply the so-called grid-independent target resolution form of the Tikhonov

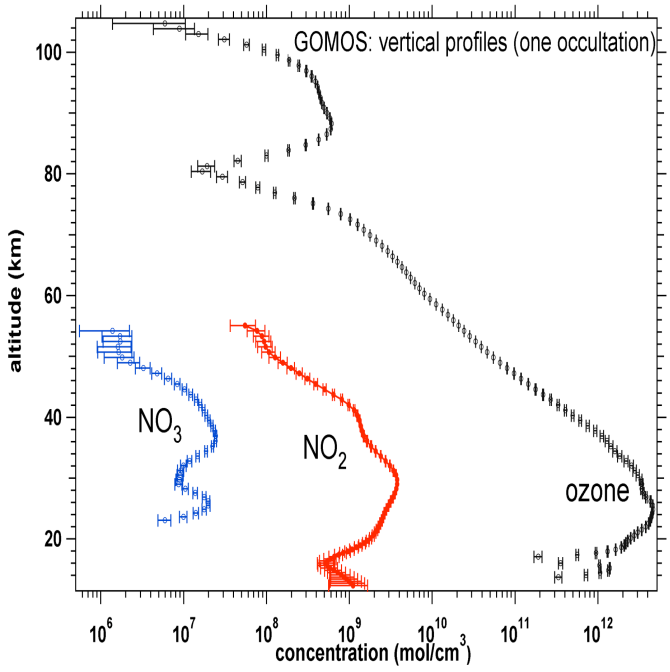

Figure 4.10: The vertical profiles and their errors in one occultation.

regularisation (Ref.[39]). Then:

$$\mathbf{H} = \mathrm{diag}\left[\frac{1}{h_i^2}\right]\begin{bmatrix} 0 & 0 & 0 & ... & 0 \\ 1 & -2 & 1 & ... & 0 \\ ... & .. & ... & ... & ... \\ 0 & ... & 1 & -2 & 1 \\ 0 & 0 & ... & 0 & 0 \end{bmatrix} \tag{4.41}$$

The Tikhonov regularized solution of (4.40) exists, and it is unique. It is given by the formula:

$$\hat{\rho} = (\mathbf{K}^T\mathbf{K} + \lambda\mathbf{H}^T\mathbf{H})^{-1}\mathbf{K}^T\mathbf{N} \tag{4.42}$$

Fig. 4.9 shows the sampling resolution and the regularized resolution for various viewing angles (with respect to the orbital plane). Fig. 4.10 shows an example of retrieved profiles. GOMOS vertical density product includes also five covariance values for each altitude.

4.7 Level 2 loops

With the vertical inversion we have produced density profiles. Originally the plan was to use temperature profile from the MSIS90 model and ECMWF data

and then after vertical inversion to calculate a new GOMOS temperature profile from Rayleigh scattering or from O_2 data of the IR-spectrometer. The current version keeps the ECMWF/MSIS90 data because the Rayleigh and O_2 retrievals have not been good enough for this purpose.

The new ozone data and the ECMWF/MSIS90 temperature profile are injected to the calculation of the effective cross-sections and the spectral and vertical inversion are carried out again. It has been shown that this iterative process over spectral and vertical inversions significantly improves the final results. Therefore it is routinely applied (at least once and at the maximum twice) to reach best results.

4.8 High resolution temperature profile

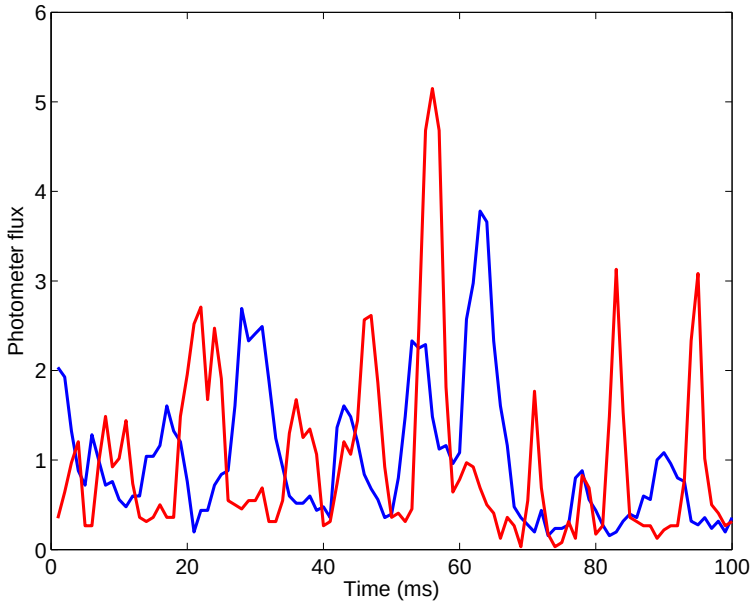

Figure 4.11: Blue and red photometer signals. Both signals have been normalised by dividing by the mean. In the horizontal axis time is the occultation time measured from the altitude of 26 km (35 s since the beginning of the occultation). The obliquity of the occultation is 3.9. Some peaks show clearly the time delay effect between the red and blue photometers. Figure is from ref. [19].

Besides the scintillation correction, the photometers signals can be used to detect small scale structures in the atmosphere. Specifically we can derive high resolution temperature profiles.

The algorithm to derive the high resolution temperature profile is based on

the computation of the time delay between the signals of the two photometers. Due to the variation of the index of refraction of air with wavelength, the light beam of an occulted star is more bent in the blue part of the spectrum than in the red part. For a given tangent altitude, the red beam reaches GOMOS before the blue beam (see Fig. 2.8). The computation of the time delay gives information on the bending angle which is related to the density and temperature profile in the atmosphere. This method allows us to derive an high resolution temperature profile with a vertical resolution of 100-200 m.

The algorithm is divided in three main parts:

1. Computation of the chromatic time delay between the two photometers
2. Determination of the refraction angle
3. Determination of the atmospheric profile.

The time delay is computed at 40 Hz, corresponding to a vertical sampling of 85 m at most. This means that 20 time delay values are computed during each 0.5 s spectrometer measurement.

The time delay is computed by searching the time shift between the blue and the red signal which gives the largest correlation coefficient between the two signals taken in a time window corresponding to a vertical change of the tangent altitude of 250 m.

The difference in the refractive angle between the central wavelengths of the blue and the red photometers is obtained from the time delay Δt (not to be confused with the integration time 0.5 sec):

$$\delta_{blue} - \delta_{red} = \frac{v_z \Delta t}{L} \tag{4.43}$$

where L is the distance between GOMOS and the limb and v_z the projection of the satellite velocity on the vertical axis at tangent point.

The refractive angle is directly proportional to the refractivity $\nu - 1$ and is obtained with a linear transformation:

$$\delta_{blue} = \frac{(\delta_{blue} - \delta_{red})\nu_{blue}}{(\nu_{blue} - \nu_{red})} = \frac{\delta_{blue} - \delta_{red}}{(\frac{\Delta\nu}{\nu})} \tag{4.44}$$

The coefficient $\Delta\nu/\nu$=0.011 depends on the exact band pass of the photometers.x

Once the refraction angle as a function of the impact parameter is obtained (at 40 Hz), the profile of refractivity, directly proportional to the atmospheric density, is obtained by inverting an Abel integral:

$$n(h_{blue}) = \frac{1}{\pi} \int_{h_{blue}}^{\infty} \frac{\delta_{blue}(h)}{\sqrt{(R+h)^2 - (R+h_{blue})^2}} dh \tag{4.45}$$

where h_{blue} is the impact parameter and R the Earth radius.

The inversion is done downwards, starting at the top of the high resolution profile (around 35-40 km) and using the model atmospheric profile at the tangent point above this altitude. Once the density profile is obtained, the temperature profile is computed using the hydrostatic equation. An example of the retrieved temperature profile is provided in Fig. 4.12.

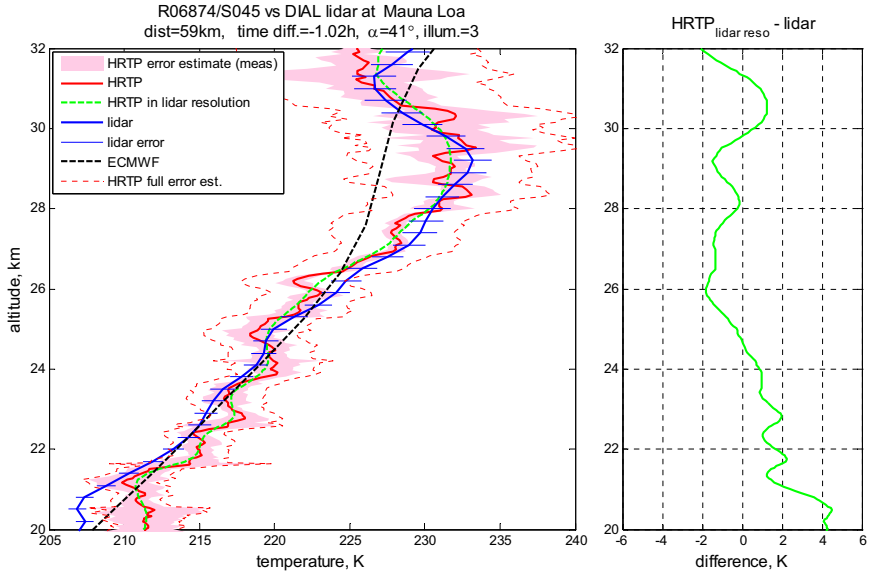

Figure 4.12: GOMOS HRTP compared with the ECMWF temperature profile and with a temperature profile from a lidar. The uncertainty (in pink) shows the contribution from random errors (coloured area) and the total error including initialisation bias (dashed).

4.9 Level 2 products

The level 2 processing chain is shown in Fig. 4.13 and products in Table 4.1.

Some part of the Level 2 products are delivered to various Meteo Offices and other users, as Fast Delivery Products (available within 3 hours of ground reception). The GOMOS processing is identical to the standard processing. The main difference is that the external atmospheric data are predictions, while the standard processing is based on an a posteriori analysis.

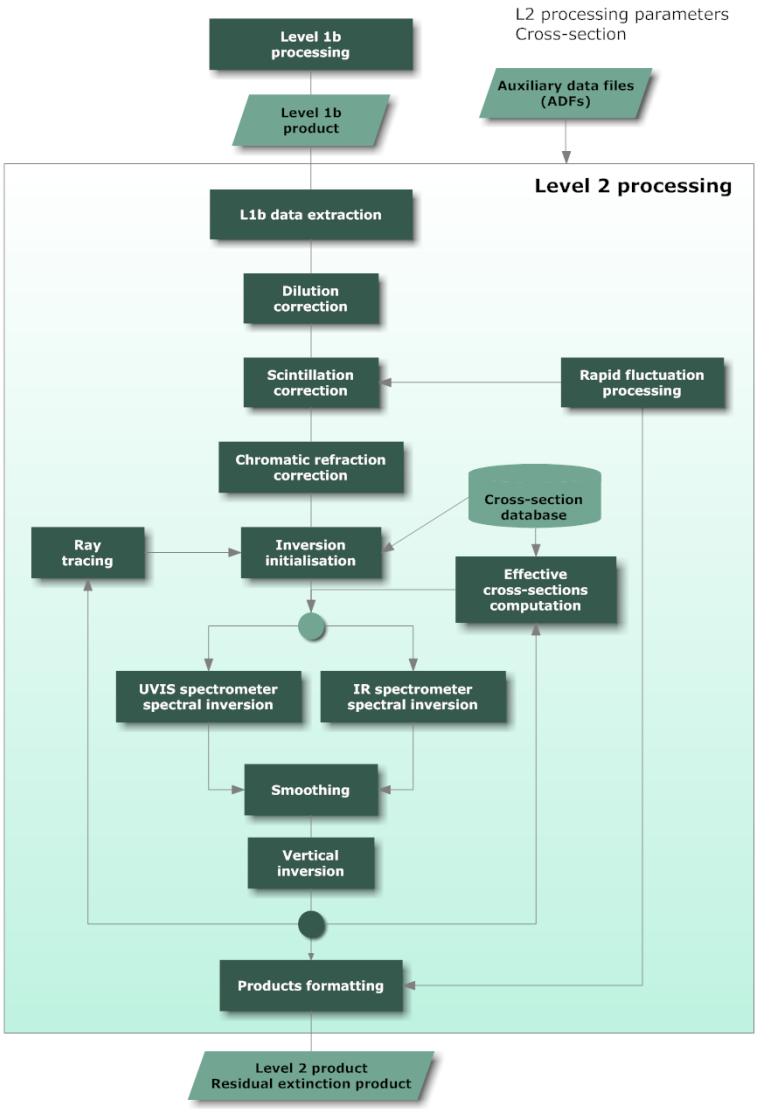

Figure 4.13: GOMOS Level 2 processing architecture.

Table 4.1: **GOMOS Level 2 products**

Product	**Description**
Local density product	Once per occultation
Line Density	The line density of O_3, NO_2, NO_3, O_2, H_2O and air, which come as a result of the spectral inversion process. The relative errors and the flag tables for densities. Errors are 1σ errors (standard deviation) expressed in %. The spectral inversion covariance matrix for each altitude.
Local Density	The local density of O_3, NO_2, NO_3, O_2, H_2O and air, which come as a result of the vertical inversion process. The relative errors and the flag tables for densities. The full vertical covariance matrix is not included but only five nearest elements.
Aerosol	Tangential extinction and error at the reference wavelength (500 nm). Local extinction (km-1) and error at the reference wavelength (500 nm). Spectral parameters of the extinction coefficient and error estimates
High resolution temperature	From the analysis of fast photometers, the vertical profiles of temperature and density and corresponding errors are retrieved at high resolution (40 Hz). They are derived from the time delay between the peaks of red and blue fast photometers.
Geolocation	Position of the spacecraft and error. Position of the tangent point of LOS and error. Tangent point pressure and temperature (from external model)
Accuracy	Chi-2 final value. Covariance matrix for line densities after spectral inversion. Covariance matrix for local densities after vertical inversion. The 12 x 12 covariance matrix (symmetrical) is given, corresponding to the 6 gas species, 5 aerosol parameters and one spare. For the vertical inversion the covariance matrix is also given (influence of one altitude on the other).
Residual extinction product	Once per occultation
Residual transmission	Transmission corrected for scintillation and dilution effects.
Transmission model function	The retrieval of line densities is based on fitting the transmission function to the refraction corrected transmission data, The model function in this product is the final value of the model after nonlinear iteration.

Chapter 5

GOMOS data quality

5.1 Level 1b

GOMOS geophysical retrieval is based on horizontal transmission data, limb radiance data and photometer data. The retrieval from the transmission data leads to horizontal column densities and local density of O_3, NO_2, NO_3, O_2, H_2O. Ozone and aerosols can also be retrieved from limb radiances but this is not part of the official ESA GOMOS processing [30]. Photometer data leads to HRTP.

GOMOS Level 1b and Level 2 transmission data are unique and therefore their quality cannot be investigated by a normal validation technique using ground based instruments. The only direct comparison presently is with the SAGE II solar occultation measurements at five SAGE II wavelengths but the diurnal variation of the atmosphere and sun/star differences in refraction effects make this comparison difficult (Kyrölä et al., 2012, unpublished). Another possibility would be a comparison to data from the UVISI instrument on board the MSX-satellite. UVISI has carried out successfully stellar occultations during 1996-2001 providing samples of ozone profiles in the stratosphere [40]. This comparison of transmissions has not yet been performed.

Without real validations or satellite-satellite intercomparisons we need to investigate transmission data quality by what we know about measurement physics and about what we will assume in the Level 2 retrieval. Theoretically transmission values should be between zero and one but inherent noise fluctuations and also scintillation fluctuations can break these limits. Solar scattered light and atmospheric emissions also contribute to transmission in such a way that transmission values can be negative or exceed one. In full dark measurements the solar contamination can be ignored but atmospheric emissions remain. These emissions are not modeled in Level 2 data handling chain and therefore, the spectral regions having emissions at general noise level or more need to be removed from retrieval. This has been done for O emissions at 630 nm. The auroral emissions have been found in GOMOS data but their effect on retrieval

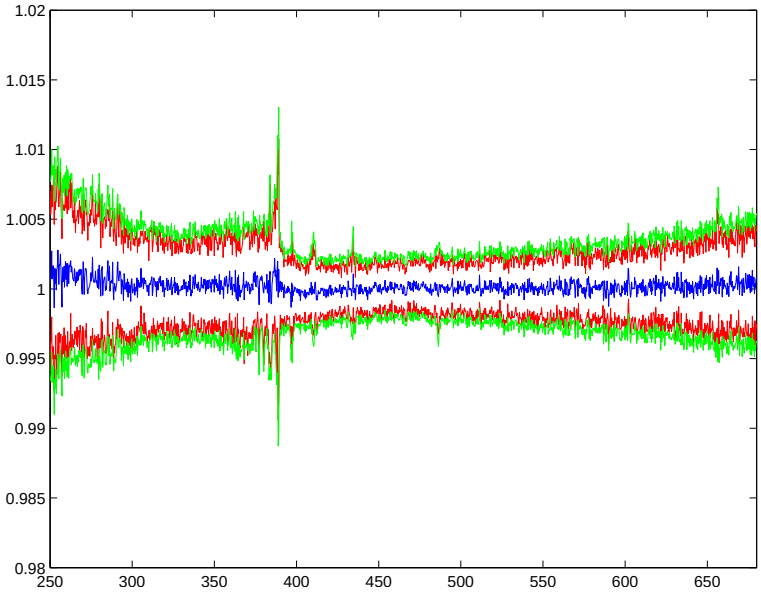

Figure 5.1: GOMOS measurements of Sirius spectra at Equator in 2003. The blue line is the mean of transmissions at 130 km, red lines are std values and green are mean of error estimates.

quality has been estimated to be negligible.

In other illumination conditions than full dark the quality of transmission depends critically from the removal of background light from the central detection band of the CCD. This removal is known to be in error in measurements of noctilucent clouds where the small vertical extent of the scattering cloud is in contradiction with the assumptions of the background removal algorithm. Generally, in bright limb cases we have good reasons to suspect that the background removal does not work accurately enough. The retrieved daytime profiles are of poor quality.

Even if the retrieval from the limb product is not included in this document we can learn something relevant from limb-related studies. Limb radiances have been compared to the ones measured by OSIRIS on Odin and strong stray light contribution has been identified [30]. This is not a fundamental problem for the background removal algorithm but it has also been found that upper and lower background band measurements are not consistent with each other. This may contribute to the poor results in daytime occultations. Limb measurements have also shown large deviations from OSIRIS in the UV-part of the spectrum.

The last element in the quality of transmission is noise. Usually, the data retrieval and error estimation in Level 2 work best if the data distribution (at given wavelength) is normally distributed, The statistical distribution of noise can be studied to some extent by investigating measurements from a single star.

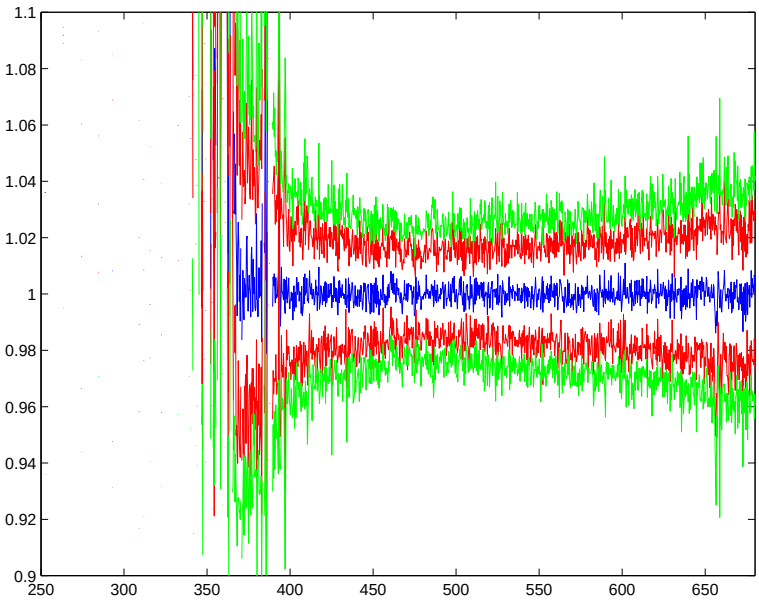

Figure 5.2: GOMOS measurements of Iot1Sco (star 178 in GOMOS star catalogue) spectra at Equator in 2003. The blue line is the mean of transmissions at 130 km, red lines are std values and green are mean of error estimates.

In Figs. 5.1 and 5.2 we show the mean transmission at 130 km from a bright and weak star. The transmission are near unity as they should be. The error estimates slightly overestimate the actual fluctuations. Studies on earlier version of GOMOS data (Kyrölä et al, GOM-FMI-TN-023, unpublished) have further shown that the distribution of noise is close to the normal distribution.

5.2 Level 2

In Level 2 the vertical profiles of trace gas columns and local densities are retrieved from reduced transmissions (refraction corrected). The reduced transmissions can be studied in the same way as Level 1 transmission but more interesting is to study the spectral residuals after the spectral inversion. In Fig. 5.3 we show an example of star 29 (GOMOS star catalogue) residual at 30 km. The overestimation of errors is similar to Level 1b. In addition, a small fine structure can be found in 350-400 nm.

The overall performance of the spectral inversion can be investigated from χ^2 values. For normally distributed noise and for linear problem χ^2 values should be near one. Figures 5.4 and 5.5 show χ^2 values for several star classes and two years, 2003 and 2010. At higher altitudes we see that values are near one, even slightly below. This is an indication of a small overestimation of noise. This is in line with our earlier observations of the transmission noise. Below 50

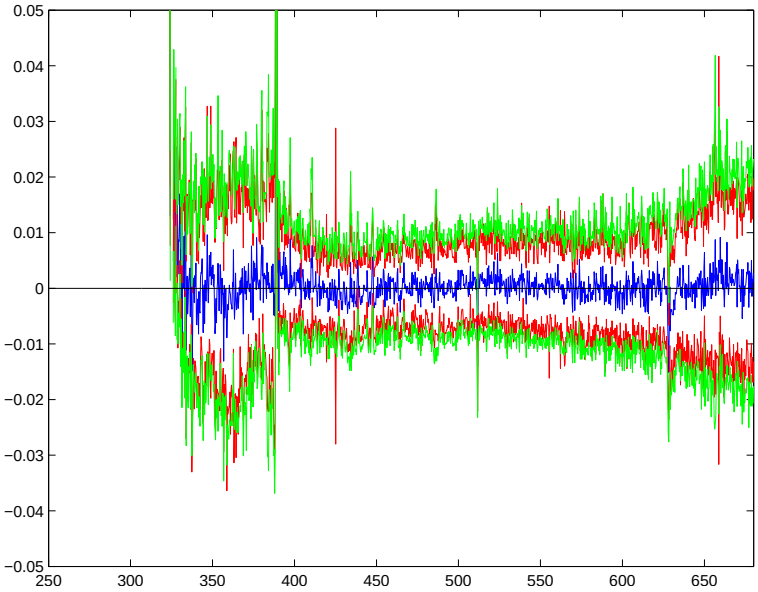

Figure 5.3: Spectral inversion residual of (star 29 in theGOMOS star catalogue) at Equator in 2003. The blue line is the mean of residual at 130 km, red lines are std values and green are mean of error estimates.

km values increase and obtain their maximum values in the troposphere. Some degradation of χ^2 values between 2003-2010 can be seen.

The investigation of the quality of column densities from the spectral inversion is similarly difficult as with the horizontal transmissions. The vertical local density profiles can, however, be inspected with classical validation methods. We have also quite a good understanding how the profiles should look like in general. The special feature of the GOMOS method is that the uncertainty for a given retrieved gas varies from one occultation to another. We first look how the error estimates depend on the star qualities.

Ozone retrieval at high altitudes is based solely on UV-wavelengths and cool stars radiate only little at these wavelengths. By comparing statistical averages of ozone from different stars (with solar zenith angle larger than 105°) we have found that there are 58 stars[1] that do not support ozone retrievals above 40-50 km. Note that the judgement is somewhat subjective and the quality of retrievals has changed during the mission. The ozone retrievals from these stars show negative bias at lower altitudes (the reason for this is presently under investigation). The "bad" and "good" stars on the star temperature-magnitude

[1]During the period 2002-2004 42 bad stars were identified with GOMOS star catalogue numbers: 3, 13, 14, 17, 26, 37, 43, 48, 50, 51, 52, 53, 54, 61, 63, 65, 75, 84, 92, 93, 94, 102, 106, 114, 116, 117, 120, 126, 137, 138, 139, 141, 148, 151, 161, 162, 165, 167, 169, 170, 171, 178; in 2005-2008 11 new stars: 16, 40, 101, 113, 132, 135, 142, 143, 154, 155, 157; in 2009-2012 5 new stars: 122, 134, 159, 164, 173.

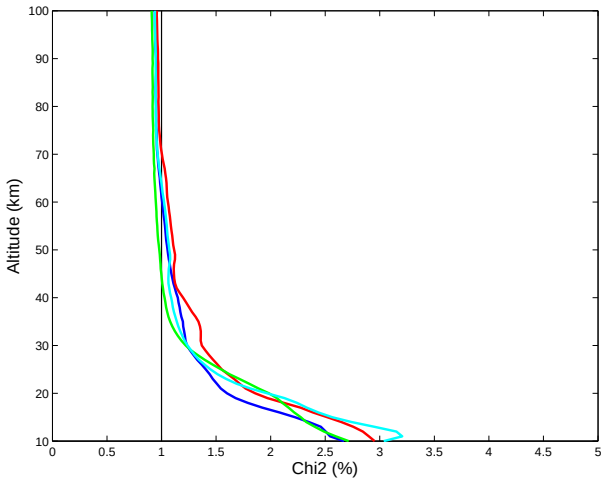

Figure 5.4: GOMOS χ^2 values in 2003. Color coding as follows: red:T>7000K, mag<1.9; blue: T<7000K, mag<0.9; green: T<7000, mag>1.9; cyan T>7000K, m>1.9.

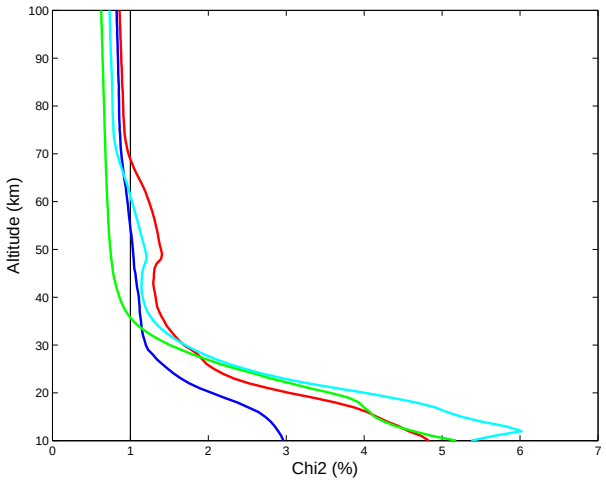

Figure 5.5: GOMOS χ^2 values in 2010. Color coding as follows: red:T>7000K, mag<1.9; blue: T<7000K, mag<0.9; green: T<7000, mag>1.9; cyan T>7000K, m>1.9.

plane is shown in Fig. 5.6.

For other gases the retrieval accuracy is limited by the visual magnitude of the star. In addition to temperature and magnitude of the star occultation illumination conditions determine the quality of the results. In bright limb occultations the accuracies are strongly degraded because of increased noise.

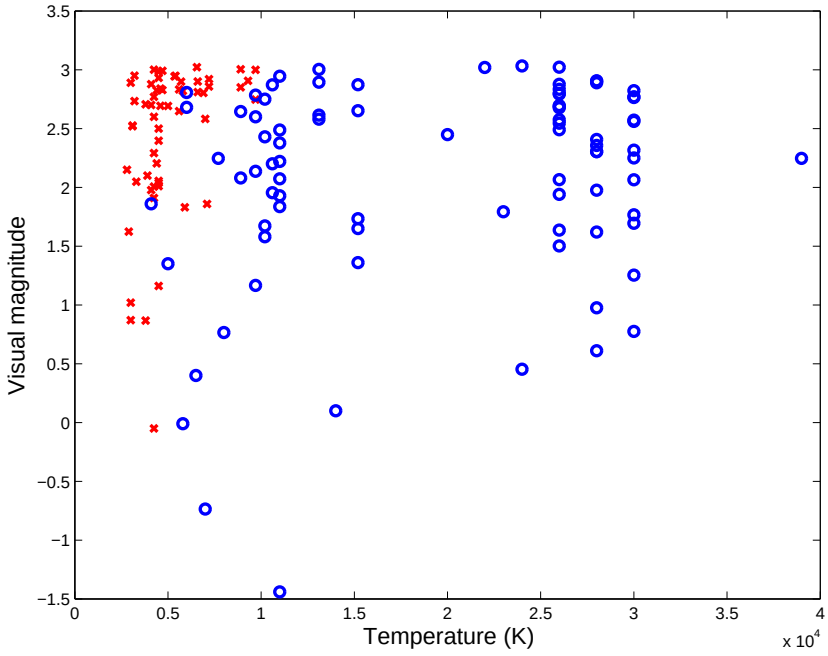

Figure 5.6: GOMOS stars on the star temperature-magnitude plane. The good stars (84) at the end of the mission are shown by blue circles and the bad stars (58) by red crosses.

Obliqueness of the occultation has no noticeable effect on retrieval accuracy. The movement of the tangent point in oblique occultations needs to remembered, however.

Figures 5.7-5.8 show error estimate for several star classes. As expected the star temperature has a strong effect on the capability to measure ozone profiles. For stars with T<7000, mag>1.9 ozone retrieval is possible only below 40-50 km. For other gases the retrieval accuracy is dictated by the visual magnitude.

From Figs. 5.7-5.8 it is easy to see how the increased noise of CCDs has increased the estimated errors. The instrument response has also changed during its ten years of operation. An idealistic view of an occultation measurement claims that measurements are stable in time. This is based on the cancellation of multiplicative calibration parameters when calculating atmospheric transmission from spectral measurements. But we have seen that in the case of GOMOS we need first to remove a considerable amount of dark charge and in bright limb and twilight cases also background radiation. It is probable that the uncertainties in these removals overshadow to some extent the benefit from the cancellation of calibration parameters. This means that the long-term stability of GOMOS results depends very much on the quality of the dark charge estimation. At the moment we have no sound evidence that GOMOS

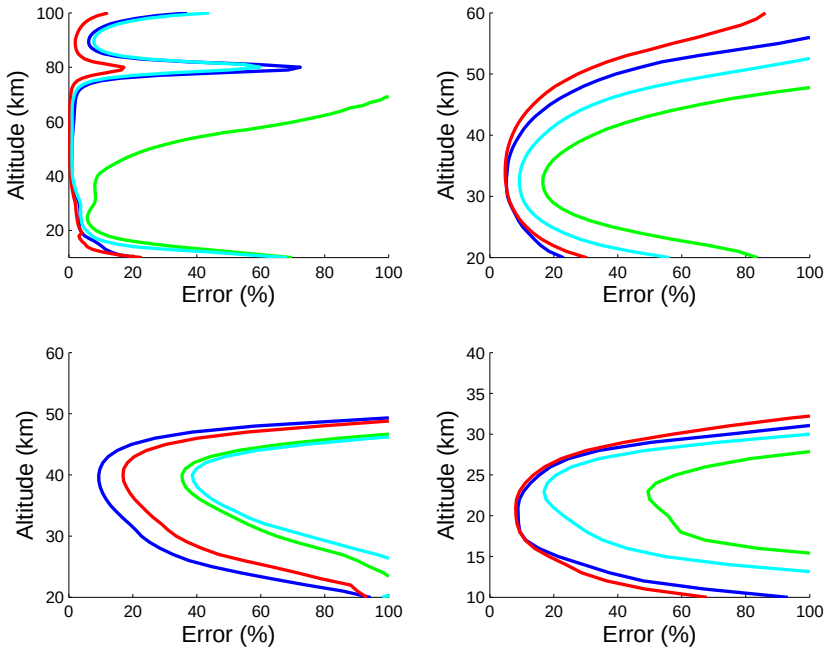

Figure 5.7: GOMOS error estimates 2003 in clockwise order O_3 (upper left), NO_2, NO_3 and aerosols. Aerosol results are from IPF 5. Color coding as follows: red:T>7000K, mag<1.9; blue: T<7000K, mag<0.9; green: T<7000, mag>1.9; cyan T>7000K, m>1.9.

results have been drifting due to instrument aging (for estimates, see presentations in `http://congrexprojects.com/atmos2012/programme`) and in `https://www1.cmos.ca/abstracts/abstracts128/congress_schedule.asp`).

The real test of GOMOS Level 2 products is obtained from geophysical validation. GOMOS data validation activity has been carried out since the summer of 2002. Results have been reported in ACVE-conferences by ESA and in scientific publications. The comprehensive validation of ozone against ground-based and balloon-borne instruments has been presented in [41]. The results show that in dark limb the GOMOS data agree very well with the correlative data: between 14 and 64 km altitude their differences show only a small (2.5 –7.5%) insignificant negative bias with a standard deviation of 11 –16% (19 –63 km). This conclusion was demonstrated to be independent of the star temperature and magnitude and the latitudinal region of the GOMOS observation, with the exception of a slightly larger bias in the polar regions at altitudes between 35 and 45 km. Updates of this work has been issued in [42].

GOMOS, MIPAS and SCIAMACHY measurements have been compared in [43]. In the mesosphere and lower thermosphere only satellite data are available for validation purposes. GOMOS results have been compared with MIPAS

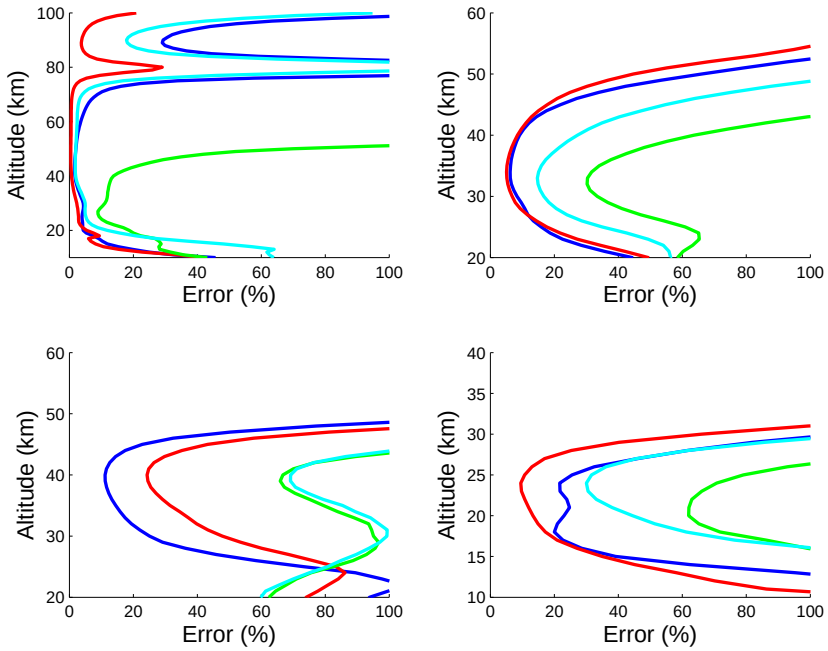

Figure 5.8: GOMOS error estimates 2010 in clockwise order O_3 (upper left), NO_2, NO_3 and aerosols. Aerosol results are from IPF 5.Color coding as follows: red:T>7000K, mag<1.9; blue: T<7000K, mag<0.9; green: T<7000, mag>1.9; cyan T>7000K, m>1.9.

[44]. A general agreement between these two instruments has been found but presently too few coincident measurements are available for a definitive comparison. GOMOS NO_2 measurements have been compared with HALOE in [45], with MIPAS in [46] and with ACE-FTS in [47]. For NO_3 we have validation with a balloon borne instrument in [48]. SAGE III lunar measurements of NO_3 have been compared with GOMOS in [49] and they show good agreement. Recent GOMOS validation results can be found from the Atmospheric science conference 2012 program (see `http://congrexprojects.com/atmos2012/programme`) and from the Quadrennial Ozone Symposium program (see `https://www1.cmos.ca/abstracts/abstracts128/congress_schedule.asp`).

The GOMOS Level 1b and Level 2 data processing contain quite an extensive collection of processing modules that presumably take all the major physical effects into account. The modelling errors have been introduced in Table 5.1 and table of quantitative estimates is presented in Table 5.2 (for more details, see [20]). The GOMOS Level 2 disclaimer (see `http://envisat.esa.int/handbooks/availability/disclaimers/`) provides detailed information on the quality of GOMOS products.

Table 5.1: **Modelling errors**

Error source	**Symptom or Impact**
Excluded constituents in the spectral retrieval	Only two constituents, OClO and Na, have so far been retrieved from GOMOS data an addition to the constituents discussed before. These retrievals call special statistical averaging of several occultations and the impact of these gases in single retrievals can be ignored.
Background subtraction	The quality of bright limb occultations decrease quickly below 35 km. It is possible that the model used to calculate the bright limb contribution in the central band does not work properly.
Incomplete correction of scintillations	Isotropic scintillations are not completely removed by the scintillation correction algorithm. This leads to most 2% errors for O_3 line densities.
Incomplete removal of refractive dilution	The estimated transmission error is at most 1%
Errors in geolocation	The maximal errors in tangent height are estimated to be 170 m at 10 km and 100 m above 40 km. The ensuing ozone errors are less than 0.5% above 20 km. At lower altitudes, the error increases to 4% at 10 km.
Error in the assumed temperature distribution	The error in temperature affects the temperature dependent cross sections.
Errors in the used cross sections	The cross sections from different laboratory measurements may differ considerably from each other. This leads naturally to different values in retrievals.
Errors in aerosol modelling	The aerosol extinction model is a second order polynomial of wavelength where the expansion coefficients are determined from data by the spectral inversion. The model's flexibility may lead to a situation where the aerosol part includes some other slowly varying (in wavelength) atmospheric or instrumental phenomena.
Retrieval errors in the spectral inversion	In very low S/N conditions the LM procedure in the spectral inversion may settle down to a wrong local minimum. This is a possible source for some biased retrievals.

Table 5.2: **Estimates of GOMOS errors**

Data characteristics	**O_3**	**NO_2**	**NO_3**	**Aerosol**
Altitude range	15–100 km	20–50 km (65 km in solar events) km	25–50 km	10–40 km
Resolution	2-3 km	4 km	4 km	4 km
Random errors: Measurement noise and scintillations	10% around 15 km; 0.5–4 % in stratosphere; 2–10 % in mesosphere	10–20 %	20–40 %	30% around 10 km; 2–10% in 15–25 km; 10–50% in 24-40 km
	slightly increasing with time			
Systematic errors: Aerosol model selection	∼20 % below 20 km; 1–5 % in 20–25 km; <1% above 25 km	∼10% in 15-20 km; 0–5 % in 20–25 km; negligible elsewhere	negligible above 25 km	<10% below 35 km; 10–50 % in 35–40 km
Temperature uncertainty	< 0.5% in 30–60 km; negligible elsewhere	negligible	negligible	
Uncertainty in cross sections	∼1%	few per-cents	few per-cents	Connected to the aerosol model uncertainty
Uncertainty in neutral a priori density	< 1% below 20 km; negligible elsewhere	negligible	negligible	< 5% below 22 km; 5-15% in 22–40 km

Chapter 6

Discussion

In this document we have discussed the ESA GOMOS Level 0/1b and Level 2 processing algorithms and retrieved products. GOMOS measurements have provided global vertical distributions of ozone [50, 51], NO_2 and NO_3[45, 51], and aerosols [52, 53, 54]. In addition to normal products several additional products have been issued. Turbulence parameters [55] and noctilucent cloud occurrence [56] from photometers, and OClO [57] and sodium [58, 59] from spectrometers by a special processing.

GOMOS retrieval algorithms have been investigated in several publications: [33, 60, 61, 62, 63, 39, 64, 65, 66, 19, 20, 26]. The processing itself has undergone many changes since the launch. The most important ones are (for a complete list, see the monthly GOMOS report `http://envisat.esa.int/handbooks/availability/disclaimers/`.

- Calibration of the dark charge for each orbit in order to counteract the sensitivity of the GOMOS CCD to particle precipitation. An automatic correction for dark charge residual bias from detector temperature uncertainty.
- Full covariance matrix implemented in the spectral inversion
- DOAS-type inversion for NO_2 and NO_3 to counteract perturbations from isotropic scintillations
- Tikhonov constraints in the vertical inversion to smooth oscillations
- Neutral density is not retrieved but set equal to the value predicted by ECMWF. The retrievals suffered from bias and interfered with aerosol retrieval.
- GOMOS atmospheric products (GAP) are not produced.

The development of GOMOS algorithms continues. Several improvements or alternatives are under investigation:

- SPB2 iPRNU correction for H_2O retrieval
- H_2O retrieval algorithm
- Retrieval from GOMOS limb products (see [29], and [30])
- Correction for straylight
- Inclusion of the ECMWF neutral density as a priori data in the Level 2 inversion
- One-step inversion (spectral and vertical inversions combined)
- Aerosol model development
- Validation of error estimates

The novelty and richness of GOMOS measurements will certainly foster many new studies for algorithms and data usage in future.

Acknowledgements

The GOMOS Level 2 processing scheme is a product of many years and many people. At FMI the following people has participated in the development: E. Kyrölä, G. W. Leppelmeier, L. Oikarinen (deceased in 2002), E. Sihvola (now at the University of Helsinki), J. Tamminen, V. Sofieva; At LATMOS-IPSL: P.Benet, J. L. Bertaux, E. Chassefière, F. Dalaudier, A. Hauchecorne, J-C. Lebrun,M. Martic, B. Théodor; at IASB: D. Fussen, F. Vanhellemont, P. Simon. M. Van Roozendael; at ACRI: A. Mangin, O. Fanton d'Andon, G. Barrot, M. Guirlet, L. Blanot; at ESA: J. Langen, G. Levrini, A. Popescu, F. Spiero. T. Wehr, T. Fehr, A. Dehn, L. Saavedra de Miguel. In particular, the team wishes to thank Odile Fanton d'Andon for her enthusiasm, encouragement, and leadership, all of which were essential to obtaining a coherent result from such a diverse group.

Bibliography

[1] S. Solomon. Stratospheric ozone depletion: a review of concepts and history. *Rev. Geophys.*, 37(3):275–316, 1999.

[2] J. L. Bertaux, G. Megie, T. Widemann, E. Chassefiere, R. Pellinen, E. Kyrölä, S. Korpela, and P. Simon. Monitoring of ozone trend by stellar occultations: The GOMOS instrument. *Adv. Space Res.*, 11(3):237–242, 1991.

[3] J. L. Bertaux, E. Kyrölä, and T. Wehr. Stellar occultation technique for atmospheric ozone monitoring: GOMOS on Envisat. *Earth Observation Quarterly*, 67:17–20, 2000.

[4] J. L. Bertaux, A. Hauchecorne, F. Dalaudier, C. Cot, E. Kyrölä, D. Fussen, J. Tamminen, G. W. Leppelmeier, V. Sofieva, S. Hassinen, O. Fanton d'Andon, G. Barrot, A. Mangin, B. Théodore, M. Guirlet, O. Korablev, P. Snoeij, R. Koopman, and R. Fraisse. First results on GOMOS/Envisat. *Adv. Space Res.*, 33:1029–1035, 2004.

[5] E. Kyrölä, J. Tamminen, G. W. Leppelmeier, V. Sofieva, S. Hassinen, J.-L. Bertaux, A. Hauchecorne, F. Dalaudier, C. Cot, O. Korablev, O. Fanton d'Andon, G. Barrot, A. Mangin, B. Theodore, M. Guirlet, F. Etanchaud, P. Snoeij, R. Koopman, L. Saavedra, R. Fraisse, D. Fussen, and F. Vanhellemont. GOMOS on Envisat: An overview. *Adv. Space Res.*, 33:1020–1028, 2004.

[6] J. L. Bertaux, E. Kyrölä, D. Fussen, A. Hauchecorne, F. Dalaudier, V. Sofieva, J. Tamminen, F. Vanhellemont, O. Fanton D'Andon, G. Barrot, A. Mangin, L. Blanot, J. C. Lebrun, K. Pérot, T. Fehr, L. Saavedra, G. W. Leppelmeier, and R. Fraisse. Global ozone monitoring by occultation of stars: an overview of GOMOS measurements on ENVISAT. *Atmospheric Chemistry & Physics*, 10:12091–12148, December 2010.

[7] ESA. *Envisat-GOMOS, An instrument for global atmospheric ozone monitoring*, volume SP-1244. European Space Agency, 2001.

[8] J. L. Elliot. Stellar occultation studies of the solar system. *Ann. Rev. Astron. Astrophys.*, 17:445–475, 1979.

[9] R. G. Hays and P. B. Roble. Stellar spectra and atmospheric composition. *J. Atmos. Sci.*, 25:1141–1153, 1968.

[10] S. Korpela. *A study of the operational principles of the GOMOS instrument for global ozone monitoring by the occultation of stars.* Geophysical publications, no. 22. Finnish Meteorological Institute, Helsinki, 1991. Ph.D thesis at the Helsinki University of Technology.

[11] E. Kyrölä, E. Sihvola, Y. Kotivuori, M. Tikka, T. Tuomi, and H. Haario. Inverse theory for occultation measurements, 1, Spectral inversion. *J. Geophys. Res.*, 98:7367–7381, 1993.

[12] G. E. Smith and D. M. Hunten. Study of planetary atmospheres by absorptive occultations. *Rev. Geophys.*, 28:117–143, 1990.

[13] E. Kyrölä. GOMOS ATBD—Level 2. In *ESAMS99, European Symposium on Atmospheric Measurements From Space*, volume WPP-161, pages 125–137, Noordwijk, 1999. ESA.

[14] J. Tamminen, E. Kyrölä, and H. Auvinen. MCMC algorithms for inverse problems in remote sensing. In *ESAMS99, European Symposium on Atmospheric Measurements from Space*, volume WPP-161. ESA, 1999.

[15] J. L. Bertaux. GOMOS mission objectives. In *ESAMS99, European Symposium on Atmospheric Measurements From Space*, volume WPP-161, pages 79–87, Noordwijk, 1999. ESA.

[16] E. Kyrölä and J. Tamminen. GOMOS mission planning. In *ESAMS99, European Symposium on Atmospheric Measurements from Space*, volume WPP-161, pages 101–110, Noordwijk, 1999. ESA.

[17] J. Louet. Envisat ground segment structure. In *ESAMS99, European Symposium on Atmospheric Measurements from Space*, volume WPP-161, pages 17–23. ESA, 1999.

[18] J. L. Bertaux. GOMOS ATBD—Level 1b. In *ESAMS99, European Symposium on Atmospheric Measurements From Space*, volume WPP-161, pages 115–123, Noordwijk, 1999. ESA.

[19] E. Kyrölä, J. Tamminen, V. Sofieva, J. L. Bertaux, A. Hauchecorne, F. Dalaudier, D. Fussen, F. Vanhellemont, O. Fanton D'Andon, G. Barrot, M. Guirlet, A. Mangin, L. Blanot, T. Fehr, L. Saavedra de Miguel, and R. Fraisse. Retrieval of atmospheric parameters from GOMOS data. *Atmospheric Chemistry & Physics*, 10:11881–11903, December 2010.

[20] J. Tamminen, E. Kyrölä, V. F. Sofieva, M. Laine, J.-L. Bertaux, A. Hauchecorne, F. Dalaudier, D. Fussen, F. Vanhellemont, O. Fanton-D'Andon, G. Barrot, A. Mangin, M. Guirlet, L. Blanot, T. Fehr, L. Saavedra de Miguel, and R. Fraisse. GOMOS data characterisation and error estimation. *Atmospheric Chemistry & Physics*, 10:9505–9519, October 2010.

[21] A. Popescu and T. Paulsen. Gomos data products. In *ESAMS99, European Symposium on Atmospheric Measurements from Space*, volume WPP-161, pages 111–114. ESA, 1999.

[22] L. Oikarinen. Monte Carlo simulations of radiative transfer for limb scan measurements. In *ESAMS99, European Symposium on Atmospheric Measurements from Space*, volume WPP-161, pages 243–249. ESA, 1999.

[23] L. Oikarinen, E. Sihvola, and E. Kyrölä. Multiple scattering radiance in limb-viewing geometry. *J. Geophys. Res.*, 104(D24):31,261–31,274, 1999.

[24] A. Popescu and T. Paulsen. Gomos instrument on Envisat. In *ESAMS99, European Symposium on Atmospheric Measurements from Space*, volume WPP-161, pages 89–99. ESA, 1999.

[25] B. Edlen. The refractive index of air. *Metrologia*, 2(71), 1966.

[26] P. Keckhut, A. Hauchecorne, L. Blanot, K. Hocke, S. Godin-Beekmann, J.-L. Bertaux, G. Barrot, E. Kyrölä, J. A. E. van Gijsel, and A. Pazmino. Mid-latitude ozone monitoring with the GOMOS-ENVISAT experiment version 5: the noise issue. *Atmospheric Chemistry & Physics*, 10:11839–11849, December 2010.

[27] J. Tamminen, E. Kyrölä, L. Oikarinen, E. Sihvola, and H. Haario. Tomographic inversion of GOMOS measurements. In A. Steen, editor, *Proceedings of the 19th Annual European Meeting on Atmospheric Studies by Optical Methods*, pages 17–22. IRF, 1992.

[28] H. Auvinen, L. Oikarinen, E. Kyrölä, J. Tamminen, and G. W. Leppelmeier. Inversion algorithms for OSIRIS and GOMOS bright-limb background term. In *ESAMS99, European Symposium on Atmospheric Measurements from Space*, volume WPP-161, pages 271–276, 1999.

[29] G. Taha, G. Jaross, D. Fussen, F. Vanhellemont, E. Kyrölä, and R. D. McPeters. Ozone profile retrieval from GOMOS limb scattering measurements. *Journal of Geophysical Research (Atmospheres)*, 113(D12):23307–+, December 2008.

[30] S. Tukiainen, E. Kyrölä, P. T. Verronen, D. Fussen, L. Blanot, G. Barrot, A. Hauchecorne, and N. Lloyd. Retrieval of ozone profiles from GOMOS limb scattered measurements. *Atmospheric Measurement Techniques Discussions*, 3:4355–4382, October 2010.

[31] E. Sihvola. *Coupling of spectral and vertical inversion in the analysis of stellar occultation data.* Geophysical publications, no. 38. Finnish Meteorological Institute, Helsinki, 1994. Licentiate thesis at the University of Helsinki, Department of Theoretical Physics.

[32] F. Vanhellemont, D. Fussen, and C. Bingen. Global one-step inversion of satellite occultation measurements: A practical method. *Journal of Geophysical Research (Atmospheres)*, 109(D18):9306, 2004.

[33] V. Sofieva. *Inverse problems in stellar occultation.* Finnish Meteorological Institute contributions, no. 49. Finnish Meteorological Institute, Helsinki, 2005. Doctoral thesis at the Helsinki University of Technology, Department of Engineering Physics and Mathematics .

[34] W. H. Press, S. A. Teukolsky, W. T. Vetterling, and B. P. Flannery. *Numerical Recipes in FORTRAN, The Art of Scientific Computing.* Clarendon Press, Oxford, 1992.

[35] V. F. Sofieva, J. Vira, E. Kyrölä, J. Tamminen, V. Kan, F. Dalaudier, A. Hauchecorne, J.-L. Bertaux, D. Fussen, F. Vanhellemont, G. Barrot, and O. Fanton D'Andon. Retrievals from GOMOS stellar occultation measurements using characterization of modeling errors. *Atmospheric Measurement Techniques*, 3(4):1019–1027, 2010.

[36] F. Dalaudier, V. Kan, and A. S. Gurvich. Chromatic refraction with global ozone monitoring by occultation of stars. I. Description and scintillation correction. *Applied Optics*, 40(6):866–877, February 2001.

[37] V. F. Sofieva, V. Kan, F. Dalaudier, E. Kyrölä, J. Tamminen, J.-L. Bertaux, A. Hauchecorne, D. Fussen, and F. Vanhellemont. Influence of scintillation on quality of ozone monitoring by GOMOS. *Atmos. Chem. Phys.*, 9:9197–9207, December 2009.

[38] V. F. Sofieva, A. S. Gurvich, F. Dalaudier, and V. Kan. Reconstruction of internal gravity wave and turbulence parameters in the stratosphere using GOMOS scintillation measurements. *Journal of Geophysical Research (Atmospheres)*, 112(D11):12113, June 2007.

[39] V. F. Sofieva, J. Tamminen, H. Haario, E. Kyrölä, and M. Lehtinen. Ozone profile smoothness as a priori information in the inversion of limb measurements. *Annales Geophysicae*, 22(10):3411–3420, 2004.

[40] J.-H. Yee, R. J. Vervack Jr., R. Demajistre, F. Morgan, J. F. Carbary, G. J. Romick, D. Morrison, S. A. Lloyd, P. L. DeCola, L. J. Paxton, D. E. Anderson, C. K. Kumar, and C.-I Meng. Atmospheric remote sensing using a combined extinctive and refractive stellar occultation technique, 1. overview and proof-of-concept observations. *J. Geophys. Res.*, 107(D14):10 1029, 2002. 10.1029/2001JD000794.

[41] Y. J. Meijer, D. P. J. Swart, M. Allaart, S. B. Andersen, G. Bodeker, Boyd, G. Braathena, Y. Calisesia, H. Claude, V. Dorokhov, P. von der Gathen, M. Gil, S. Godin-Beekmann, F. Goutail, G. Hansen, A. Karpetchko, P. Keckhut, H. M. Kelder, R. Koelemeijer, B. Kois, R. M. Koopman, J.-C. Lambert, T. Leblanc, I. S. McDermid, S. Pal, G. Kopp, H. Schets,

R. Stubi, T. Suortti, G. Visconti, , and M. Yela. Pole-to-pole validation of ENVISAT/GOMOS ozone profiles using data from ground-based and balloon-sonde measurements. *J. Geophys. Res.*, 109(D23):art. no D23305, 2004.

[42] J. A. E. van Gijsel, D. P. J. Swart, J.-L. Baray, H. Bencherif, H. Claude, T. Fehr, S. Godin-Beekmann, G. H. Hansen, P. Keckhut, T. Leblanc, I. S. McDermid, Y. J. Meijer, H. Nakane, E. J. Quel, K. Stebel, W. Steinbrecht, K. B. Strawbridge, B. I. Tatarov, and E. A. Wolfram. GOMOS ozone profile validation using ground-based and balloon sonde measurements. *Atmospheric Chemistry & Physics Discussions*, 10:8515–8551, 2010.

[43] A. Bracher, H. Bovensmann, K. Bramstedt, J. P. Burrows, T. V. Clarmann, K.-U. Eichmann, H. Fischer, B. Funke, S. Gil-López, N. Glatthor, U. Grabowski, M. Höpfner, M. Kaufmann, S. Kellmann, M. Kiefer, M. E. Koukouli, A. Linden, M. López-Puertas, G. M. Tsidu, M. Milz, S. Noel, G. Rohen, A. Rozanov, V. V. Rozanov, C. V. Savigny, M. Sinnhuber, J. Skupin, T. Steck, G. P. Stiller, D.-Y. Wang, M. Weber, and M. W. Wuttke. Cross comparisons of O_3 and NO_2 measured by the atmospheric ENVISAT instruments GOMOS, MIPAS, and SCIAMACHY. *Advances in Space Research*, 36:855–867, 2005.

[44] P. T. Verronen, E. Kyrölä, J. Tamminen, B. Funke, S. Gil-López, M. Kaufmann, M. López-Puertas, T. von Clarmann, G. Stiller, U. Grabowski, and M. Höpfner. A comparison of night-time GOMOS and MIPAS ozone profiles in the stratosphere and mesosphere. *Adv. Space Res.*, 36:958–966, 2005.

[45] A. Hauchecorne, J.-L. Bertaux, F. Dalaudier, C. Cot, J.-C. Lebrun, S. Bekki, M. Marchand, E. Kyrölä, J. Tamminen, V. Sofieva, D. Fussen, F. Vanhellemont, O. Fanton d'Andon, G. Barrot, A. Mangin, B. Théodore, M. Guirlet, P. Snoeij, R. Koopman, L. Saavedra de Miguel, R. Fraisse, and J.-B. Renard. First simultaneous global measurements of nighttime stratospheric NO_2 and NO_3 observed by Global Ozone Monitoring by Occultation of Stars (GOMOS)/Envisat in 2003. *J. Geophys. Res.*, 110(D18):D18301, September 2005.

[46] P. T. Verronen, S. Ceccherini, U. Cortesi, E. Kyrölä, and J. Tamminen. Statistical comparison of night-time NO_2 observations in 2003–2006 from GOMOS and MIPAS instruments. *Adv. Space Res.*, 43:1918–1925, June 2009.

[47] T. Kerzenmacher, M. A. Wolff, K. Strong, E. Dupuy, K. A. Walker, L. K. Amekudzi, R. L. Batchelor, P. F. Bernath, G. Berthet, T. Blumenstock, C. D. Boone, K. Bramstedt, C. Brogniez, S. Brohede, J. P. Burrows, V. Catoire, J. Dodion, J. R. Drummond, D. G. Dufour, B. Funke, D. Fussen, F. Goutail, D. W. T. Griffith, C. S. Haley, F. Hendrick, M. Höpfner, N. Huret, N. Jones, J. Kar, I. Kramer, E. J. Llewellyn,

M. López-Puertas, G. Manney, C. T. McElroy, C. A. McLinden, S. Melo, S. Mikuteit, D. Murtagh, F. Nichitiu, J. Notholt, C. Nowlan, C. Piccolo, J.-P. Pommereau, C. Randall, P. Raspollini, M. Ridolfi, A. Richter, M. Schneider, O. Schrems, M. Silicani, G. P. Stiller, J. Taylor, C. Tétard, M. Toohey, F. Vanhellemont, T. Warneke, J. M. Zawodny, and J. Zou. Validation of NO_2 and NO from the Atmospheric Chemistry Experiment (ACE). *Atmos. Chem. Phys.*, 8:5801–5841, October 2008.

[48] J.-B. Renard, G. Berthet, C. Brogniez, V. Catoire, D. Fussen, F. Goutail, H. Oelhaf, J.-P. Pommereau, H. K. Roscoe, G. Wetzel, M. Chartier, C. Robert, J.-Y. Balois, C. Verwaerde, F. Auriol, P. François, B. Gaubicher, and P. Wursteisen. Validation of GOMOS-Envisat vertical profiles of O_3, NO_2, NO_3, and aerosol extinction using balloon-borne instruments and analysis of the retrievals. *Journal of Geophysical Research (Space Physics)*, 113(A12):A02302, February 2008.

[49] J. Hakkarainen, J. Tamminen, J. R. Moore, and E. Kyrölä. Direct comparisons of GOMOS and SAGE III NO_3 vertical profiles. *Atmospheric Measurement Techniques Discussions*, 5:1497–1514, February 2012.

[50] E. Kyrölä, J. Tamminen, G. W. Leppelmeier, V. Sofieva, S. Hassinen, A. Seppälä, P. T. Verronen, J.-L. Bertaux, A. Hauchecorne, F. Dalaudier, D. Fussen, F. Vanhellemont, O. Fanton d'Andon, G. Barrot, A. Mangin, B. Theodore, M. Guirlet, R Koopman, L. Saavedra, P. Snoeij, and T. Fehr. Nighttime ozone profiles in the stratosphere and mesosphere by the Global Ozone Monitoring by Occultation of Stars on Envisat. *J. Geophys. Res.*, 111:D24306, 2006.

[51] E. Kyrölä, J. Tamminen, V. Sofieva, J. L. Bertaux, A. Hauchecorne, F. Dalaudier, D. Fussen, F. Vanhellemont, O. Fanton D'Andon, G. Barrot, M. Guirlet, T. Fehr, and L. Saavedra de Miguel. GOMOS O_3, NO_2, and NO_3 observations in 2002-2008. *Atmospheric Chemistry and Physics*, 10(16):7723–7738, 2010.

[52] F. Vanhellemont, D. Fussen, C. Bingen, E. Kyrölä, J. Tamminen, V. Sofieva, S. Hassinen, J. L. Bertaux, A. Hauchecorne, F. Dalaudier, O. Fanton D'Andon, G. Barrot, A. Mangin, B. Théodore, M. Guirlet, J. B. Renard, R. Fraisse, P. Snoeij, R. Koopman, and L. Saavedra. A first comparison of GOMOS aerosol extinction retrievals with other measurements. *Advances in Space Research*, 36:894–898, 2005.

[53] F. Vanhellemont, D. Fussen, C. Bingen, E. Kyrölä, J. Tamminen, V. Sofieva, S. Hassinen, P. Verronen, A. Seppälä, J. L. Bertaux, A. Hauchecorne, F. Dalaudier, O. Fanton D'Andon, G. Barrot, A. Mangin, B. Théodore, M. Guirlet, J. B. Renard, R. Fraisse, P. Snoeij, R. Koopman, and L. Saavedra. A 2003 stratospheric aerosol extinction and PSC climatology from GOMOS measurements on Envisat. *Atmos. Chem. Phys.*, 5:2413–2417, 2005.

[54] F. Vanhellemont, D. Fussen, N. Mateshvili, C. Tétard, C. Bingen, E. Dekemper, N. Loodts, E. Kyrölä, V. Sofieva, J. Tamminen, A. Hauchecorne, J.-L. Bertaux, F. Dalaudier, L. Blanot, O. Fanton D'Andon, G. Barrot, M. Guirlet, T. Fehr, and L. Saavedra. Optical extinction by upper tropospheric/stratospheric aerosols and clouds: GOMOS observations for the period 2002-2008. *Atmospheric Chemistry & Physics*, 10:7997–8009, August 2010.

[55] V. F. Sofieva, E. Kyrölä, S. Hassinen, L. Backman, J. Tamminen, A. Seppälä, L. Thölix, A. S. Gurvich, V. Kan, F. Dalaudier, A. Hauchecorne, J.-L. Bertaux, D. Fussen, F. Vanhellemont, O. Fanton d'Andon, G. Barrot, A. Mangin, M. Guirlet, T. Fehr, P. Snoeij, L. Saavedra, R. Koopman, and R. Fraisse. Global analysis of scintillation variance: Indication of gravity wave breaking in the polar winter upper stratosphere. *Geophys. Res. Lett.*, 34:3812, February 2007.

[56] K. Pérot, A. Hauchecorne, F. Montmessin, J.-L. Bertaux, L. Blanot, F. Dalaudier, D. Fussen, and E. Kyrölä. First climatology of polar mesospheric clouds from GOMOS/ENVISAT stellar occultation instrument. *Atmospheric Chemistry & Physics*, 10:2723–2735, March 2010.

[57] D. Fussen, F. Vanhellemont, J. Dodion, C. Bingen, N. Mateshvili, F. Daerden, D. Fonteyn, Q. Errera, S. Chabrillat, E. Kyrölä, J. Tamminen, V. Sofieva, A. Hauchecorne, F. Dalaudier, J.L. Bertaux, J.-B. Renard, R. Fraisse, O. Fanton d'Andon, G. Barrot, M. Guirlet, A. Mangin, B. Théodore, , P. Snoeij, and L. Saavedra. A global OClO stratospheric layer discovered in GOMOS stellar occultation measurements. *Geophys. Res. Lett.*, 33(13):L13815, 2006.

[58] D. Fussen, F. Vanhellemont, C. Bingen, E. Kyrölä, J. Tamminen, V. Sofieva, S. Hassinen, A. Seppälä, P. Verronen, J.-L. Bertaux, A. Hauchecorne, F. Dalaudier, J.-B. Renard, R. Fraisse, O. Fanton d'Andon, G. Barrot, A. Mangin, B. Théodore, M. Guirlet, R. Koopman, P. Snoeij, and L. Saavedra. Global measurement of the mesospheric sodium layer by the star occultation instrument GOMOS. *Geophys. Res. Lett.*, 31(24):L24110, Dec 2004.

[59] D. Fussen, F. Vanhellemont, C. Tétard, N. Mateshvili, E. Dekemper, N. Loodts, C. Bingen, E. Kyrölä, J. Tamminen, V. Sofieva, A. Hauchecorne, F. Dalaudier, J.-L. Bertaux, G. Barrot, L. Blanot, O. Fanton D'Andon, T. Fehr, L. Saavedra, T. Yuan, and C.-Y. She. A global climatology of the mesospheric sodium layer from GOMOS data during the 2002-2008 period. *Atmospheric Chemistry & Physics*, 10:9225–9236, October 2010.

[60] J. Tamminen and E. Kyrölä. Bayesian solution for nonlinear and non-Gaussian inverse problems by Markov chain Monte Carlo method. *J. Geophys. Res.*, 106(D13):14377–14390, 2001.

[61] J. Tamminen, E. Kyrölä, and V. Sofieva. Does prior information improve measurements? In G. Kirchengast, U. Foelsche, and A.K. Steiner, editors, *Occultations for Probing Atmosphere and Climate - Science from the OPAC-1 Workshop*, pages 87–98. Springer Verlag, 2004.

[62] V. F. Sofieva, E. Kyrölä, J. Tamminen, and M. Ferraguto. Atmospheric density, pressure and temperature profile reconstruction from refractive angle measurements in stellar occultation. In G. Kirchengast, U. Foelsche, and A.K. Steiner, editors, *Occultations for Probing Atmosphere and Climate - Science from the OPAC-1 Workshop*, pages 289–298. Springer Verlag, 2004.

[63] J. Tamminen. Validation of nonlinear inverse algorithms with Markov chain Monte Carlo method. *J. Geophys. Res.*, 109(D19):D19303, October 2004.

[64] H. Haario, M. Laine, M. Lehtinen, E. Saksman, and J. Tamminen. MCMC methods for high dimensional inversion in remote sensing (with discussion). *J. R. Statist. Soc. B*, 66(Part 3):591–607, 2004.

[65] D. Fussen, F. Vanhellemont, C. Bingen, B. Kyrölä, J. Tamminen, V. Sofieva, S. Hassinen, A. Seppälä, P. T. Verronen, J. L. Bertaux, A. Hauchecorne, F. Dalaudier, O. F. D'Andon, G. Barrot, A. Mangin, B. Theodore, M. Guirlet, J. B. Renard, R. Fraisse, P. Snoeij, R. Koopman, and L. Saavedra. Autoregressive smoothing of GOMOS transmittances. *Advances in Space Research*, 36:899–905, 2005.

[66] J. Tamminen. *Adaptive Markov chain Monte Carlo algorithms with geophysical applications.* Finnish Meteorological Institute contributions, no. 47. Finnish Meteorological Institute, Helsinki, 2004. Doctoral thesis at the University of Helsinki, Department of Mathematics ans Statistics.

Appendix A

Acronyms

ADU Analog-to-Digital Units

CCD Charge Coupled Device

CFC Chlorofluorocarbon

CNRS Centre National de la Recherche Scientifique

DC Dark Charge

DCNU Dark Charge Non Uniformity

DOAS Differential Optical Absorption Spectroscopy

DSA Dark Sky Area

ECMWF European Centre for Medium-term Weather Forecast

ENVISAT ENVIronment SATellite

ESA Earth Space Agency

ESL GOMOS Expert Support Laboratory

FMI Finnish Meteorological Institute

FOV Field Of View

FP Fast Photometer

GDI Global DOAS iterative

GOMOS Global Ozone Monitoring by Occultation of Stars

GOPR GOMOS Prototype (GOMOS gaound segment simulator)

HRTP High-Resolution Temperature Profiles

IASB Institut dAronomie Spatiale de Bruxelles

IODD Input/Output Data Definition

IR Infra-Red

LIMBO FMI's signal simulator and inversion package for limb-measurements

LM Levenberg-Marquardt

LOS Line of Sight

LSF Point Spread Function (Spectral direction)

LUT Look Up Table

MIPAS Michelson Interferometer for Passive Atmospheric Sounding

MSIS90 Mass-Spectrometer-Incoherent-Scatter Model (version 90)

NIR Near Infra-Red

NRT Near Real Time

PRNU Pixel (to pixel) Response Non Uniformity

PSF Point Spread Function (Spatial direction)

SdA Service dAronomie du CNRS (presently LATMOS)

S/C Spacecraft

S/N Signal to Noise

SATU Star Acquisition and Tracking Unit

SCIAMACHY SCanning Imaging Absorption spectroMeter for Atmospheric CartograpHY

SFA Steering Front Assembly

SXXX GOMOS star identification number (ex. S001 is Sirius)

RTS Radio Telegraphic Signal

SZA Solar Zenith Angle

UV Ultra Violet

UVIS Ultra violet - VISible

Appendix B

Additional sources of information

GOMOS data is available free of charge online. For data access please, please see `https://earth.esa.int/web/guest/missions/esa-operational-eo-missions/envisat/instruments/GOMOS`. Additional GOMOS information can be obtained from the following web-sites:

Links to GOMOS specific material: `https://earth.esa.int/web/guest/missions/esa-operational-eo-missions/envisat/instruments/gomos`

GOMOS daily, monthly and other reports: `http://earth.eo.esa.int/pcs/envisat/gomos/reports/`

GOMOS data consolidation: `http://earth.eo.esa.int/pcs/envisat/gomos/consolidated_dataset/Level_0/index.html`

GOMOS data disclaimers etc.: `http://envisat.esa.int/handbooks/availability/disclaimers/`

ESA is supporting a group of institutes and a company to make research on GOMOS data processing issues. This group is called GOMOS Expert Support Laboratories. They are:

Finnish Meteorological Institute (FMI) : Earth observation, P.O. Box 503, FIN-00101; Helsinki, Finland. Erkki Kyrölä: erkki.kyrola@fmi.fi

LATMOS-IPSL : Quartier des Garennes,11, Boulevard d'Alembert, 78280 Guyancourt,FRANCE phone: 33 1 64 47 42 51. Jean-Loup Bertaux:jean-loup.bertaux@aerov.jussieu.fr

IASB (Institut d'Aeronomie Spatiale de Belgique) : 3, Avenue Circulaire, 1180 - BRUXELLES, BELGIQUE phone: 32 2 3730371, fax : 32 2 3748423. Didier Fussen: didier@labora.oma.be

ACRI S.A. : 260 Route du Pin Montard, B.P. 234, Sophia Antipolis Cedex, France phone: 33 (0)4 92 96 75 00, fax : 33 (0)4 93 95 80 98. Odile Fanton d'Andon: oha@acri.fr

The GOMOS Science Advisory (SAG) group consisted of the following members: J. L. Bertaux, F. Dalaudier, A. Hauchecorne, D. Fussen, E. Kyrölä, J. Langen, G. W. Leppelmeier, J.B. Renard, H. K. Roscoe, P. Simon,T. Wehr.

The GOMOS Quality Working Group consists of the following members in 2012: J. L. Bertaux, F. Dalaudier, A. Hauchecorne, D. Fussen, E. Kyrölä, J. Tamminen, V. Sofieva, G. Barrot, O. Fanton d'Andon, L. Blanot, L. Saavedra de Miguel, A. Guijsel and R, Fraisse. A. Dehn from ESA is the chairman of the group.

Appendix C

Cross sections

C.1 O_3

O3 cross section are from Bogumil et al., 2001. Interpolated linearly on a regular spectral grid from 235.0 to 699.984 nm with a spectral step of 0.052 nm
Original data provided at 203, 223, 243, 273 and 293 K
Linear interpolation to get the cross-sections at 213, 233, 253, 263, 283 K

C.2 NO_2

235-400 nm: Merienne et al., 1995 and Coquart et al., 1995
Reference identifier: NO2/Re3/1 and NO2/Re4/1-3
Original wavelength range: 200-500 nm
Original spectral resolution: < 0.01 nm
Original temperature values: T = 220K, 240K, 293K.
Final spectral resolution: 0.05 nm
Interpolation data set with a spectral sampling rate of 0.0525 nm due to product format limitations
Error estimation: Total error $< 3\%$ at T = 293K, $< 4\%$ at T = 240K, $< 6\%$ at T = 220K
500-667 nm: Vandaele et al., 1998
Reference identifier: NO2/V2/1-2
Original wave number range: 10000-23000 cm-1 (238-700 nm)
Original spectral resolution: 2 cm-1
Original temperature values: T = 220K, 294K.
Choice of the data sets: cross section data at P < 0.015 torr for T = 220K, at P < 0.02 torr at T = 294K
Final spectral resolution: 0.05 nm
Interpolation data set with a spectral sampling rate of 0.0525 nm due to product format limitations

Error estimation: Total error < 3% for λ >250 nm at T=294K, and <3% for $\lambda > 333$ nm at T = 220K
$\lambda >$ **667 nm: Burrows et al., 1998**
Reference identifier: NO2/Br2/1-4
Original wavelength range: 230-794 nm
Original spectral resolution: 0.33 nm
Original temperature values: T = 221K, 241K, 273K, 293K.
Final spectral resolution: 0.05 nm
Interpolation data set with spectral sampling rate of 0.0525 nm due to product format limitations
Error estimation: no information available

Final wavelength range: λ = 235.0 nm: 0.0525 nm: 674.95 nm and 750.0 nm: 0.0525 nm: 779.9775 nm (8381 + 572 = 8953 values).

C.3 NO_3

Wavelength range and spectral interval: 400 - 691 nm , $\delta\lambda$ = 1.0 nm, 292 points (extracted from the original spectrum recorded at 0.1 nm steps without wavelength averaging). Spectral resolution: 0.4 nm. Temperature: 230 and 298 K Reference: Sander (1986). Error estimation : Systematic and random errors (2σ) the larger of ±15% and ±0.210-19 cm2/molec. Remark: Some cross section values are slightly different from those listed in Sander (1986).

The information and notation are from the following report:
Oikarinen, L., E. Kyrölä, and P. Simon, GOMOS prototype High priority study: Cross sections, PO-TN-FMI-GM-015, 1996.

Appendix D

Version IPF 6 vs. IPF 5

For additional information about software changes, see GOMOS Monthly reports.

Level 1:

- Specification of the subpixel PRNU correction (see Sec. 3.3.2.6)
- Specification of the automatic dark charge bias correction (see Sec. 3.3.2.2)
- New reflectivity parameters storage
- New error bars for limb spectra
- Update of the cosmic ray detection and correction algorithm
- Update of the flags for the cosmic ray processing task
- New correction when missing SATU information
- New slit width LUT
- Star spectra location on CCD
- New wavelength assignment
- Flag consolidation
- Attitude file written to DSD (MPH+SPH consolidation)
- Error due to dark current removal included in the error budget of L1b
- Threshold level of pixel saturation (bright limb) changed

Level 2:

- Error coding change
- Full covariance matrix in spectral inversion (see Sec. 4.5.2)
- Changes in the HRTP algorithm